Chair of Petroleum and Geothermal Energy Recovery

Master's Thesis

CO2 Flow in Supercritical Geothermal Systems

Florian Stefan Probst, BSc

May 2023

MONTANUNIVERSITÄT LEOBEN
www.unileoben.ac.at

EIDESSTATTLICHE ERKLÄRUNG

Ich erkläre an Eides statt, dass ich diese Arbeit selbständig verfasst, andere als die angegebenen Quellen und Hilfsmittel nicht benutzt, und mich auch sonst keiner unerlaubten Hilfsmittel bedient habe.

Ich erkläre, dass ich die Richtlinien des Senats der Montanuniversität Leoben zu "Gute wissenschaftliche Praxis" gelesen, verstanden und befolgt habe.

Weiters erkläre ich, dass die elektronische und gedruckte Version der eingereichten wissenschaftlichen Abschlussarbeit formal und inhaltlich identisch sind.

Datum 11.05.2023

Unterschrift Verfasser/in
Florian Stefan Probst

MONTANUNIVERSITÄT LEOBEN
www.unileoben.ac.at

AFFIDAVIT

I declare on oath that I wrote this thesis independently, did not use other than the specified sources and aids, and did not otherwise use any unauthorized aids.

I declare that I have read, understood, and complied with the guidelines of the senate of the Montanuniversität Leoben for "Good Scientific Practice".

Furthermore, I declare that the electronic and printed version of the submitted thesis are identical, both, formally and with regard to content.

Date 11.05.2023

Signature Author
Florian Stefan Probst

Florian Stefan Probst, BSc.

Master Thesis 2023

Petroleum Engineering

CO_2 Flow in Supercritical Geothermal Systems

Supervisor: Univ.-Prof. PhD Keita Yoshioka
Advisor: Dr. Víctor Vilarrasa

Chair of Petroleum and Geothermal Energy Recovery

dpe

MONTAN UNIVERSITÄT LEOBEN

Acknowledgements

First, I would like to thank my supervisor Univ.-Prof. PhD Keita Yoshioka for the opportunity to write this master's thesis. His support and expertise helped me broaden my knowledge in the field of simulations as well as geothermal energy recovery.

I also want to thank Dr. Víctor Vilarrasa, who advised this thesis, for taking the time to share his vast knowledge on the topic in various meetings and his valuable contributions.

Furthermore, I would like to express my endless gratitude to my family, who, through their support in all aspects of life, gave me the possibility to pursue a university education.

Abstract

CO_2 is one of the main greenhouse gases causing climate change and its efficient removal from the atmosphere will determine whether the goals set in the Paris Agreement can be reached or not. By capturing and permanently storing CO_2 right after its generation, either from power plants or industry-related processes which require large amounts of fossil energy or produce CO_2 in the chemical reactions that take place during the manufacturing of products, a neutral carbon footprint can be achieved. Geological carbon storage can be achieved by injecting CO_2 in underground reservoirs such as aquifers or depleted gas reservoirs. However, due to the low density of CO_2, it is naturally buoyant and creates a plume as the topmost component of the reservoir. Due to this buoyancy, the presence of a tight seal rock is essential in the traditional storage concept, thus preventing an escape of the CO_2. Alternatively, storing CO_2 in supercritical geothermal systems does not require a caprock because at the pressure and temperature of these systems, CO_2 is denser than supercritical water and, thus, sinks. In light of recent achievements in the drilling of high temperature volcanic areas, such as the Icelandic Deep Drill Project, it deems possible to exploit supercritical reservoirs for CO_2 storage combined with simultaneous geothermal energy production where the critical point of water (T = 374°C and p = 21.8 MPa) is exceeded. Our simulations show that CO_2 injection is gravity dominated with the reservoir permeability as high as 10 mD and the CO_2 plume sinks. Also, if we choose adequate well spacing, CO_2 breakthrough can be avoided. Compared with water injection, CO_2 injection leads to a smaller area of the cooled region due to the lower heat capacity of CO_2, which subsequently lowers the risk of thermally induced seismicity. The cumulative geothermal energy production between water and CO_2 is comparable and when considering the benefits of safe long-term CO_2 storage, CO_2 injection may be a more viable option for supercritical geothermal pressure maintenance.

Zusammenfassung

Das Treibhausgas CO_2 ist mitverantwortlich für den Klimawandel. Seine effiziente Entfernung aus der Atmosphäre wird ausschlaggebend sein, ob die in den Pariser Abkommen festgelegten Klimaziele erreicht werden können oder nicht. Durch die Absonderung von CO_2 direkt nach seiner Entstehung, zum Beispiel als Abgas von Kraftwerken oder industriellen Prozessen, welche große Mengen fossiler Energie erfordern, kann ein neutraler CO_2-Fußabdruck erreicht werden. Die Absonderung des CO_2 aus der Atmosphäre kann durch seine Speicherung in unterirdischen Reservoirs, wie tiefliegenden Grundwasserträgern oder erschöpften Gaslagerstätten, erreicht werden. Aufgrund der geringeren Dichte von CO_2 im Vergleich zu Wasser schwimmt es jedoch als leichtere Komponente wie eine Blase im Reservoir auf. Aufgrund dieses Auftriebs ist es unerlässlich, dass bei der Speicherung von CO_2 in herkömmlichen Lagerstätten eine impermeable Deckschicht vorhanden ist, um das Austreten des CO_2 zu verhindern. Als Alternative kann das CO_2 in überkritischen, geothermalen Reservoirs gespeichert werden, da durch die dort herrschenden hohen Temperaturen und Drücke, CO_2 dichter als das Lagerstättenwasser ist und folglich absinkt. Aufgrund der Ergebnisse erfolgreicher Bohrungen in Gegenden des aktiven Vulkanismus, wie dem „Icelandic Deep Drill Project“, hält man es für möglich überkritische Lagerstätten, einerseits als CO_2 Speicher und andererseits als geothermale Ressource zu verwenden, weil dort der kritische Punkt von Wasser ($T = 374°C$ und $p = 21.8$ MPa) überschritten wird. Unsere Simulationen zeigen, dass die Bewegung der CO_2 Blase, bei einer Lagerstättenpermeabilität von 10 mD, von der Schwerkraft bestimmt wird und die Blase somit absinkt. Durch die korrekte Wahl der Entfernung zwischen den zwei Bohrungen wird sichergestellt, dass kein CO_2 die Produktionsbohrung erreicht. Darüber hinaus führt die Injektion von CO_2, durch seine geringere Wärmekapazität, zu einer geringeren Abkühlung der Lagerstätte und verringert so das Risiko von thermisch induzierter Seismizität. Da die gesamte produzierte Wärmeenergie, bei Injektion von CO_2, sich kaum von der Wärmeenergie bei Injektion von Wasser unterscheidet führt der zusätzliche positive Effekt der CO_2 Absonderung dazu, dass gesamtheitlich betrachtet, die Injektion von CO_2 die bessere Alternative zur Aufrechterhaltung des Druckhaushalts in überkritischen, geothermalen Systemen darstellt.

Table of Contents

Chapter 1

Introduction

In times where countries are expanding and diversifying their energy portfolio, they deem to further their independence within the energy market. With climate change being on top of the agenda of modern society and politics the role of non-hydrocarbon and non-fossil forms of energy becomes more important. Especially countries in which oil and gas reservoirs are depleted or not readily available are looking into new forms of energy generation instead of solely relying on the import of energy. A transformation of the energy industry lies ahead and while renewable forms such as power from wind farms, solar systems as well as hydroelectric plants look promising, the use of geothermal energy can fill the void in times where wind is not abundant, or the sun is not shining.

In order to effectively prevent climate change the excess carbon dioxide in the atmosphere has to be removed and stored safely underground. Carbon sequestration while simultaneously using the reservoir as a geothermal power source can be a solution for this increasing demand of carbon storage. However, when CO_2 is injected into a reservoir a plume is created. This liquid plume makes up the topmost layer of the phases in the reservoir which creates the additional problem of needing a seal to prevent it from leaking. Without an appropriate seal, the CO_2 could migrate to upper geological formations and ultimately escape from the reservoir defeating the purpose of long-term storage.

By utilizing the high temperatures and pressures in supercritical geothermal reservoirs, the conditions there could make it possible to inject the CO_2 in a state where it is denser than the brine present in the reservoir (Parisio and Vilarrasa 2020). This phenomenon renders the tight seal rock not necessary as the CO_2 exists as the denser phase at the bottom of the reservoir because of its sinking tendency. Additionally, in some volcanic geothermal reservoirs there are no potential water recharge areas present (Celati et al. 1991). This means that the water

lost during normal operation of the geothermal system has to be reinjected. By injecting CO_2, the geothermal reservoir can be re-pressurized to support ongoing production.

This thesis aims to provide an overview of state-of-the-art geothermal energy systems and evaluate the effects of gravity, permeability, well spacing as well as injection temperatures on the behavior of the sequestered CO_2 plume, thermal effects and the resulting cumulative energy production. Through the variation of the above-mentioned parameters, a comparison between traditional water injection versus CO_2 injection is drawn, pointing out the advantages and disadvantages of this technology. The software used in this study is Multiphysics object-oriented simulation environment (MOOSE), which is an open-source program that provides results based on a 2D mesh of a deep volcanic reservoir.

Chapter 2

Geothermal Energy

Geothermal energy refers to energy that can be used as part of the natural heat flux from the earth's core. This heat is transported either by conductive or convective processes (Elders and Moore 2016) from the core to the base of the mantle which then releases heat at the base of the earth's crust (Huenges 2010).

Heat flux varies from 10 mWm^{-2} beneath stable continents (Huenges 2010) to 50 mWm^{-2} beneath continental margins or values above 70 mWm^{-2} have been suggested to occur beneath young perturbed areas (Huenges 2010). According to Glassley (2010), the average heat flux across the globe would be 87 mWm^{-2} which would result in a global heat output, across the entire earth's surface, of $4.4x10^{13}$ W (Glassley 2010). This is a very broad representation of the potential energy that can be sourced from geothermal systems and should illustrate that the potential for this kind of renewable energy seems limitless.

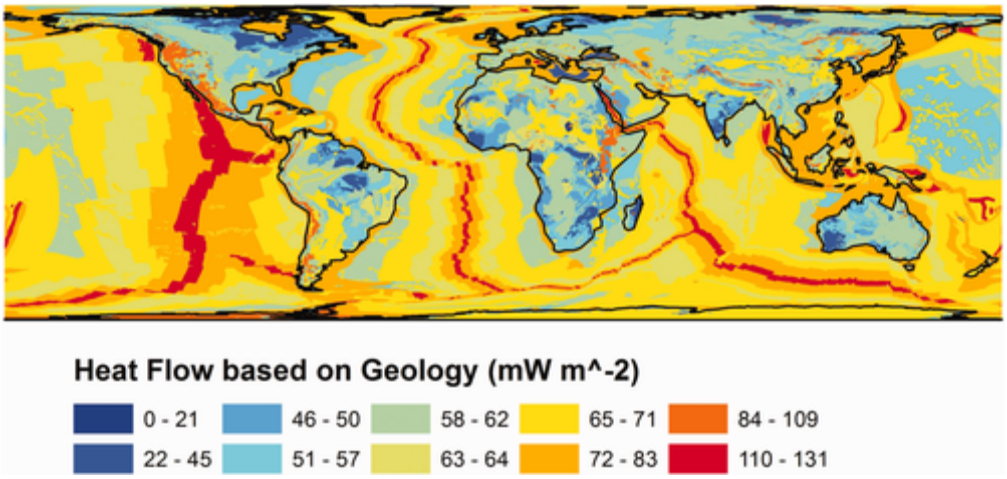

Figure 1. Global heat map (Davies 2013)

The source of the generated heat are of two origins, the first one being heat due to decay of radioactive elements such as ^{238}U, ^{232}Th and ^{40}K, and the second source being the residual

heat generated during the accretion of the earth (Elders and Moore 2016). Figure 1 shows that the highest heat flux generally occurs at the tectonic plate boundaries, nevertheless the identification and locating geothermal systems can be very complicated and depends on the tectonic setting, heat source, reservoir depth, rock type as well as surface features and topography (Elders and Moore 2016).

2.1 Conventional Geothermal Systems

Geothermal systems can be split up into conventional and unconventional geothermal systems. In conventional systems, the classification is performed according to reservoir temperature, fluid type and heat transfer (Elders and Moore 2016). When dealing with systems of 150°C and below, the system is a low-temperature system, which can usually be found in continental regions (Basel I. Ismail 2022) and is used for applications such as heat pumps and direct use (Elders and Moore 2016). Direct use includes the heating of homes, agricultural applications as well as aquaculture and in some cases small scale electricity generation (Green 2004). Moderate temperature systems, 150-200°C, like low temperature systems, are also mainly found in continental regions. They are used for electricity generation but require a pump in order to bring the hot fluid to the surface. In contrary, high temperature conventional systems of 200°C and above, are typically found close to volcanic regions and island chains (Basel I. Ismail 2022) and use thermo-artesian flow in order to transport the fluid to the surface without requiring any pumps and thus generating electricity from the well (Elders and Moore 2016).

2.1.1 Geothermal Heat Pumps

Low-temperature geothermal resources, such as geothermal heat pumps, are applied in residential and commercial buildings and installed at shallow depths. In these depths the soil maintains a consistent temperature of about 10°C to 13°C during the winter and summer months (Glassley 2010). This distinct feature of the earth can be used to use it as an excellent heat sink in the summer months, when temperatures climb and used as a heat source during the winter months, where heating is required, and exterior temperatures are usually below 10°C.

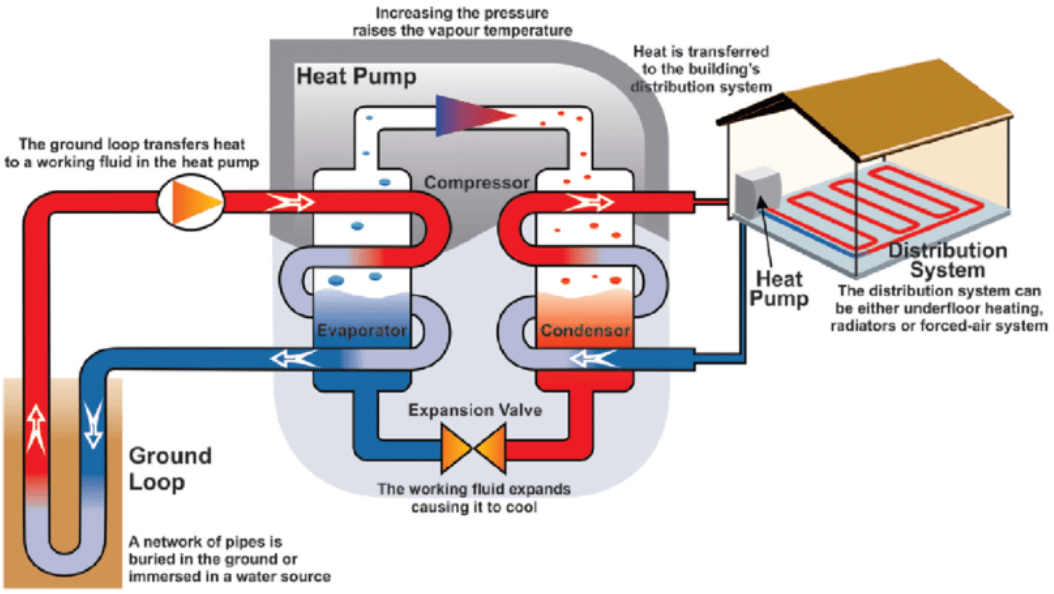

Figure 2. Schematic of a Geothermal Heat Pump (Climo et al. 2012)

The working principle of geothermal heat pumps is illustrated in Figure 2. The system consists of two loops. The ground loop continuously circulates fluid either through a network of pipes that are coiled up in a shallow layer of the subsurface or it can be installed as a deep vertical heat collector whenever deeper and higher temperature reservoirs are targeted. Subsequently, the circulating refrigerant, also called working fluid, within the heat pump is heated up by turning the working fluid into a hot gas, as a consequence of the refrigerant having a boiling temperature significantly below that of the local subsurface. As a next step, the hot gas is compressed via a pump and, through this pressure increase, work is added to the system (Glassley 2010). The hot gas passes through the second heat exchanger which heats up the distribution system loop. Afterwards the cooler gas condenses and passes through an expansion valve, causing further cooling of the condensate into a cold liquid. The system can be reversed in order to use it for cooling purposes in the summer months.

In a closed loop system, as shown in Figure 2, the heated mixture consists of water and antifreeze. Another application of heat pumps is to inject the water into a geothermal reservoir via an injection well and produce it via a production well which as a doublet system. However, both systems (open- and closed loop) transfer heat to a working fluid (via a heat exchanger) which subsequently transfers the heat to a distribution loop within a household.

2.1.2 Hydrothermal Systems

For power generation most common geothermal systems currently in use are hydrothermal systems. In order for such a system to develop naturally, three prerequisites have to be in place: heat, water and permeability (Geothermal Technologies Office 2019). These reservoirs are created by hot water or steam being trapped in the pores of a rock which is sealed by an impermeable cap rock layer (Geothermal Technologies Office 2019). The temperature range for these systems is around 200°C and above but temperatures are generally below the critical point of water leading to, depending on the pressure and temperature, liquid, steam, or two-phase flow dominated reservoirs. When looking at an enthalpy – pressure phase diagram most hydrothermal systems are usually on the low-enthalpy side of the critical point and flash to steam either in the reservoir itself or within the wellbore (Glassley 2010) but ideally flashing occurs in a planned manner. Therefore, the conditions of when the fluid of a well will flash needs to be understood in order to perform proper well- and surface facility design.

2.1.3 Geothermal Power Technologies

2.1.3.1 Single Flash and Double Flash

Flash systems are dominating the geothermal energy systems worldwide as 42% of installed capacity are single flash systems and 19% double flash systems (Anderson and Rezaie 2019). Figure 3 shows a single flash system where the two-phase water-steam mixture is extracted from the well via a brine pump and consequently flows into the separator. After flash vaporization in the separator, the vapor expands through a turbine resulting in power generation, while the majority of the liquid is reinjected into the reservoir at the separator (Anderson and Rezaie 2019).

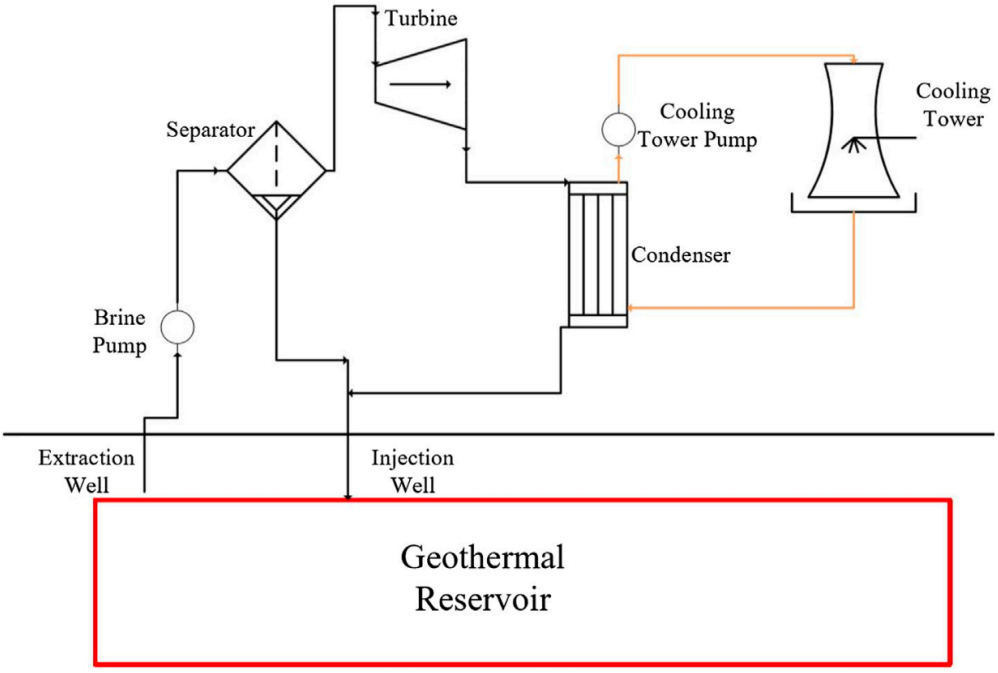

Figure 3. Single flash steam cycle for two-phase mixtures (Anderson and Rezaie 2019)

Understanding the flashing process is required in order to correctly design the system in a way that the produced enthalpy is maximized and the steam quality is at its optimum. Figure 4 shows a pressure – enthalpy diagram of a hydrothermal system with reservoir conditions of 200 bar and 235°C (Point 1) and, according to the diagram, the system will flash to steam when the pressure drops to 30.6 bar (A) (Glassley 2010). As an idealized assumption from this point on the system behaves isenthalpically. The amount of steam is maximized if temperature and pressure are reduced as much as possible, which in this case leads to a temperature of 50°C as the final state. From the diagram a steam quality of 33% can be read (as indicated by the dashed lines) which means that one third of the fluid mass is converted to steam. The path from point 1 to A-B is the initial separation of vapor from the liquid and from B on the vapor expands through the turbine and the condensed liquid reaches point 2. Due to the 33% steam quality, we know, in terms of extracted mass, we must take out three kilograms of liquid from the reservoir in order to get one kilogram of steam for our system. Another concern connected to steam quality is the moisture's effect on the turbine efficiency. Thus the liquid has to be separated from the mixture effectively otherwise the energy extraction efficiency is reduced by 30% (Glassley 2010).

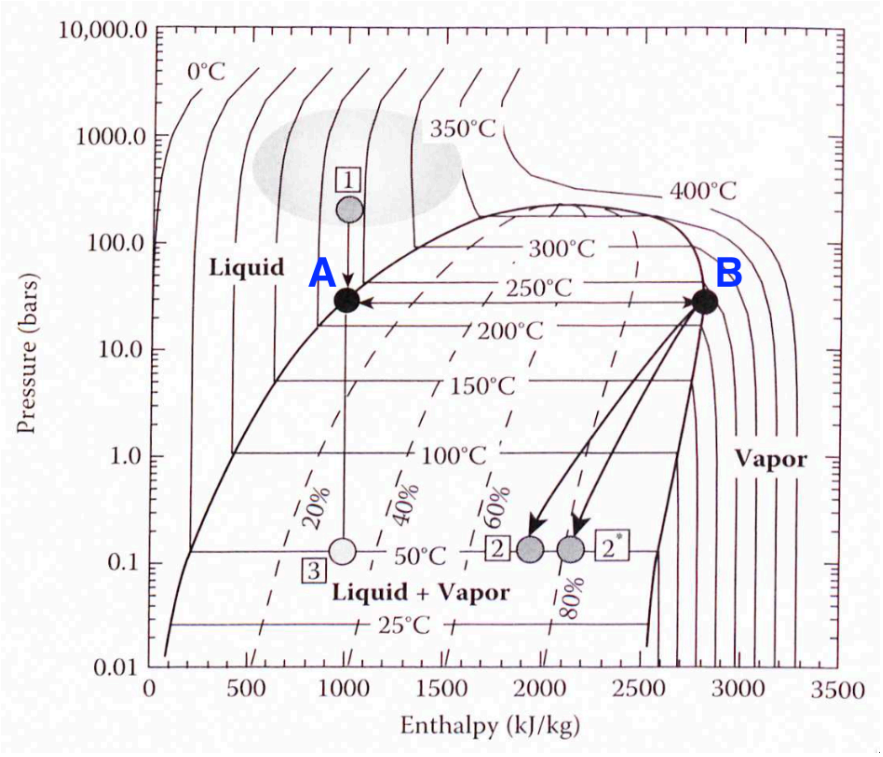

Figure 4. Pressure-enthalpy diagram for single flash vaporizing. Most hydrothermal systems are located in the shaded section (Modifications added to the original from Glassley 2010)

In case the reservoir temperature is high enough a so-called double or dual flash cycle can be utilized. In this system the liquid phase remaining from the first flash cycle is flash vaporized again powering a lower pressure turbine and generating an additional 20-30% of power (Mondejar and Chamorro 2017).

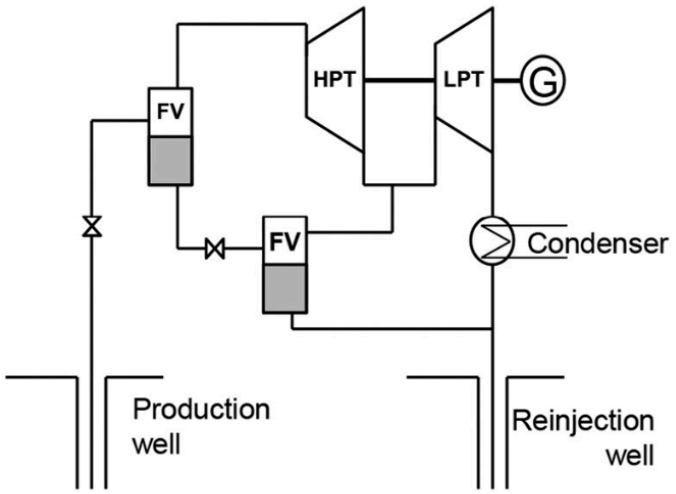

Figure 5. Process flow diagram of a double-flash system with two separators and two turbines for high- and low pressure and temperature cases (Mondejar and Chamorro 2017)

Initially the process follows the same path on the pressure enthalpy diagram (Figure 6) as the single flash system. The reservoir fluid is in its liquid state at point 1, and reaches two-phase state, the initial separation of vapor and liquid (A to A*). A cyclone separator separates the phases, and the steam is fed into the turbine, thus generating electricity. At this point the dual-flash system differs from the single-flash one. In the single flash system, the turbine would recover the maximum heat possible and the cool condensed and separated fluid from the separator would be injected back into the reservoir at the lowest temperature possible. However, the heat of the condensed fluid would be lost as it would simply be fed into the cooling unit and flowing back into the injection well. In the case of dual flash the first turbine is designed to work in a narrow pressure and temperature range because the initial flash operates in a moderate window and cooling is only down to approximately 150°C (A* to 2). The main advantage is that the separated hot water from the first flash (A to B) can be flashed again at a lower pressure (point B) and will not go to waste like in the single flash case (Glassley 2010). After the second flash the vapor enters a different turbine, designed specifically for handling lower pressures and high efficiencies thus generating additional electricity.

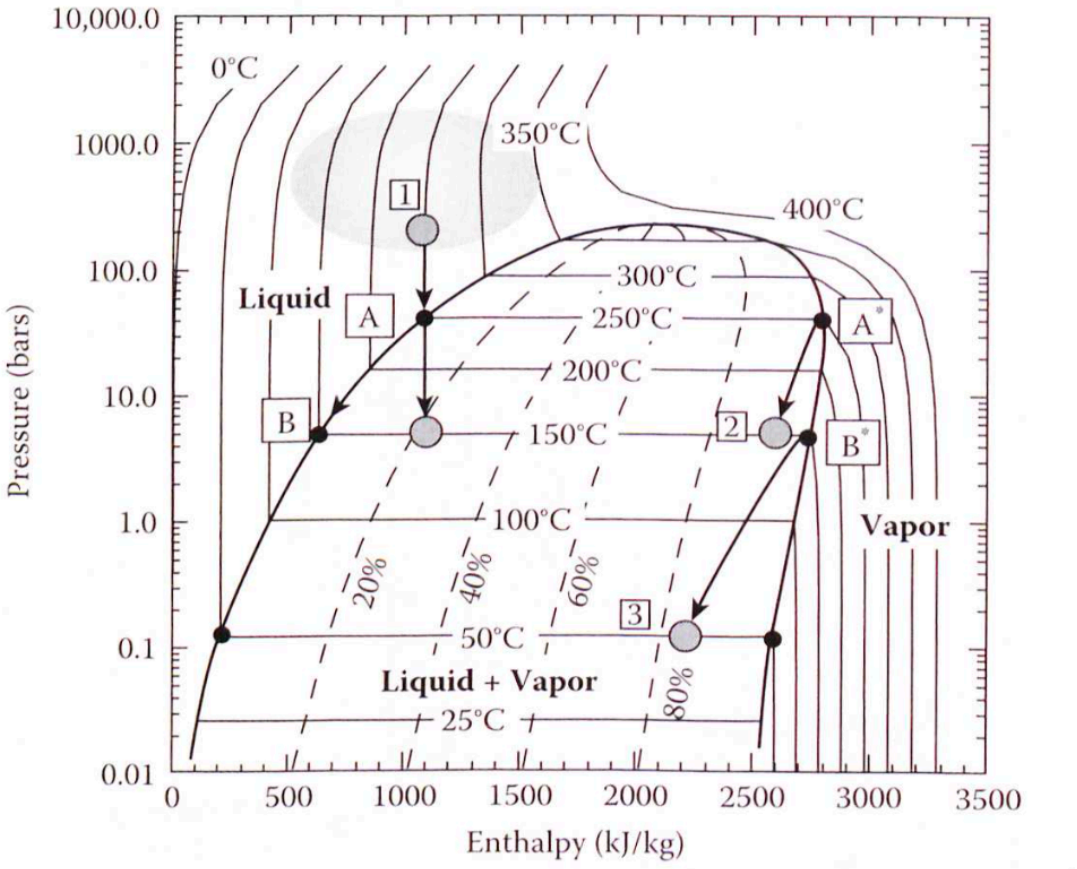

Figure 6. Schematic of a double flash system on a pressure-enthalpy diagram. Starting point is at point 1 and the end state is reached at point 3 (Glassley 2010)

2.1.3.2 Binary Cycle Systems

In reservoirs where the reservoir temperature is below 150°C, flashing will not result in efficient power generation. This is due to the low temperature difference of the fluid in the initial and the end state (Glassley 2010). Additionally, due to the low-energy density of the fluid, that is Joules per mass of fluid, it requires a different method in order to convert thermal energy to electricity. Figure 7 shows a schematic of a binary organic Rankine cycle which consists of a pump, heat exchanger, produced fluid loop, working fluid loop, turbine connected to a generator as well as a condenser.

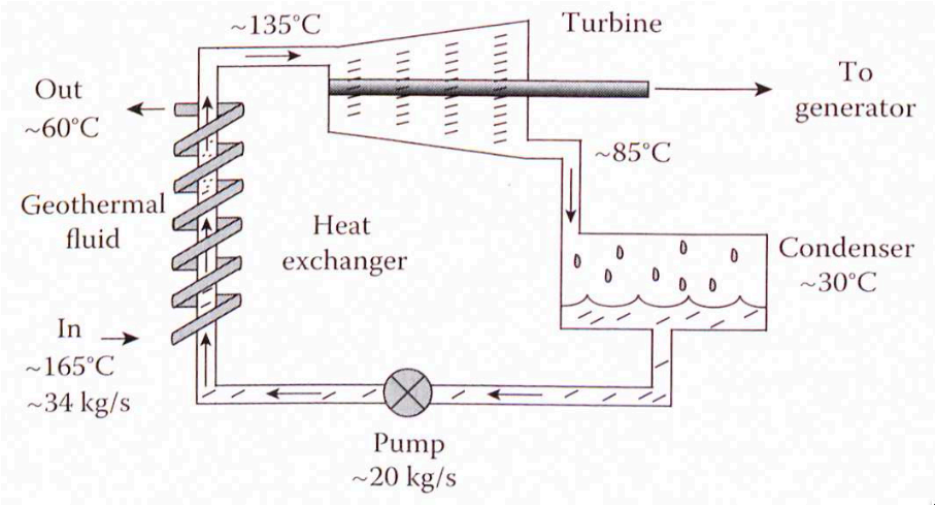

Figure 7. Schematic of a binary cycle system with generalized values at each station (Glassley 2010)

The values shown in the figure are representative of the temperatures and mass flow rates in real applications. Typical capacities of theses power plants range from 2 to 50 MWe, but when averaged across the globe the installed capacities are around 5 MWe (Mondejar and Chamorro 2017).

The working fluid itself must fulfill two conditions: boiling point must be significantly below that of water and it has to be nonreactive with the piping and the surrounding machinery that it passes through (Glassley 2010). The fluids that meet this criterion are isopentane or butane. The low boiling point characteristic causes the working fluid to be vaporized by the heat supply of the produced fluid through the heat exchanger, thus driving the developed vapor into the turbine causing it to spin (Basel I. Ismail 2022). The vapor is then cooled and condensed in the condenser and pumped through the heat exchanger to repeat the power generation process.

When considering the environmental footprint, unlike in flash power plants, binary cycle power plants do not release any emissions to the atmosphere (Glassley 2010). Due to the

closed loop design, neither the geothermal fluid nor any steam or fumes from the condensation and cooling process is released into the atmosphere.

As the power output of a binary cycle power plant depends on the temperature difference between the geofluid and the working fluid, and since there is no water cooling in such a system, it makes binary plants susceptible to seasonal changes in temperature. During the winter months the low atmospheric temperatures keep the temperature difference (ΔT) high, thus generating the expected energy output. In the summer months, when atmospheric temperatures are warm, power generation capacity is reduced by as much as 20% (Glassley 2010).

2.1.4 Dry Steam Systems

Power generation systems are bound to the state the reservoir is in and if any liquid will be produced to the surface. Previously discussed flash systems and binary cycle systems are suitable for hydrothermal reservoirs where the reservoir is initially in liquid phase or liquid-vapor phase. Dry steam systems are suitable for application when dealing with reservoir temperatures above the critical point of water (373.946°C & 220.64 bars), or pressures and temperatures which move the operating point to the vapor zone of the phase diagram (Glassley 2010). In other words, the most suitable reservoir candidates are the ones that do not reach conditions where liquid and vapor coexist. In contrast to flash systems, dry steam systems do not require any separation of a liquid phase, thus it is understandable why dry steam operations are among the most simple and cheapest designs for geothermal power plants (Anderson and Rezaie 2019).

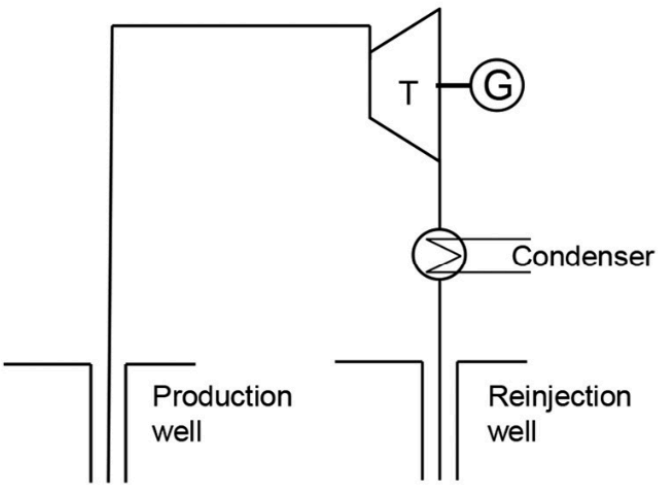

Figure 8. Schematic of a dry steam operation, with piping kept to a minimum and no liquid separators. (Mondejar and Chamorro 2017)

The high-pressure steam rises through the production well while decompressing but remains in the vapor phase the entire time. Before reaching the turbine, the vapor passes through a particulate separator with the purpose of removing any solids or particulates that might damage the turbine. Although dry steam power plants typically have higher efficiencies than other systems (Anderson and Rezaie 2019), the main constraint lies in the expansion within the turbine. It is important to minimize steam condensation in this step, as every percent increase in liquid fraction results in a 0.5% drop in turbine isentropic efficiency (Mondejar and Chamorro 2017).

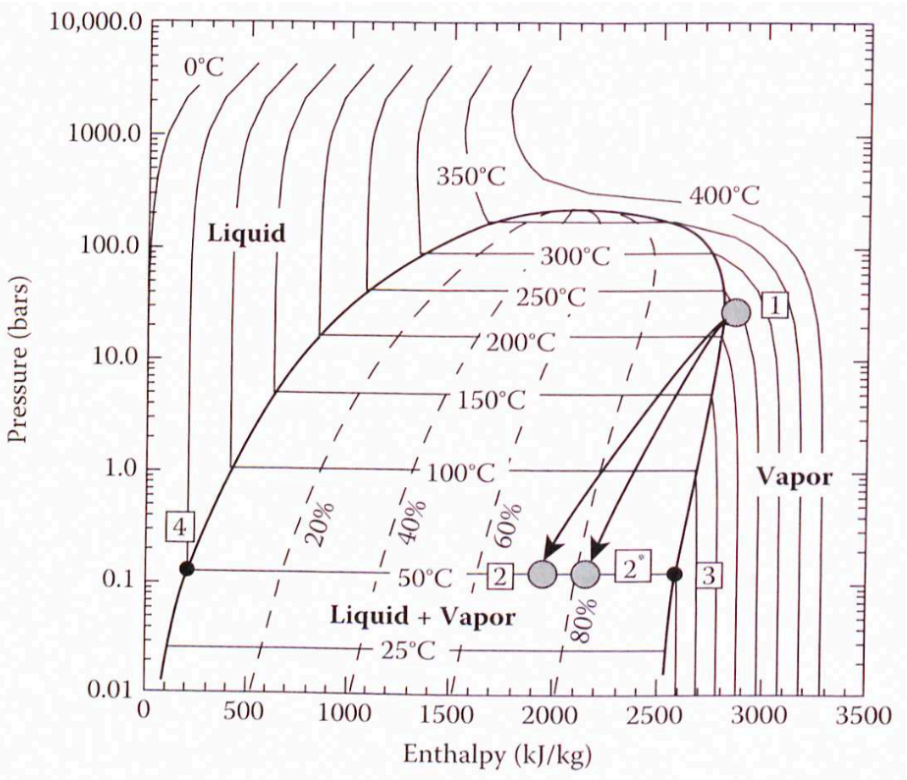

Figure 9. Pressure-enthalpy diagram of a dry steam system (Glassley 2010)

In terms of thermodynamics, dry steam systems deliver the highest energy density (energy per kilogram of extracted fluid), with the average size of these units being about 45 MWe (Mondejar and Chamorro 2017). The reason for such high energy densities relies mainly on the fact that the enthalpies are not partitioned into fluid phase enthalpy and vapor enthalpy, as is the case in most hydrothermal reservoirs, but rather most of the enthalpy of the fluid remains with the steam. As seen in Figure 9, the vapor expands in the turbine at point 1 at very high temperatures, with the ideal situation being that the expansion would happen isentropic and reversible (Figure 9, 1-2). Due to heat losses through conduction and friction, the real situation will differ to the idealized one and rather be resembled by path 1-2* (Glassley 2010).

2.2 Unconventional Geothermal Systems

The characteristic that divides geothermal systems in conventional and unconventional systems is described by the reservoir itself. Conventional systems are using the heat that is stored within a couple of kilometers of depth via extraction of a working fluid from a suitable reservoir. However, although temperatures up to 150°C within 10 km of depth are commonly available around the globe (Glassley 2010), the bigger issue is finding the right downhole conditions. Most of the high temperature resources could be produced economically when only temperature is considered, but lack either the natural permeability to produce fluids (Elders and Moore 2016) or, in some cases, have extremely high temperatures which brings the drilling and completion equipment to its limits.

Unconventional geothermal systems include enhanced geothermal systems (EGS), supercritical geothermal resources combined with CO_2 injection as well as resources in ductile, high-enthalpy, geological reservoirs that belong to the category of advanced geothermal systems (Elders and Moore 2016; GeoEnergy 2021).

2.2.1 Enhanced Geothermal Systems

Enhanced Geothermal Systems, or EGS, are man-made geothermal systems. EGS work independently of in-situ water or permeability being present which means they are able to produce thermal energy through conduction. This heat transfer process is introduced in the reservoir by pumping and circulating a fluid through the created fractures in the hot rock (Mondejar and Chamorro 2017).

Enhancing a geothermal reservoir is performed by utilizing the hydrofracturing technique, widely used in the Oil and Gas industry. However, the process of stimulation in EGS can be considered more as a reservoir creation than a reservoir stimulation, as there is usually no reservoir present in the first place (Guinot and Meier 2019).

The typical target for EGS, also known as Hot-dry-rock method (HDR) is hot impervious crystalline dry basement rock, which can be found almost everywhere beneath the earth's surface ("Geothermal: Digging Beneath the Surface" 2020). In very basic terms, the process of creating an enhanced geothermal system consists mainly of drilling two wells which are spaced properly and inject fluid into the formation causing the formation to breakdown, thus connecting the two wells via creation of a flow path.

2.2.1.1 Hydraulic Stimulation

In more detail, hydraulic fracturing can typically be described by four principles (Pongratz 2021):

1. Injection of fracturing fluids
2. Fracture initiation/breakdown of the formation
3. Fracture propagation/extension
4. Use of proppants to keep the fracture open

The first three phenomena can be seen in Figure 10:

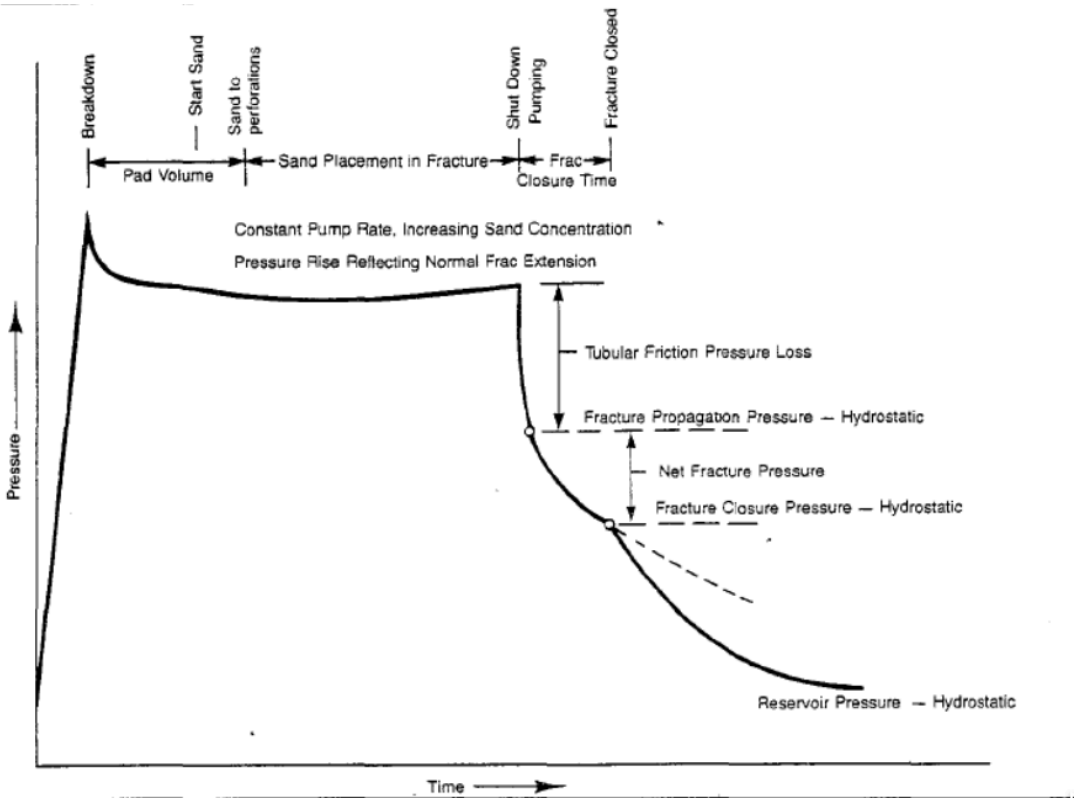

Figure 10. Idealized Pressure vs. Time diagram describing the different stages of a hydraulic fracturing job (Pongratz 2021)

If injection into the rock occurs at a higher rate than the fluid can escape the formation then inevitably the pressure increases. This goes as far as the formation breaking down, as seen in Figure 10. The formation breaks and the fracture propagates perpendicular to the minimum principle stress (Ott 2018), and after the initial formation breakdown, the fracture propagates. Since fractures are induced under tensile stress, the fracture would close when injection stops which is why the injection slurry is mixed with a proppant. This is needed in order to keep the fracture open even after the fluid leaves the fracture. After successfully placing the proppant, the final flush stage is reached, during which a fluid is injected with the goal to clean the wellbore of any remaining proppant (Ott 2018).

In order to perform a successful and efficient fracturing job it is necessary to gather all the necessary data. This includes the petrophysics and formation properties such as permeability, porosity, young's modulus, in-situ stresses, pore-pressure and temperatures (Pongratz 2021). Other important data includes fluid-loss characteristics, total fluid volume pumped, type and amount of propping agent, pad volume, fracture fluid selection and injection rate (Lake, Fanchi, and Society of Petroleum Engineers (U.S.) 2006). To provide an overview of the challenges and difficulties that arise when trying to establish a fracture network for EGS purposes, this section discusses the most important design steps and tests.

To gather information about the downhole pressures, pressure losses, closure limits, shut-in pressures et cetera, pumping diagnostics is performed.

Pumping diagnostics is generally a relatively short duration pump-in followed by a shut-in period. This information is necessary in order to set up a pumping schedule in which the program is planned in detail. Typical injection tests include step-up tests, step-down tests and Pump-in/Shut-In tests (MiniFrac or Fluid Efficiency Test).

Step-Up tests, also called step rate tests, are performed by injecting a fluid and stepping up the injection rate. The results of this test show the closure pressure limits, and flow rates needed to successfully complete the treatment.

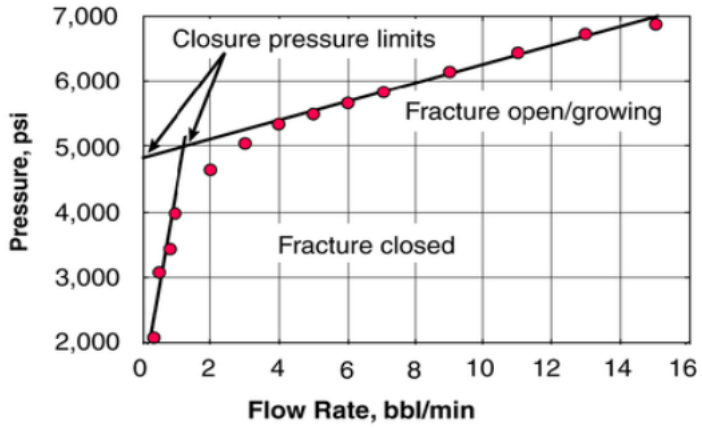

Figure 11. Step-Up Test (Pongratz 2021)

A tool to determine near wellbore and perforation pressure losses is the step-down test (Figure 12). In this test a fluid with known properties is injected into the formation at a rate high enough to open a small fracture. Then the injection rate is reduced stepwise with each step lasting the same amount of time. After the test is completed, the pressure response due to the rate change can be analyzed and the effect of perforation and near-wellbore friction can be determined ("Step-down Test Analysis" 2017).

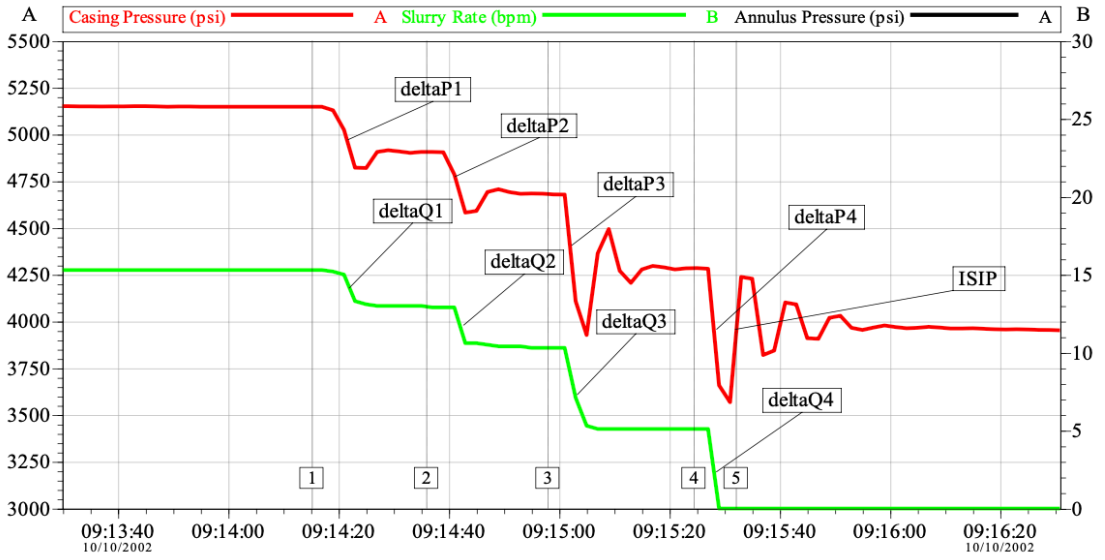

Figure 12. Step-down test (Pongratz 2021)

By plotting the pressure versus rate data points with the same time, the cause of the near wellbore pressure drop can be determined. As illustrated in Figure 13, if the graph is concave upward then it is dominated by tortuosity and if the curve is concave downward the pressure drop is dominated by the friction losses across the perforations (Lake, Fanchi, and Society of Petroleum Engineers (U.S.) 2006).

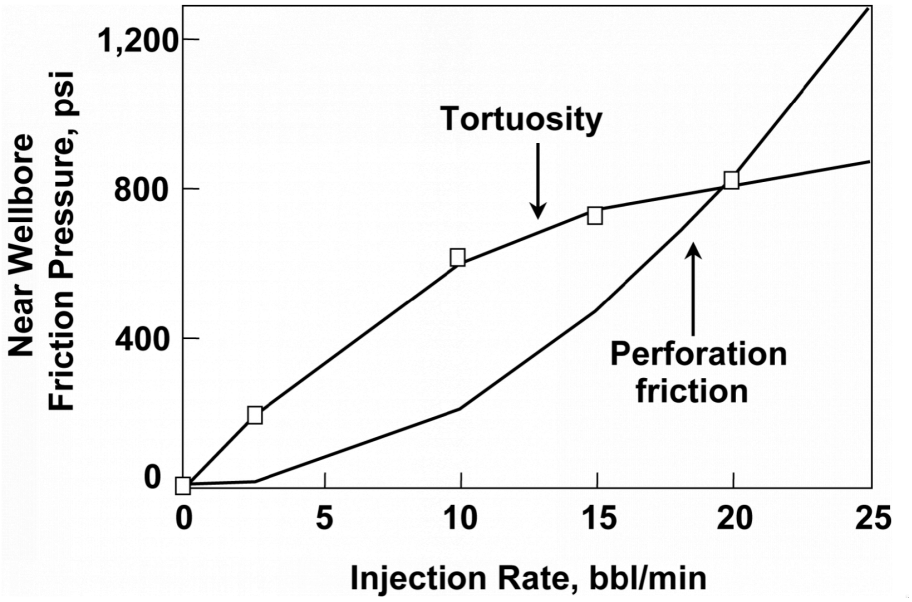

Figure 13. Pressure vs. rate plot to determine near wellbore pressure losses ("PEH:Hydraulic Fracturing" 2017)

A typical pump-in test is the so-called Minifrac test which is performed without placing a proppant and is done prior to the main injection treatment. The goal of a Minifrac is to create a small fracture by breaking down the formation and the stop injection and observe closure of

the fractures. Figure 14 shows a Minifrac test which is always performed prior to the main stimulation treatment as it provides useful information such as formation breakdown pressure, instantaneous shut-in pressure and fracture closure pressure as well as other design parameters like fluid efficiency, formation permeability, reservoir pressure and stress state ("Minifrac" 2017).

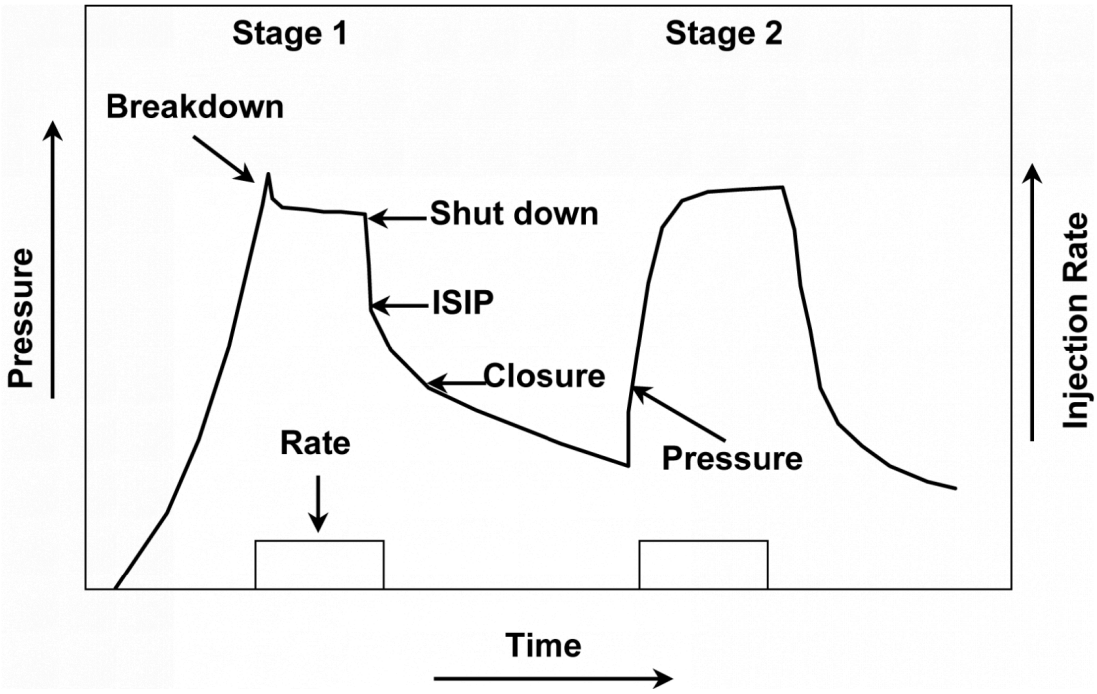

Figure 14. A typical pressure/rate versus time representation of a Minifrac test. After injection is stopped ISIP and closure pressures can be observed from the graph ("PEH:Hydraulic Fracturing" 2017)

Before the main stimulation treatment begins it is crucial to select the correct stimulation fluid and proppant. The fracturing fluid itself can be classified according to fluid types and has to have certain characteristics. These include good clean-up behaviour to maximize fracture conductivity, high viscosity in the fracture, fluid viscosity should be high enough to prevent excessive leak off into the formation but at the same time have a low friction pressure to allow for high-rate pumping (Pongratz 2021). At last, the fluid should be non-hazardous, have a high hydrostatic gradient which minimizes surface treating pressures and also should be low in cost.

Designing the fluid to conform to the characteristics named above can be done by properly selecting the suitable fluid type. Table 1 shows the different base fluid types along with their main composition and ideal application.

Table 1. Fracturing fluid selection chart and conditions for their use (Pongratz 2021)

Base Fluid	Fluid Type	Usage
Water	Linear	Short fractures, low temperatures
	Crosslinked	Long fractures, high temperatures
	Micellar	Moderate length fractures, moderate temperatures
Foams	Water based	Low-pressure formations
	Acid based	Low-pressure carbonate formations
	Alcohol based	Low-pressure water-sensitive formations
Oil	Linear	Short fractures, water-sensitive formations
	Crosslinked	Long fractures, water-sensitive formations
	Water emulsion	Moderate length fractures, good fluid loss control
Acid	Linear	Short fractures, carbonate formation
	Crosslinked	Longer, wider fractures, carbonate formations
	Oil emulsion	Moderate length fractures, carbonate formations

Depending on the application of the fluid, different additives can be added to customize the fluid further. Such additives include polymers, biocides, surfactants, gel breakers, conductivity enhancers, pH control agents as well as defoamers and fluid loss additives (Pongratz 2021). The additives are blended into the fracturing fluid at the surface with the main goal of improving the effectiveness of the resulting fracture.

Proper EGS design with the correct proppant selection dramatically improves economic performance in some cases (Hu et al. 2021), and establishes connectivity of the wellbore. Typical proppant materials include sand, resin-coated sands, ceramic proppants as well as walnut hulls, aluminum pellets or plastic beads (Pongratz 2021). Classification among these

materials is based on the strength of the material to avoid crushing, the quality and geometric factors such as size and sphericity (Pongratz 2021).

As compared to hydraulic fracturing in the Oil and Gas industry, which assumes that only newly generated and propagating fractures contribute to the permeability, the EGS community also considers pure shear stimulation. In pure shear stimulation the permeability enhancement is due to induced slip on preexisting fractures, which indicates that natural fractures open without the formation of new fractures (McClure and Horne 2014). This process of inducing slip is called “hydroshearing” and, in contrast to hydrofracturing, does not necessarily lead to a fracture orientation perpendicular to the minimum principal stress (McClure and Horne 2014). While some believe this is the main reason for enhanced permeability, others believe that it is a mixture of newly created fractures and propagation of existing natural fractures which is responsible for successful EGS completion (McClure and Horne 2014).

2.2.1.2 In-Field, Near-Field and Deep EGS

The development of enhanced systems is still being explored intensely with the most readily available resources being in- and near-field resources. Compared to near-field and deep EGS resources, in-field resources are located shallower and within existing hydrothermal locations but with very low permeabilities (Geothermal Technologies Office 2019). Due to the low permeability of the reservoir rock, the circulation path needs to be enhanced by hydraulic fracturing.

Near-field EGS, are typically present in vicinity to hydrothermal resources but do not have a permeable reservoir system in place along with the heat being generated by thermal anomalies (Geothermal Technologies Office 2019). In addition to the lack of permeability, they typically do not have a sufficient fracture network thus needing improved technology to establish connectivity between injection and production wellbores.

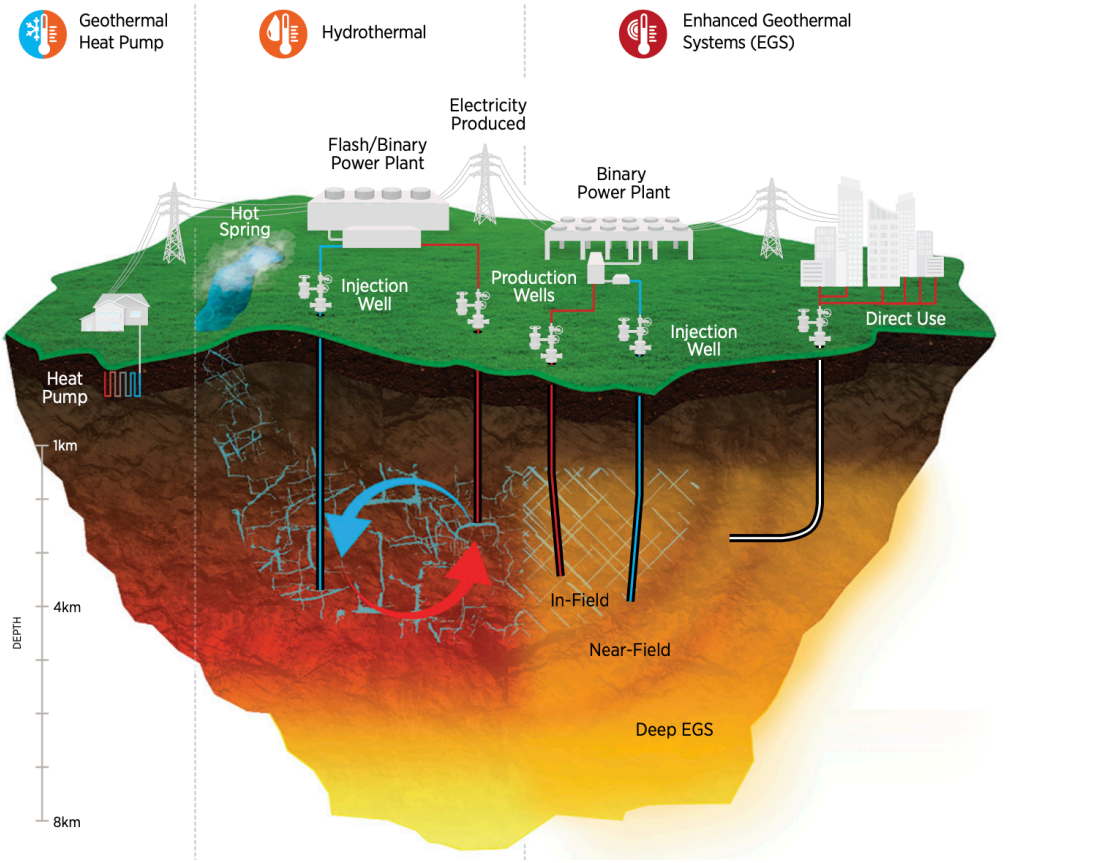

Figure 15. Overview of categories and subcategories of geothermal energy systems (Geothermal Technologies Office 2019)

The third category of enhanced systems describes resources that could potentially be explored with advancements in technology which could unlock access to at least 5.16 GW of power (Geothermal Technologies Office 2019). Systems that fall under this category have high reservoir temperatures, but low initial permeabilities and no reservoir water in place, thus they are not able to support commercial flow rates. As temperatures at theses depths can be very high, the integrity of packers, drilling muds as well as other equipment is heavily affected in such hostile conditions (Mondejar and Chamorro 2017). In addition to failing equipment, another challenge that arises is pressure depletion. It has been shown that it takes approximately three times the time of the operational period to replenish 90% of the heat of the reservoir (Mondejar and Chamorro 2017). Even with successful pressure management and equipment staying intact, the circulated water is often unable to maintain hot-rock fracture pathways leading to cool water breakthrough (“Geothermal Well Construction: A Step Change in Oil and Gas Technologies” 2021). Another challenge is that the circulated water can act as a solvent for many minerals which results in plugging of the pores by the transported solids and ultimately a reduction in permeability (Mondejar and Chamorro 2017).

2.2.2 Advanced Geothermal Systems & EGS-CLG hybrids

Challenges concerning the compatibility and thermal properties of water as a working fluid lead to engineers taking a different approach. The development of advanced geothermal systems (AGS), also known as closed loop geothermal systems (CLG), does not require a suitable reservoir with good initial permeability and does not rely on the success of a hydraulic stimulation job. These types of systems use one or more wells that are drilled into zones of high temperature formations in order to circulate a working fluid in a closed loop which is connecting the wells. Through the closed loop the harvested heat can then be utilized for commercial use like district heating, or electricity generation via turbines (“Technology - Eavor - Closed-Loop Geothermal, Unlike Any Other” 2023).

Eavor Technologies is a Canadian based company with the goal of making closed loop radiator systems available for commercialization. By using a thermally insulated drill pipe they are able to drill into deeper and hotter areas while staying in control of bottomhole temperatures (“Technology - Eavor - Closed-Loop Geothermal, Unlike Any Other” 2023). In order to drill vertical wells with multilaterals extending from the junctions, the use of magnetic ranging technology is necessary. This provides an accurate intersection of the wells and efficient connection of one borehole to the other (“Technology - Eavor - Closed-Loop Geothermal, Unlike Any Other” 2023).

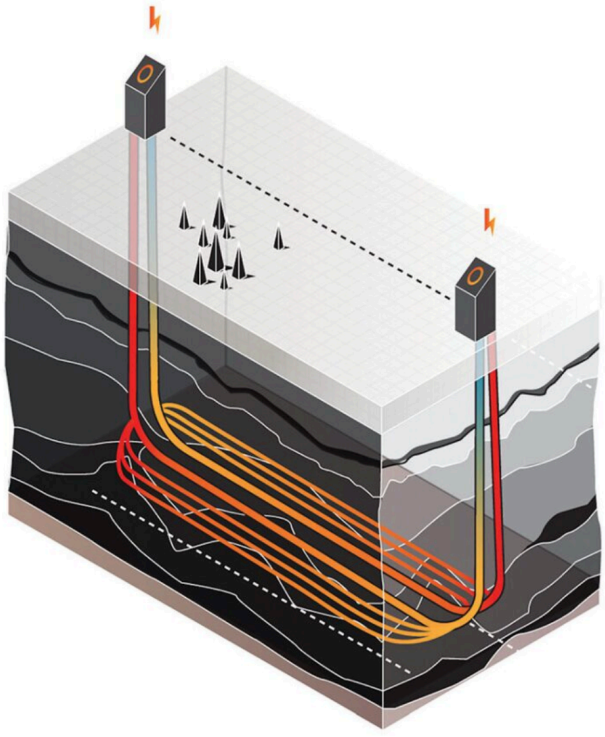

Figure 16. Eavor-Loop™ “radiator” closed loop system. (“Technology - Eavor - Closed-Loop Geothermal, Unlike Any Other” 2023)

After successful completion and connection of the boreholes, the working fluid is injected into the closed loop, whilst being completely isolated from the environment. The hot fluid from the closed loop reaches the surface where it enters an organic Rankine cycle. There, the working fluid from the Rankine cycle is preheated, and through the additional heat of the downhole fluid, is vaporized. The vapor then enters the turbine causing it to rotate and therefore generating electric power. The downhole working fluid is pumped back down into the loop where the cycle is repeated. Closed loop systems are potentially attractive for the application of supercritical CO_2 as a working fluid. The supercritical state of the carbon dioxide creates a strong thermosiphon effect, causing the working fluid to rise on its own, without the need of a pump ("Geothermal Well Construction: A Step Change in Oil and Gas Technologies" 2021). Supercritical carbon dioxide has many advantages when dealing with geothermal energy recovery and will be discussed in further detail in the next chapter 3.

Another approach to increase heat recovery are EGS/CLG hybrid systems. Sage Geosystems™, based in Texas, drills wells from 4 to 6 km total depth and targets areas with bottomhole temperatures of 100°C to approximately 250°C ("Technology - Sage Geosystems™" 2021). Targeted areas include hot-dry-rock reservoirs without the presence of an aquifer. Their geothermal well design is based on a technology called HeatRoot™ design and is based on drilling four laterals with a distance of around 105 meters (350ft) between them ("Geothermal Potential Runs Hot in Texas" 2023). Consequently the goal of HeatRoot™ is to induce a single downward oriented fracture which is at least tens to hundreds of meters deeper than the drilled depth ("Geothermal Well Construction: A Step Change in Oil and Gas Technologies" 2021). Through this increase in depth the circulated fluid within the fractured part of the reservoir is much hotter than the bottomhole temperature of the well itself, and filling up the fractures with a highly conductive and convective slurry, results in them acting as a chimney which delivers the heat to the wellbore ("Geothermal Well Construction: A Step Change in Oil and Gas Technologies" 2021). Via this downward extension of fractures it is possible to keep drilling costs within an economic limit as the necessary drilling depth is reduced drastically ("Technology - Sage Geosystems™" 2021).

Chapter 3

Carbon Dioxide in Geothermal Energy

3.1 Supercritical CO_2

Most of the time carbon dioxide is considered as a useless waste product and large efforts are made in order to establish efficient and economical carbon capture projects. This is done to remove the CO_2 from the atmosphere as a countermeasure against global warming. Most people know carbon dioxide as a gas emitted by humans through the biological breathing cycle, as the waste product of fossil fuels in large industries or, in the form of a solid, as dry ice. However, when supercritical state is reached, the properties and characteristics of carbon dioxide change. Supercritical fluids exist whenever their critical pressure and critical temperature is exceeded, and therefore a region in the phase diagram without phase boundaries is reached. The absence of phase boundaries means that the CO_2 can change instantaneously into either gaseous or liquid phase (Gupta and Vashistha 2016). The properties in the supercritical region are midway between the ones of a liquid and a gas (“Supercritical CO2 Tech Team” 2023) and the existing single phase has a liquid-like density but viscosity and interfacial tension are similar to the ones encountered for a gas (“What Is Supercritical CO2?” 2021).

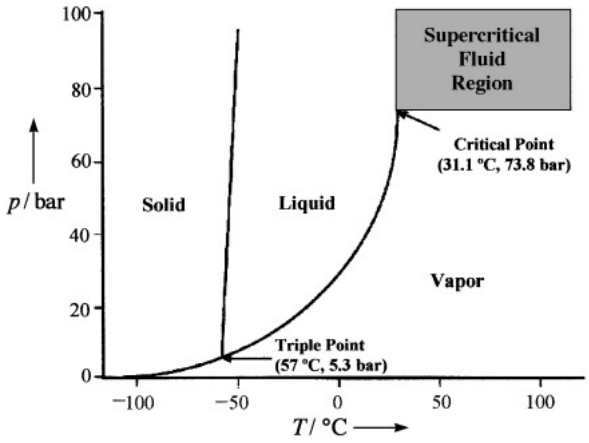

Figure 17. Phase diagram of pure carbon dioxide (Wells and DeSimone 2001)

Figure 17 shows the phase diagram of pure carbon dioxide and the location of the critical point at which supercritical state is reached (T_c=31.1 °C; P_c=73,8 bar). The moderate conditions, at which the critical point occurs, also add to the usability of supercritical CO_2 and allow for safe operating conditions when handling it in the laboratory (Wells and DeSimone 2001). The strong dependence of supercritical CO_2 on temperature and pressure as well as the early presence of the supercritical state at relatively low temperatures lead to it being used in a broad range of industrial applications, including as a geothermal working fluid.

The favorable properties of supercritical CO_2 include the high mobility due to low kinematic viscosity. Kinematic viscosity is defined as the ratio of the dynamic viscosity (μ) of a fluid and the density (ρ) of the fluid (Camuffo 2014). A low kinematic viscosity leads to better heat advection (Gupta and Vashistha 2016) which increases heat extraction efficiency and reduces pressure losses through the rock (Fleming et al. 2022). As mentioned above, the critical point of CO_2 is relatively low when compared to water. This means that the density varies much more with temperatures than the density of water and due to the high compressibility of CO_2 a thermosyphon effect occurs that allows for fluid circulation without the use of a mechanical pump (Gupta and Vashistha 2016). CO_2 also has a lower mineral solubility, which has been mentioned as one of the main issues when maintaining EGS fracture pathways and scaling in equipment, resulting in less scale across the surface facilities and in the pipes (Fleming et al. 2022).

3.2 Carbon Dioxide Plume Geothermal Systems (CPG)

Due to the fact that processes that use CO_2 do not increase the greenhouse effect (Wells and DeSimone 2001) it presents itself as an opportunity to simultaneously capture, store and use it in geothermal power plants. The high density and low viscosity of CO_2 make it a good candidate to use for heat extraction. The supercritical state is reached at early stages of

injection and, under normal hydraulic conditions, the critical pressure can be reached at depths of more than 800 meters (Huenges 2010) meaning that these conditions are already encountered in quite shallow regions. In addition, a subsurface CO_2 energy storage system combined with geothermal energy production can generate more energy than it consumes (Aljughaiman 2022) due to the excess power that is being produced through the geothermal power plant.

In order to understand the terminology, literature differentiates between CO_2-Plume Geothermal (CPG) (Gupta and Vashistha 2016), CO_2-Bulk Energy Storage (CO_2-BES), Compressed CO_2 Energy Storage (CCES) (Aljughaiman 2022) and Flexible CO_2-Plume Geothermal (CPG-F) facilities (Fleming et al. 2022).

The systems which utilize carbon dioxide as working fluids are categorized as carbon dioxide plume geothermal systems or short CPG. As the name already suggests the technology is based on a large CO_2 plume which develops upon sequestration of carbon dioxide which subsequently can be accessed to circulate the working fluid through surface facilities for power production. During stages of energy demand, the CO_2 can be retrieved and used for energy production whereas during off peak hours it can be compressed and injected into the reservoir in order to store it (Katterbauer et al. 2022).

To successfully develop a carbon dioxide plume geothermal (CPG) system four main prerequisites must be in place: natural permeability allowing the carbon dioxide to flow from injector to producer, supercritical state of the CO_2, a low permeability cap rock and, as in any geothermal system, a sufficient reservoir temperature usually in the range of around 100°C (Saar et al. 2012) or when an organic Rankine cycle is utilized, even lower temperatures suffice.

The whole injection and storage cycle can be carbon negative. This is possible via the injection of the CO_2 which is emitted by the compression pumps used during injection in addition to the CO_2 emitted by the industrial emitter (Saar et al. 2012). Through this the reservoir can be re-pressurized and some research has shown that CPG reservoirs show tendencies of sufficient pressure for them to be used for heat extraction even without constant injection of CO_2 (Saar et al. 2012).

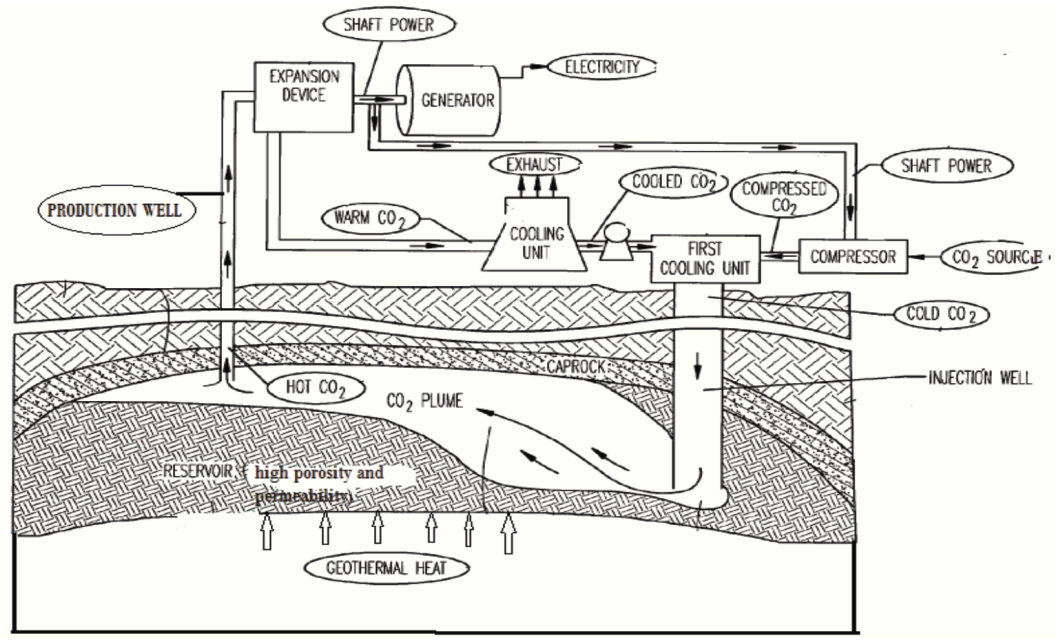

Figure 18. Schematic of a carbon dioxide plume geothermal system including surface facilities (Gupta and Vashistha 2016)

The working principle of a carbon dioxide plume geothermal (CPG) system is illustrated in Figure 18. After successfully capturing the carbon dioxide, it is injected into the formation where it displaces native fluids and, as already mentioned, develops a plume. Due to the difference in density the supercritical CO_2 occupies the upper part of the reservoir, on top of the brine phase, as it is driven up by buoyant forces. While it resides in the reservoir the stored CO_2 is heated up by the in-situ heat of the reservoir. The hot CO_2 can then be produced through a production well, where it will rise to the surface via a very strong thermosyphon effect. Power generation at the surface facilities can then be achieved in two ways. The first method includes a closed loop through which the CO_2 enters a heat exchanger thereby heating up a secondary working fluid which in turn is powering a binary power system or district heating (Gupta and Vashistha 2016). The second method that is in use is very similar to a hydrothermal steam turbine but in the case of CO_2 the fluid expands in a high-pressure turbine causing it to rotate.

3.2.1 CCES, CO_2-BES and Flexible CPG

CCES facilities use multi-layered reservoirs filled with compressed CO_2. Its main use is to act as a 'battery' for solar or wind power via compression and injection of CO_2. CO_2-Bulk Energy storage systems are mainly used to inject, produce, or re-inject CO_2 either, alongside with, or instead of water. This allows for re-pressurization of the reservoir and provides energy storage space utilizing both phases. Another interesting development is the flexible

CO_2 plume geothermal approach. Flexible CPG (CPG-F) consists of one deep reservoir, as in conventional CPG systems, and a second shallow reservoir. After storage in either the deep or the shallow reservoir the CO_2 is heated up and brought to the surface. The hot CO_2 expands through a high-pressure turbine, thus generating power. At this point, some of the non-expanded CO_2 can be reinjected into the shallower reservoir in order to not cause pumping capacity to reach its limit but also reduce cooling due to inefficiencies. The part that is not reinjected into the shallow reservoir passes through a low-pressure turbine for further expansion and, after cooling, will be re-injected into the deeper part of the reservoir. By utilizing the shallow reservoir the CPG system can effectively act as energy storage as well as provide dispatchable power upon demand (Fleming et al. 2022).

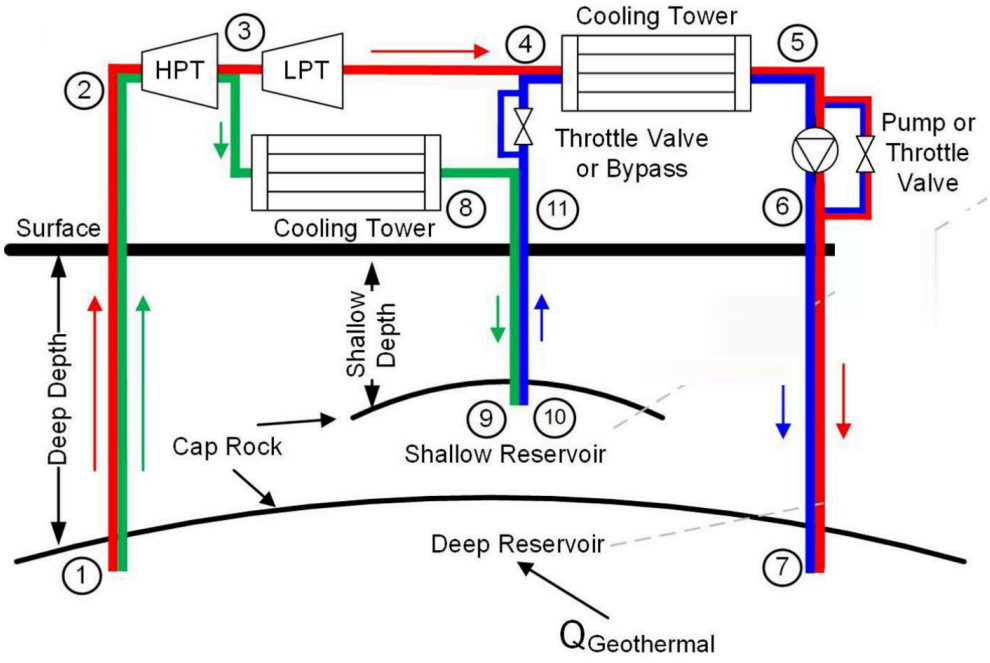

Figure 19. Schematic of a Flexible CO_2 Plume Geothermal System including lines describing dispatchable power (red), energy storage (green) and flexible dispatchable power (blue) (Fleming et al. 2022)

3.2.2 Thermodynamics of Flexible CPG (CPG-F)

From a thermodynamic point of view, it is of advantage to consider the Rankine cycle (Figure 20). The illustration shows an ideal repeatable process in which the surface equipment such as pump, turbine and compressors work isentropically. In reality a completely reversible process is not possible causing entropy to increase which makes this process adiabatic (Aljughaiman 2022). Since the flexible CPG system can be considered a combination of Compressed CO_2 Energy Storage (CCES) and CPG the processes can be looked at as two separate cycles.

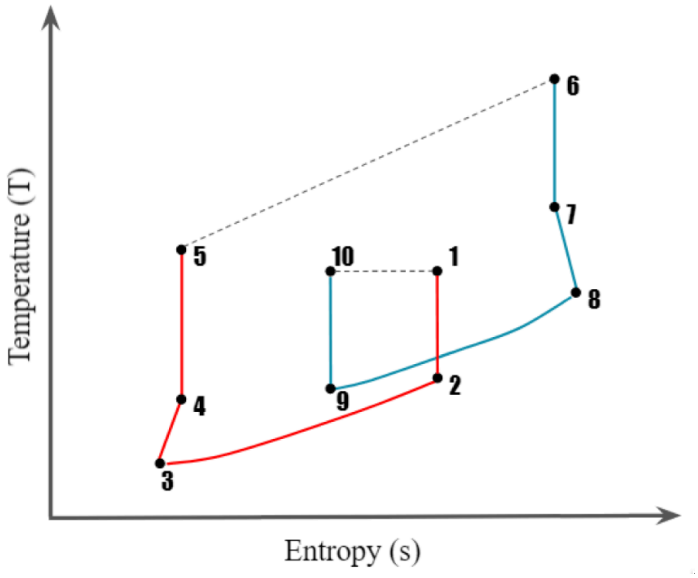

Figure 20. Rankine Cycle showing energy storage mode in red (1-5) and energy generation in blue (6-10) (Aljughaiman 2022)

The energy storage mode, held in red, starts by the injection of CO_2 into the shallow reservoir. As a next step it is brought to the surface causing a drop in temperature at constant entropy (isentropic) (Points 1-2). Once at the surface the carbon dioxide enters the cooling tower and is cooled at constant pressure causing an increase in density (2-3). After cooling, the CO_2 is still supercritical and compressed adiabatically (without transferring heat to the environment) (3-4) and injected into the deep reservoir (4-5). At this point the stored CO_2 is heated up in the reservoir. Point 6 represents the starting point for energy generation at which the stored CO_2 is hot enough to provide energy. Bringing the supercritical CO_2 to the surface isentropically causes it to drop in temperature slightly (6-7). When entering the turbine, the CO_2 is adiabatically expanded in the turbine causing it to rotate and therefore creating energy (7-8). Point 8 to point 9 describes the cooling process the same way as in the energy storage mode, thus increasing the density and preparing it for reinjection (9-10). (Aljughaiman 2022)

3.2.3 EGS vs. CPG

When comparing EGS with CPG, it can be said that CPG's main advantage is not requiring hydraulic stimulation. Therefore, no seismicity is induced into the formation which makes it environmentally less controversial. CPG relies mainly on the availability of highly porous formations as well as high permeabilities. These systems are often encountered in abandoned hydrocarbon reservoirs and are widely available around the globe. However, as mentioned earlier, the necessity of a suitable seal rock is obvious, due to the buoyancy driving up the CO_2 resulting in a significant leakage risk if not contained properly. Such considerations must be taken into account when evaluating the technical and economic feasibility of CPG projects.

3.3 Volcanic Reservoirs

Supercritical reservoirs are part of unconventional geothermal systems. They exist when high temperature gradients as well as sufficiently high pressures occur, which leads to the respective fluid to reach supercritical state. Such reservoirs are hosting fluids above their critical point, resulting in the fluid to merge from a two-phase system, consisting of liquid and vapor, into one single-phase system in supercritical state (Elders and Moore 2016).

Regions of ocean spreading centers result in extensional environments, where hot magma intrudes through the spreading crust (Glassley 2010) and thus higher temperatures at shallower depths are present. The thinner continental crust leads to more heat that is transported conductively. Conduction itself can be described as the transfer of heat through a solid substance or material, from a geological point of view that is the earth's crust. It is highly dependent on the minerals that are present in the crust, therefore conduction differs throughout the continental crust and settings of highly conductive fractured granites are favored for geothermal exploitation (Huenges 2010).

Convective heat transfer processes are processes that move heat in the form of hot material or moving particles (Huenges 2010). A typical example of convection is the intrusion and formation of a dike volcano. When magma rises through a fracture or through existing rock it transfers heat convectively from a deeper to a shallower zone. When the heat of the magma is dissipated into the surrounding rock, the magmatic intrusion cools down and solidifies resulting in the formation of a volcanic dyke ("USGS: Volcano Hazards Program Glossary - Dike" 2015). Such dyke systems lead to extreme geothermal gradients, reaching up to 500°C in depths of around 5 km (Huenges 2010). On the other hand, dikes usually come along with hotspots, which are magmatic hot bodies that either rise all the way to the surface and show as volcanoes or stay beneath the surface also causing very high geothermal gradients. Usually hotspots are located far from plate boundaries ("Hot Spots" 2022). However, in the case of Iceland, the geology was interpreted as a superposition of a hotspot on the mid-Atlantic ridge (Huenges 2010) with the North American plate to its left and the Eurasian plate to its right.

3.4 Geothermal Resources of Iceland

As mentioned above, the geological setting of Iceland is special and results in temperature gradients reaching from 50°C/km up to 150°C/km (Huenges 2010). The specialty of Iceland's geographic location can also be seen in Figure 21, which shows the mid-Atlantic ridge as well as the active zones of rifting and volcanism. The mid-Atlantic ridge reaches the surface at the southwestern tip of the Reykjanes Peninsula. As mentioned above, the diverging plates lead to volcanic activities and, in the case of Reykjanes, result in the creation of three active volcanic

systems (Spice 2021). The Reykjanes volcanic belt is aligned northeast-southwest and with the names of the three systems being Reykjanes, Krysuvik and Brennisteinsfjöll (Spice 2021).

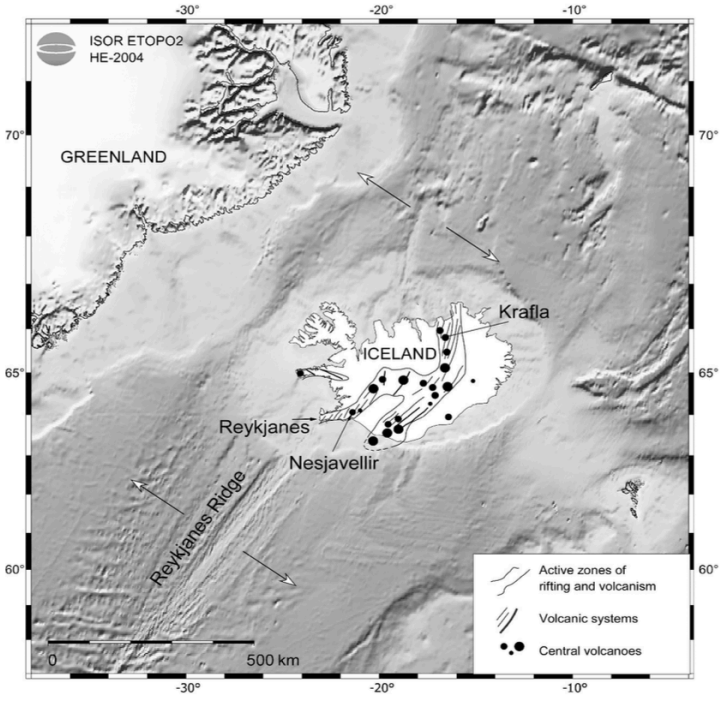

Figure 21. Iceland on the Mid-Atlantic Ridge leading through the Reykjanes region. Indicators show active rifting zones and volcanoes (Friðleifsson et al. 2017)

In addition to the extensional faulting which occurs due to the plate movement, a strike-slip fault can be observed due to lateral movement of the tectonic plates against each other. This leads to a potentially high seismic activity throughout a belt that extends from the west to the east (Spice 2021). The high temperatures at relatively shallow depths across Iceland make it a good potential candidate to explore for the development of high-temperature hydrothermal supercritical reservoirs, which is why the Icelandic Deep Drilling Project (IDDP) has been launched. The project is part of a bigger effort of the European Union which has funded the "DEEPEGS" initiative to find and develop high temperature heat mining operations and further explore the limits and opportunities of enhanced geothermal systems. With its final meeting in April of 2020 "DEEPEGS" was stopped, leaving behind individual projects like IDDP ("Season Greetings 2020 Test - IDDP" 2022).

The IDDP is a project with the objective to locate and investigate potential sites for deep enhanced geothermal systems and to demonstrate their feasibility for heat extraction ("Work Packages" 2016). For this project the targets are high-temperature supercritical reservoir in which temperatures and pressures are above the critical point of pure water (374°C, 22.1 MPa) (Wang et al. 2022). Operating a geothermal system in these conditions has the potential to extract more heat as the water's viscosity becomes low and specific enthalpy increases

(Wang et al. 2022) and could generate power outputs greater than traditional high-temperature geothermal resources which range only from 240°C-340°C (Friðleifsson et al. 2017). However, finding reservoirs with temperatures above 400°C can be quite challenging. Feasibility not only has to be considered from an economic point of view but also from a technological point of view. Temperatures of several hundred degrees Celsius exert an extreme amount of stress on the equipment and drilling in the vicinity of magmatic bodies can present many different challenges.

After its founding in the year 2000, the Icelandic Deep Drilling Project committee chose three main prospects to go into the next stage, Krafla located in the northeast of Iceland, Nesjavellir (part of the Hengill volcano) and Reykjanes, in the southwest (Figure 21) (Friðleifsson et al. 2017). The first well that was drilled was called the IDDP-1 well in the Krafla Caldera in 2008. The well was drilled until 2100 m TVD where drilling had to be stopped due to the encounter of 900°C hot rhyolite magma (Friðleifsson et al. 2017). Even though the well was tested and flowing, the reservoir pressure of 14 MPa that was encountered at the 2.1 km, was insufficient to produce supercritical water and instead had it producing superheated steam at 452°C (Friðleifsson et al. 2017). In addition to the early drilling stoppage, other mechanical failures occurred in the testing stage which led to and abandonment of the well.

A promising candidate for a feasible supercritical hydrothermal system is the IDDP-2 well. Drilling started in 2015 based on an already existing 2500 m deep production well (RN-15) ultimately resulting in a slightly inclined geothermal well at a true vertical depth of 4.5 km. The well is located on the north side of the Reykjanes drill (Figure 22) field and by drilling to a depth deeper than 4 km it could be observed that there is a hydrothermal reservoir at supercritical condition underneath the traditional geothermal well field. In comparison the Krafla caldera where the critical point of water is equal to the one of fresh water (374°C, 22.1MPa) the Reykjanes system is recharged by seawater. Due to the seawater recharge, and consequently increased salinity, the critical point shifts to 406°C at 29.8 MPa (Friðleifsson et al. 2017).

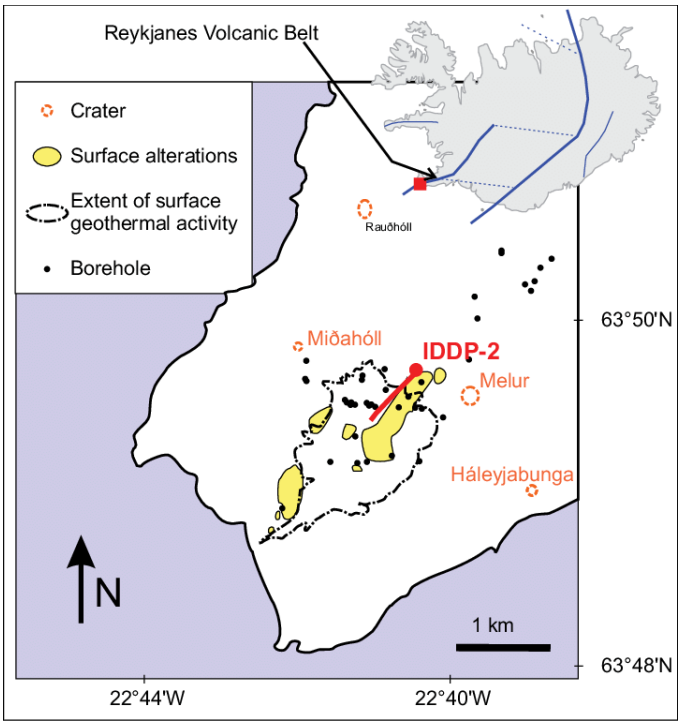

Figure 22. Location and direction of the IDDP-2 well in the northeast of the Reykjanes drill field (Bali et al. 2020)

Chapter 4

Methodology

As mentioned previously the success of the Icelandic Deep Drilling Project creates new ways for development of geothermal resources. Supercritical hydrothermal resources could lead to improved heat recovery, whilst also providing an opportunity for CO_2 sequestration. The exploration and development of such high temperature reservoirs provide the ability to inject the CO_2 into the reservoir to store and re-pressurize the geothermal resource. In contrast to CPG systems, the supercritical state of the resident water leads to the density of the water being lower than the injected CO_2 causing the carbon dioxide to sink (Parisio and Vilarrasa 2022). The result is a geological storage facility of CO_2 which is not dependent on the existence of a seal rock as the CO_2 is contained underneath the resident brine.

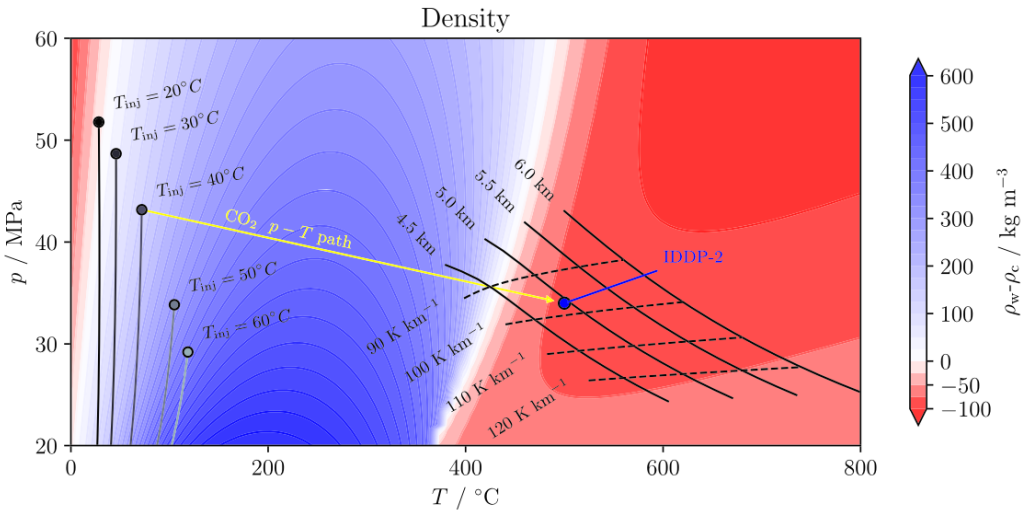

Figure 23. Density difference map showing the conditions present in the IDDP-2 well and the limits when CO_2 starts to sink. (Parisio and Vilarrasa 2020)

Figure 23 shows a density difference map between water and CO_2 describing the conditions at which the water reaches lower density than the supercritical CO_2. As indicated by the blue dot

the conditions for the IDDP-2 well are well above the requirements for CO_2 to sink, reducing the risk for buoyancy driven leakage. Parisio and Vilarrasa (2020) investigated the sinking potential according to different injection temperatures at the wellhead and determined that the optimum conditions for CO_2 sinking potential corresponds to temperature gradients in the range of 90-120 K/km at depths deeper than 5 km.

The hypothesis for their simulation assumes that the flow in the wellbore itself is isenthalpic and fixed at the corresponding wellhead conditions which leads to a loss of the transient effects after injection is started. However, the transient effects of the cold CO_2 injection usually only last a few days after which an equilibrium is reached after a cold annulus forms around the wellbore (Parisio and Vilarrasa 2020). Therefore, there is no heat transfer from the surrounding rock with the wellbore and the process becomes adiabatic.

The assumption that is used describing the reservoir features is that there is a confined aquifer in place, which is limited by the geologic features of volcanic regions. Those regions can be very diverse in whether there is low permeability structure, faults, magmatic intrusions or chemically altered layers being present (Parisio and Vilarrasa 2020). Due to this uncertainty the injection rate must be chosen carefully in order not to activate any faults and induce seismicity.

The investigation by Parisio and Vilarrasa provides the basis for the simulations performed in this thesis, however as injection and downhole conditions variations are highly non-linear and CO_2 temperature is highly governed by compression, the initial conditions used for this thesis are set at bottomhole conditions and, in contrast to Parisio and Vilarrasa, not at the wellhead. Additional findings by Parisio and Vilarrasa (2020), are compared to the results from the following simulations, and will be further discussed in the discussion section.

The following chapters introduce the software that has been used as well as the governing equations behind it. It must be noted that the calculations within the MOOSE environment are performed in the background of the program, which makes a lot of the computations not visible, therefore the overall computations are described by the equations found in the documentation. At the end of this chapter the experimental setup is introduced and the input values for the simulations are given.

4.1 MOOSE

The program that is being used for the simulation is called MOOSE, which is a Multiphysics Object-Oriented Simulation Environment. MOOSE was first developed by the Idaho National Library as a tool designed to solve computational engineering problems while simultaneously reducing expenses and time (Lindsay et al. 2022). By using an object-oriented programming

methodology, it is designed to build the bridge between different softwares. The solver interface is given by the toolkit “PETSc” which is a numerical solver package for solving matrices while “libMesh”, a GitHub library, supports multidimensional steady state and transient simulations (“LibMesh - A C++ Finite Element Library” 2023). LibMesh provides the finite element method including the shape functions and mesh implementation from Gmsh (Lindsay et al. 2022).

The main advantage of an object-oriented pluggable system are the broad possibilities for combining different modules. The user is not only able to define and input their individual equations via C++ language but can also use common physics modules such as: heat conduction, solid mechanics, porous flow, and chemical reactions. Combining the desired physics modules with predefined material modules as well as a boundary condition module makes it possible to structure the system to the users’ needs with the ability to expand whenever necessary.

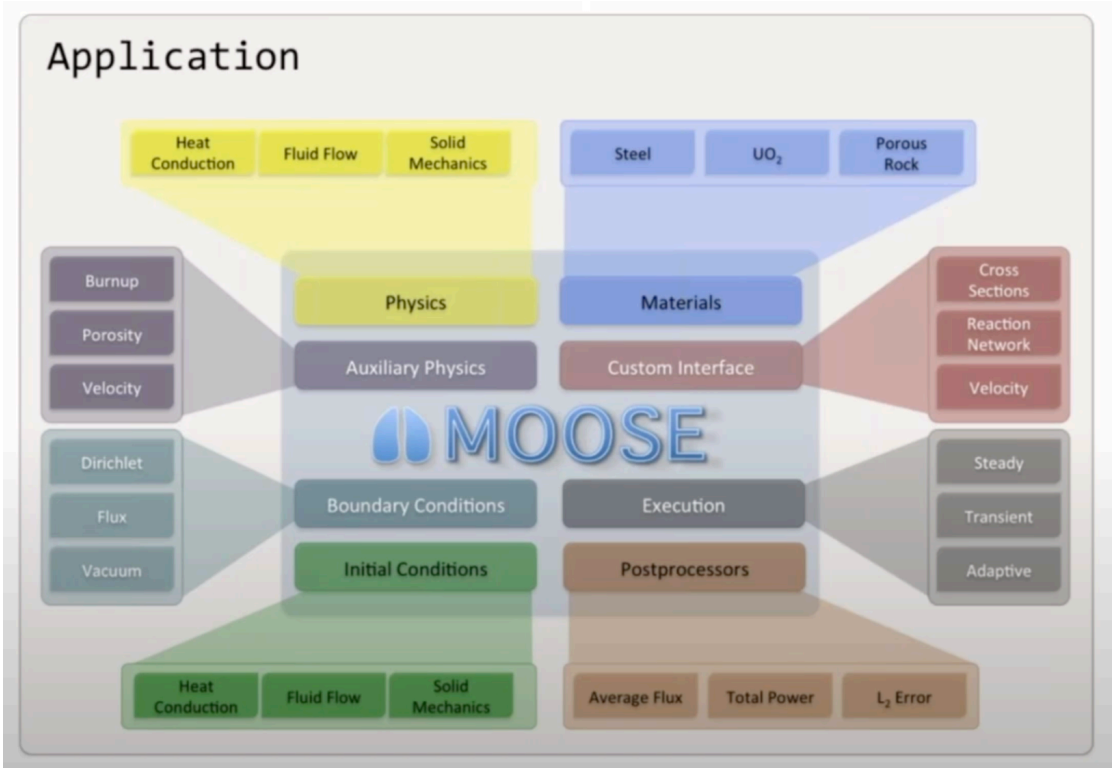

Figure 24. Visualization of the MOOSE environment (Lindsay et al. 2022)

4.2 Kernels

The modular approach and plugging of modules into your model is also maintained in the porous flow module. The module holds a library of physical equations for fluids and heat flow in porous media. The different modules were developed to keep the equations of the modules in a general manner. Thus, the equations are capable of solving problems with any

number of phases and fluid components (Wilkins, Green, and Ennis-King 2021; 2020; Slaughter et al. 2021). In order to import the different differential equations describing the porous flow model, so-called “Kernels” are defined in the input file.

4.2.1 Fluid Flow

The first Kernel that is introduced is fluid flow. Fluid flow within the model is governed by the mass conservation for different fluids and described by the continuity equation.

$$0 = \frac{\partial M^{\kappa}}{\partial t} + M^{\kappa}\nabla \cdot v_s + \nabla \cdot F^{\kappa} + \Lambda M^{\kappa} - \phi I_{Chem} - q^{\kappa} \qquad \text{(Eq. 1)}$$

With M being the mass of fluid per bulk volume, v_s the velocity of the porous solid skeleton also expressed as the derivative of the solid mechanical displacement vector $\frac{\partial u}{\partial t}$.

F is the fluid flux which is represented by the sum of the advective (Darcy) flux and diffusive-and-dispersive flux. Λ is a radioactive decay rate and ϕI_{Chem} represents chemical precipitation and dissolution.

κ represents a parametrization of the species in case a component can change phase. In the case of a single-phase fluid κ is set to 0. For the fluid model we are using, the κ is set to 1.

When considering no radioactive decay as well as no chemical precipitation and dissolution in our model then Equation (1) reduces to

$$0 = \frac{\partial M^{\kappa}}{\partial t} + \nabla \cdot F^{\kappa} - q^{\kappa} \quad \text{(Eq. 2)}$$

The fluid mass for water is given by

$$M_{H2O} = \phi S_{H2o} \rho_{H2o} \quad \text{(Eq. 3)}$$

likewise for CO2

$$M_{CO2} = \phi S_{CO2} \rho_{CO2} \quad \text{(Eq. 4)}$$

Flux is given to be the sum of advective and diffusive-dispersive flux. Equation (5) describes flux in its general form, but in our model, the second term for diffusion and dispersion flux can be omitted.

$$F^{\kappa} = \sum_{\beta} \chi_{\beta}^{\kappa} \boldsymbol{F}_{\beta}^{advective} + \boldsymbol{F}_{diffusion+dispersion}^{\kappa} \quad \text{(Eq. 5)}$$

Advective flux describes the movement of mass entrained in the flow (Fitts 2013) and is governed by Darcy's law with each phase obeying Darcy's law. According to this the flow rate at any point in the reservoir is given by the pressure gradient each of each of the fluid phases, viscosity and relative permeability (Cleveland and Ayres 2004). Absolute permeabilities are usually considered as a tensor, as it differs in vertical and lateral directions, but due to difficult parameter estimation it is treated as a scalar most of the time. Relative permeability itself is a function of the saturations (Wilkins, Green, and Ennis-King 2021;

2020; Slaughter et al. 2021). Gravity effect acting on the fluid is accounted for in the advective part as well.

$$F_{\beta}^{advective} = -\rho_{\beta}\frac{k\,k_{r,\beta}}{\mu_{\beta}}\left(\nabla P_{\beta} - \rho_{\beta} g\right) \quad \text{(Eq. 6)}$$

The pressure for each phase β is the capillary pressure (as a function of saturation) added to a reference pressure P: $P_{\beta} = P + P_{c,\beta}$ (Eq. 7). As mentioned earlier, diffusion-dispersion flux will not be considered and the Flux equation reduces to the Kernel "PorousFlowAdvectiveFlux" (Wilkins, Green, and Ennis-King 2021; 2020; Slaughter et al. 2021):

$$-\nabla\sum_{\beta}\chi_{\beta}^{\kappa}\rho_{\beta}\frac{kk_{r,\beta}}{\mu_{\beta}}\left(\nabla P_{\beta} - \rho_{\beta} g\right) \quad \text{(Eq. 8)}$$

4.2.2 Mass Density

Mass flow rates for water and CO_2 are computed using the "PorousFlowMassTimeDerivative" Kernel, from Equation (9) (Wilkins, Green, and Ennis-King 2021; 2020; Slaughter et al. 2021).

$$\dot{m} = \frac{\partial}{\partial t}\left(\phi\sum_{\beta} S_{\beta}\rho_{\beta}\,\chi_{\beta}^{\kappa}\right) \quad \text{(Eq. 9)}$$

4.2.3 Heat Flow

In order for the energy conservation of heat to be valid, the continuity equation is used in the rock fluid system

$$0 = \frac{\partial\varepsilon}{\partial t} + \varepsilon\nabla\cdot v_s + \nabla\cdot F^T - \nu(1-\phi)\sigma_{ij}^{eff}\frac{\partial}{\partial t}\epsilon_{ij}^{plastic} - q^T \quad \text{(Eq. 10)}$$

with

$$\varepsilon \dots Heat\ energy\ per\ volume$$

$$v_s \dots Velocity\ of\ the\ porous\ solid\ skeleton$$

$$F^T \dots Heat\ flux$$

$$\nu \dots Ratio\ of\ plastic\ deformation\ energy\ being\ transferred\ to\ heat\ energy$$

$$\sigma_{ij}^{eff} \dots Effective\ stress$$

$$\epsilon_{ij}^{plastic} \dots Plastic\ strain$$

$$q^T \dots Heat\ source\ term$$

When removing heat volumetric expansion ($\varepsilon\nabla \cdot v_s$) and plastic heat energy ($-\nu(1-\phi)\sigma_{ij}^{eff}\frac{\partial}{\partial t}\epsilon_{ij}^{plastic}$) from the continuity equation, then heat flow is mainly dependent on heat conduction and advection.

In order to get the equations for the heat flux in our system, we use the heat flux equation as the sum of heat conduction and convection.

$$F^T = -\lambda\nabla\mathrm{T} + \sum_{\beta} h_\beta F_\beta \qquad \text{(Eq. 11)}$$

Where λ is the tensorial thermal conductivity of the rock-fluid system. It is usually a function of the thermal conductivities of rock and fluid phases. The term h_β in the summation operator, stands for the specific enthalpy of the phase β (Wilkins, Green, and Ennis-King 2021; 2020; Slaughter et al. 2021).

As we know from Equation (6), the term F_β (Eq.11) is the advective Darcy flux. In the input file for our model, the total heat flux (Eq. 11) is imported as two separate Kernels

“PorousFlowHeat Conduction”

$$-\nabla \cdot (\lambda\nabla\mathrm{T}) \qquad \text{(Eq. 12)}$$

“PorousFlowHeatAdvection”

$$-\nabla \cdot \sum_{\beta} h_\beta\, \rho_\beta \frac{k\, k_{r,\beta}}{\mu_\beta}\left(\nabla P_\beta - \rho_\beta g\right) \qquad \text{(Eq. 13)}$$

4.2.4 Energy Density

The final Kernel, that is being imported is called "PorousFlowEnergyTimeDerivative" (Wilkins, Green, and Ennis-King 2021; 2020; Slaughter et al. 2021) and represents the time derivative of the energy density ε.

$$\varepsilon = (1-\phi)\rho_R C_R T + \phi \sum_\beta S_\beta \rho_\beta \varepsilon_\beta + \sum_\beta (1-\phi)\rho^R \, \varepsilon_{abs\,\kappa} A^\kappa \qquad \text{(Eq. 14)}$$

with the notation

$$\phi \ldots Porosity$$

$$\rho_R \ldots Grain\ density$$

$$C_R \ldots Specific\ heat\ capacity\ of\ rock$$

$$T \ldots Temperature$$

$$S_\beta \ldots Saturation\ of\ phase\ \beta$$

$$\rho_\beta \ldots Density\ of\ phase\ \beta$$

$$\varepsilon_\beta \ldots Internal\ energy\ in\ phase\ \beta$$

$$\varepsilon_{abs\,\kappa} \ldots Internal\ energy\ of\ the\ absorbed\ species$$

"PorousFlowEnergyTimeDerivative"

$$\frac{\partial}{\partial t}\left((1-\phi)\rho_R C_R T + \phi \sum_\beta S_\beta \rho_\beta \varepsilon_\beta\right) \qquad \text{(Eq. 15)}$$

4.3 Fluid Properties

4.3.1 Water and Steam Properties

The water and steam properties that are being used are according to the International Association for the Properties of Water and Steam (IAPWS). This formulation is called the Industrial Formulation of 1997 and is split into five regions in the phase diagram. The method itself calculates the properties of water and steam by using temperature and pressure as the input (Slaughter et al. 2021).

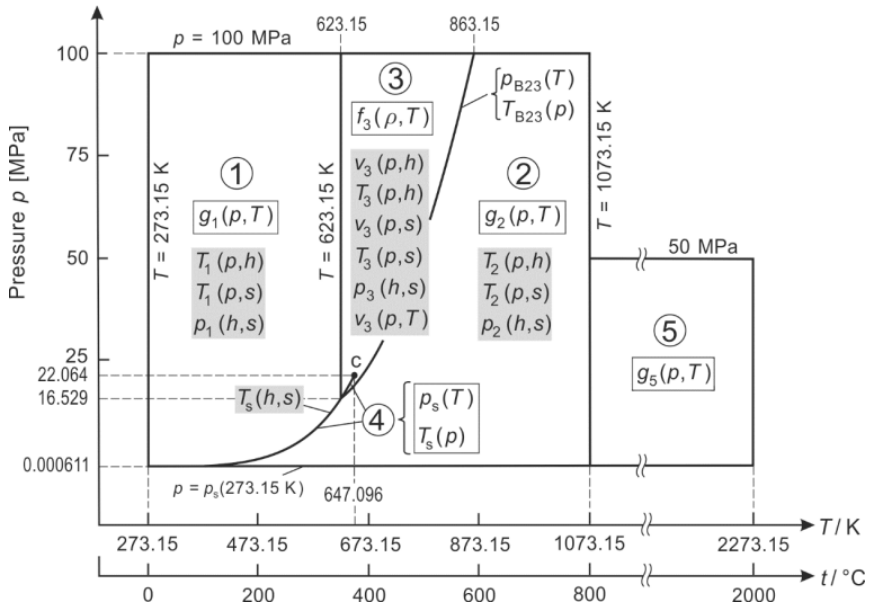

Figure 25: IAPWS – IF97 phase diagram split into five regions of validity (Wagner et al. 2000)

Figure 25 shows the entire range of validity for the industrial formulation. When computing the properties it is important to note that regions 1 & 2 are calculated by using the fundamental equation for the specific Gibbs free energy, while region 3 is using the fundamental equation for the specific Helmholtz free energy (Wagner et al. 2000). By using the Helmholtz free energy, which is a function of density and temperature, it leads to high computer resource usage and is very time consuming as it solves for density iteratively using temperature and pressure. To avoid large computation times and iteration, the fluid model we are using takes advantage of the backwards equations. These equations were designed for each of the sections from 1 to 4 and are a combination of different variables for each region. In our case the backwards equations that are applied to region 3 are equations in the form of:

Table 2: Backwards equations for region 3 of the phase diagram of water (Wagner et al. 2000)

Function	
T(p,h)	Temperature as a function of pressure & enthalpy
v(p,h)	Specific volume as a function of pressure & enthalpy
T(p,s)	Temperature as a function of pressure & entropy
v(p,s)	Specific volume as a function of pressure & entropy

p(h,s)	Pressure as a function of enthalpy & entropy
v(p,T)	Specific volume as a function of pressure & Temperature

By using backward equation v(p,T) in range 3, all other properties in addition to the specific volume can be calculated without iteration which decreases calculation time drastically (Wagner et al. 2000).

Table 3: Water and steam properties according to the IAPWS Industrial Formulation 1997 (Slaughter et al. 2021)

Property	**Value**
Molar mass	0.018015 kg/mol
Critical temperature	647.096 K
Critical pressure	22.064 MPa
Critical density	322.0 kg/m^3
Triple point temperature	273.15 K
Triple point pressure	611.657 Pa

Viscosity and thermal conductivities are calculated using the IAPWS 2008 and IAPS 1985 formulations.

When it comes to application of the IAPWS-IF97 formulation, which we are using in our input file, it has to be noted that the range of validity for application of the formulation is: 273.15 K ≤ T ≤ 1073.15 K for pressures below 100 MPa and 1073.15 K ≤ T ≤ 2273.15 K for pressures below or equal to 50 MPa (Slaughter et al. 2021).

4.3.2 CO2 fluid properties

MOOSE uses CO_2 properties that are based on the Span and Wagner equation of state. Span and Wagner is suitable for use when dealing with supercritical CO_2 as it is fitted to experimental data such as the thermal properties of the single phase region, liquid-vapor saturation curve, speed of sound, specific heat capacities, specific internal energy as well as the Joule-Thomson coefficient (Giljarhus, Munkejord, and Skaugen 2012). The equation itself

is based on the Helmholtz free energy and is quite demanding of computational resources as the density and temperature are used through iterating (Slaughter et al. 2021).

The MOOSE CO_2 fluid properties module uses pressure and temperature as the input and subsequently calculates the density iteratively, which is used to calculate other properties such as internal energy (Slaughter et al. 2021). The MOOSE module also uses thermal conductivity and calculates the dissolution of CO_2 in water by using Henry's law (Slaughter et al. 2021).

Viscosity is calculated using a method developed by Fenghour et al. (1998) which is the function $\eta(\rho, T)$ (Fenghour, Wakeham, and Vesovic 1998)

$$\eta(\rho, T) = \eta_0(T) + \Delta\eta(\rho, T) + \Delta\eta_c(\rho, T) \quad \text{(Eq. 16)}$$

where

$\eta_0(T)$ … viscosity in the zero-density limit

$\Delta\eta(\rho, T)$ … excess viscosity representing the increase in viscosity at elevated density

$\Delta\eta_c(\rho, T)$ ... term accounting for the increase in viscosity around the critical point.

Table 4 shows the critical values for CO_2 and as well as triple point temperature and pressure that are being used in the module:

Table 4: CO_2 fluid properties used in the "CO2FluidProperties" module in MOOSE (Slaughter et al. 2021)

Property	**Value**
Molar mass	0.0440098 kg/mol
Critical temperature	304.1282 K
Critical pressure	7.3773 MPa
Critical density	467.6 kg/m^3
Triple point temperature	216.592 K
Triple point pressure	0.51795 MPa

Like the water fluid properties module, the CO_2 properties module has a range of validity, which is: 216.592 K ≤ T ≤ 1100 K for pressures below 800 MPa (Slaughter et al. 2021).

4.4 Experimental Setup

4.4.1 Mesh

The mesh itself is a 2D mesh which was constructed using the software Gmsh. It has a width of 800 meters with a reservoir thickness of 1050 meters. As can be seen in Figure 25, one vertical and two horizontal dividers were added to provide flexibility in case the refinement needs to be adjusted in the different areas of the reservoir.

The injection well is a horizontal well and is placed on the right-hand side of the mesh at the coordinates x = 800, y = 525 and z = 0. Production occurs opposite of the injector at the coordinates x = 0, y = 525 and z = 0. The mesh provides a horizontal view of the reservoir in order to observe the CO_2 plume movement from right to left.

By placing the injector and producer at half of the reservoir thickness, it is ensured that the full plume development can be observed, and the buoyancy effects can be thoroughly investigated.

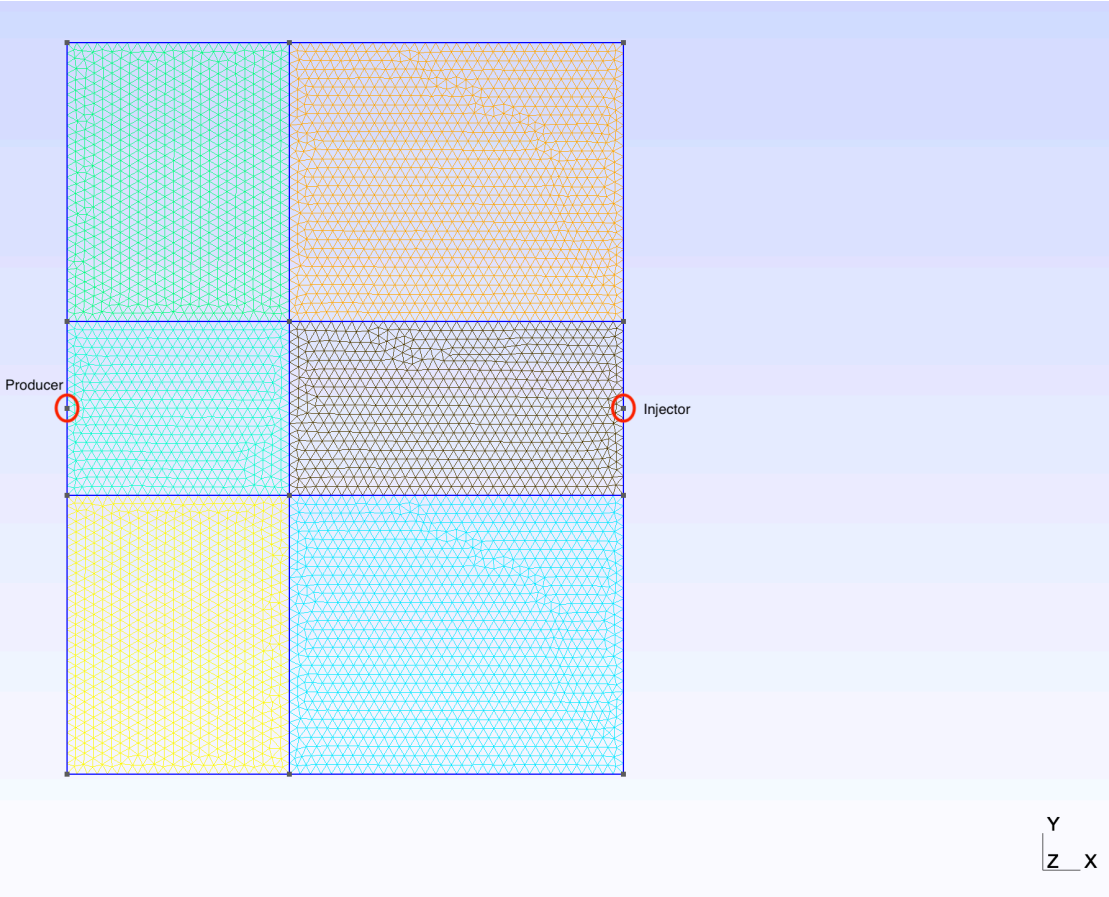

Figure 26. The mesh consists of one vertical divider and two horizontal dividers to provide flexibility if the mesh is too fine or too coarse. The pictured reservoir is 800m in width and 1025m in height.

4.4.2 Boundary Conditions

When dealing with simulations in fluid dynamics one of the main challenges is to set up the model so that it represents the real-life scenario as close as possible. The challenge starts when trying to describe flow either at a natural boundary, such as a wall, or at the truncation of the domain which is an artificial boundary of the moving fluid. Other boundary conditions are: injection boundary, symmetry boundary, coordinate cut and periodic boundary, boundary between blocks, inflow and outflow in internal flows (Blazek 2005).

These conditions require careful numerical treatment, as an improper implementation will result in an inaccurate simulation, instability of the simulation and slow convergence (Blazek 2005).

4.4.2.1 Dirichlet Boundary Conditions

A Dirichlet problem in mathematics is a problem in which the function of the governing partial differential equation at the specified domain boundary needs to be found (Wilkins, Green, and Ennis-King 2021; 2020; Slaughter et al. 2021). In general, Dirichlet boundary conditions describe the numerical value that the variable at the domain boundary should assume when solving the governing differential equation.

As can be seen in the input file, the boundary conditions that were set are as follows:

Table 5: Boundary conditions applied in the simulation model

Boundary Condition Location	Variable
Top & Bottom Reservoir Boundary	Temperature = 773.15 K (500°C)
Top Reservoir Boundary	Pressure = 31 MPa

Initially, the selected boundary was a no flow boundary at the top which represents the cap rock present in the Reykjanes, IDDP-2 reservoir. However, the initial simulations with this boundary resulted in a faulty pressure profile. This problem was solved by setting up an equilibration file which will be discussed more thoroughly in the Results section of this thesis. The top reservoir boundary is a constant pressure boundary which corresponds to the hydrostatic pressure at the top of the reservoir.

4.4.3 Injection and Production Well Implementation

In order to simulate fluid injection into our reservoir and also produce from it we have to implement injection and production processes that describe our model. Sources and sinks are implemented in MOOSE as "DiracKernels" which are point source and point sink elements. Fluid injection is performed using the "PorousFlowSquarePulsePointSource" module. This implements a constant mass point source which adds fluid to the system at a specified point defined by its coordinates (Wilkins, Green, and Ennis-King 2021; 2020). Whether the point is acting as a source, or a sink depends on the sign and is positive when used as a source and negative for a sink. The positive mass flux, fixed at 6 kg/s in our case, indicates that we use the "PorousFlowSquarePulsePointSource" as a source. As our model is a 2D representation of the reservoir, and the mass flux is an extensive property it has to be divided by 1000 in order to reach a conversion to mass per unit area (kg/m^2).

While it might seem intuitive to change the sign of the mass flux and thus creating a sink, a more accurate way is to use a different module. The "PorousFlowPeacemanBorehole" module allows for implementation of production wells producing water as well as CO_2. It is simulating a horizontal wellbore represented by a polyline made up by a sequence of points (Wilkins, Green, and Ennis-King 2021; 2020; Slaughter et al. 2021). When analyzing the resulting profiles in ParaView, the figures then represent the xy-plane perpendicular to the wellbore orientation (z-Axis).

Peaceman writes fluid flux as the following function of pressure (Wilkins, Green, and Ennis-King 2021; 2020; Slaughter et al. 2021)

$$f(P_i, x_i) = W|C|\frac{k_r \rho}{\mu}(P_i - P_{wellbore}) \qquad \text{(Eq. 17)}$$

In order to simulate geothermal fluid production, we also need to define functions that remove fluid from the system. This is done for the water as well as the CO_2 by defining the bottomhole pressure, given at 30 MPa, acting at the sink.

Bottomhole pressure is inserted into the wellbore pressure formula

$$P_{wellbore}(x_i) = P_{bottom} + \gamma \cdot (x_i - x_i^{bottom}) \qquad \text{(Eq. 18)}$$

This results in the wellbore pressure accounting for gravitational head in the location x_i, since gravitational effects are accounted for by the weight vector γ.

The term $\frac{k_r \rho}{\mu}$, in Equation (17), refers to the mobility multiplied by the density (Satter and Iqbal 2016), which must be included when performing fluid simulations using the Peaceman

fluid flux equation. Adding the character C into the input file of the respective wellbore is another way to set the well to be either an injector or a producer.

$$Sink\ (Producer): C = 1\ for\ P > P_{wellbore}\ ; otherwise\ C = 0$$

$$Source\ (Injector): C = -1\ for\ P < P_{wellbore}; otherwise\ C = 0$$

The well constant W (Eq. 17) is a length measurement, and the porous flow module automatically computes it from the information entered into the plain text input file. Important to note is that in order for this equation to be valid the borehole must be oriented into the z-direction (Wilkins, Green, and Ennis-King 2021; 2020; Slaughter et al. 2021).

$$W = 2\pi\sqrt{k_{xx}k_{yy}}L_z/\ln\left({}^{r_e}/_{r_{bh}}\right) \quad \text{(Eq. 19)}$$

$$k_{xx}, k_{yy} \ldots diagonal\ components\ of\ the\ permeability\ tensor\ in\ the\ (x,y) plane$$

$$L_z \ldots length\ of\ the\ borehole$$

$$r_e \ldots effective\ radius\ of\ the\ borehole$$

$$r_{bh} \ldots borehole\ radius\ from\ the\ plain\ text\ file$$

The effective radius of the borehole can either be determined by multiplying the horizontal polyline section of the borehole (which is simulating the perforated section) with 0.113 (Eq.20),

$$r_e = 0.113L \quad \text{(Eq. 20)}$$

or be set manually in the text files defining our wellbore locations and radius “well_in.bh” and “well_out.bh”. These files are in the form of three consecutive numbers (effective radius, x-Coordinate, y-Coordinate, z-Coordinate) and implemented in the main simulation input file.

Additionally, as we are investigating thermal properties, we determine the heat production by multiplying mass flux ($kg.s^{-1}$) by the specific enthalpy ($J.s^{-1}$) (Meyers 2002). The removed heat at the production well is specified by simply building the sum of the produced heat for each phase, which is possible with the “PorousFlowSumQunatity” Kernel.

4.4.4 Relative permeability curves

Relative permeability is a function of the effective saturation of each phase. The respective effective saturation can be found by applying Equation (21) (Wilkins, Green, and Ennis-King 2021; 2020; Slaughter et al. 2021)

$$S_{eff}^{\beta}(S^{\beta}) = \frac{S^{\beta} - S_{res}^{\beta}}{1 - \sum_{\beta'} S_{res}^{\beta'}} \quad \text{(Eq. 21)}$$

where

$$S_{eff}^{\beta} \ldots effective\ saturation\ for\ phase\ \beta$$

$$S^{\beta} \ldots saturation\ of\ phase\ \beta$$

$$S_{res}^{\beta} \ldots residual\ saturation\ for\ phase\ \beta$$

Then the relative permeability of the phase is given by Corey (1954)

$$k_r = S_{eff}^{n} \quad \text{(Eq. 22)}$$

Effective saturation is taken from Equation (21) and n is a user defined exponent which was set to n = 2 resulting in the relative permeability curve being straighter than with the original exponent used by Corey (n=4). This results in higher relative permeability values at the same saturation levels (Zhou, Al-Otaibi, and Kokal 2019).

Permeabilities are implemented into the model via a constant permeability and are entered manually as a tensor. Two intrinsic permeabilities are being investigated, the first one is a high case k = $1*10^{-14}$ m^2 which is equal to 10 mD (millidarcy) and the second one being k = $1*10^{-15}$ m^2 (1 mD). These values are derived from laboratory measurements which initially showed less permeability. However, as permeability determination is quite uncertain and laboratory measurements tend to underestimate permeabilities at natural scale (Parisio and Vilarrasa 2022), these values are deemed feasible in the basaltic crust and the prospect reservoir IDDP-2.

4.4.5 Thermal Expansion & Thermal Conductivity

Thermal expansion is accounted for by the following formula

$$A = (\alpha_B - \phi)\alpha_T + \phi\alpha_f \quad \text{(Eq. 23)}$$

The expansion is computed once during the initial stage of the simulation and is kept constant for the rest of the simulation. Drained volumetric thermal expansion coefficient α_T and the fluid thermal volumetric expansion coefficient are set to $2 * 10^{-4}\ and\ 5 * 10^{-6}$ respectively. The drained volumetric thermal expansion coefficient accounts for the expansion of the

drained porous rock where either no fluid is in place or the fluid is free to move in and out of the rock (Slaughter et al. 2021; Wilkins, Green, and Ennis-King 2021).

The Biot modulus α_B is defined via a different Kernel and computed according to the following equation

$$\frac{1}{M} = \frac{\phi}{K_f} + \frac{(1-\alpha_\beta)(\alpha_\beta - \phi)}{K} \quad \text{(Eq. 24)}$$

The fluid bulk modulus K_f is fixed to the default value $2 * 10^9$ and K is the drained bulk modulus. In our case, instead of the drained bulk modulus, we implemented its reciprocal, which is called solid bulk compliance.

Another rock property that is calculated is the internal energy of the solid rock grains. For this the density of the rock grains is multiplied by the specific heat capacity of the rock. The internal energy is then used by different Kernels such as the energy density where the internal energy is multiplied by the term (1-porosity).

For our model the values are as follows:

Table 6. Rock properties entered into the MOOSE input file

$Rock\ grain\ density$	$2500\ {}^{kg}/_{m^3}$
$Specific\ heat\ capacity\ of\ the\ rock\ grains$	$1200\ {}^{J}/_{kg.K}$

4.5 Solver

In the executioner block information on the solver will be entered. In the case of MOOSE, the solver that is used is provided by a PETSc package. The combination of a PETSc based solver and an individually designed time stepper is possible due to multi-level app coupling within MOOSE as the data transfer between the apps occurs for each time step.

In our case a transient executioner is used as it allows for simulation to do one non-linear solve per time step. For the solver to move through time the time stepper was chosen to be of the kind “iterative”. The iterative time stepper allows for adjusting the time step size based on the difficulty to find the solution. The time step size is adjusted in case the solve does not reach convergence which is why the following parameters have to be defined in the executioner: initial timestep size, maximum number of non-linear iterations, maximum number of linear iterations, cutback factor, applied whenever the solve does not converge, growth factor, solve type (where an implicit-Euler scheme is used as the default), maximum and minimum time step definitions. The last two are used to adjust the time stepper intervals and depends on whether the optimal iteration window is met or not. As mentioned, when the maximum iterations are exceeded the cutback factor is applied to reduce the time step and stop the simulation from running poorly and vice versa. In addition to the number of iterations, the time stepper puts a limit on the size of the time steps by user defined upper and lower boundaries (“dtmax” and “dtmin”) (Lindsay et al. 2022; Slaughter et al. 2021).

In order to simulate long term storage and effects, the simulation is set to end after 20 years.

Table 7. MOOSE executioner block input data specified in the input files with the extension (.i)*

$\boldsymbol{End\ Time}$	$631152000\ seconds\ (20\ years)$
$\boldsymbol{Max.Non-Linear\ Iterations}$	100
$\boldsymbol{Maximum\ Time-Step}$	$31557600\ seconds\ (1\ year)$
$\boldsymbol{Minimum\ Time-Step}$	$100\ seconds$
$\boldsymbol{Initial\ Time-Step}$	$86400\ seconds$
$\boldsymbol{Growth\ Factor}$	2
$\boldsymbol{Cutback\ Factor}$	0.5

4.6 Simulation Sequence

After the MOOSE input file has been set up correctly and the mesh is created successfully, the simulations follow a sequence of steps:

1. Run pressure equilibration simulation without any injection.
2. Determine mass flow rates of water for the different injection temperatures with a fixed CO_2 mass flow rate of 6 kg/s.
3. Run a case with only water injection using the equilibration file as initial pressure input.
4. Run the same case as in 3., this time with CO_2 injection and also using the equilibration file as initial pressure input.
5. Repeat steps 3&4 for all case variations by changing the parameters: permeability, injection temperature, well spacing.
6. Use Jupyter Notebook (or similar programs) to read and analyze CSV data from the simulations and ParaView to view the simulation output files.

4.7 Pressure Equilibration

Pressure equilibration simulations are based on the reservoir mesh created (Figure 27), and according to the boundary conditions that were discussed in chapter 4.4.2. This means that the initial equilibration input file was set up so that permeability was varied for each of the two cases, porosity was entered at 0.15, initial reservoir pressure at the bottom of the reservoir at 34 MPa, pressure at the top of the reservoir was set to 31 MPa, as well as initial temperatures are all fixed in the model.

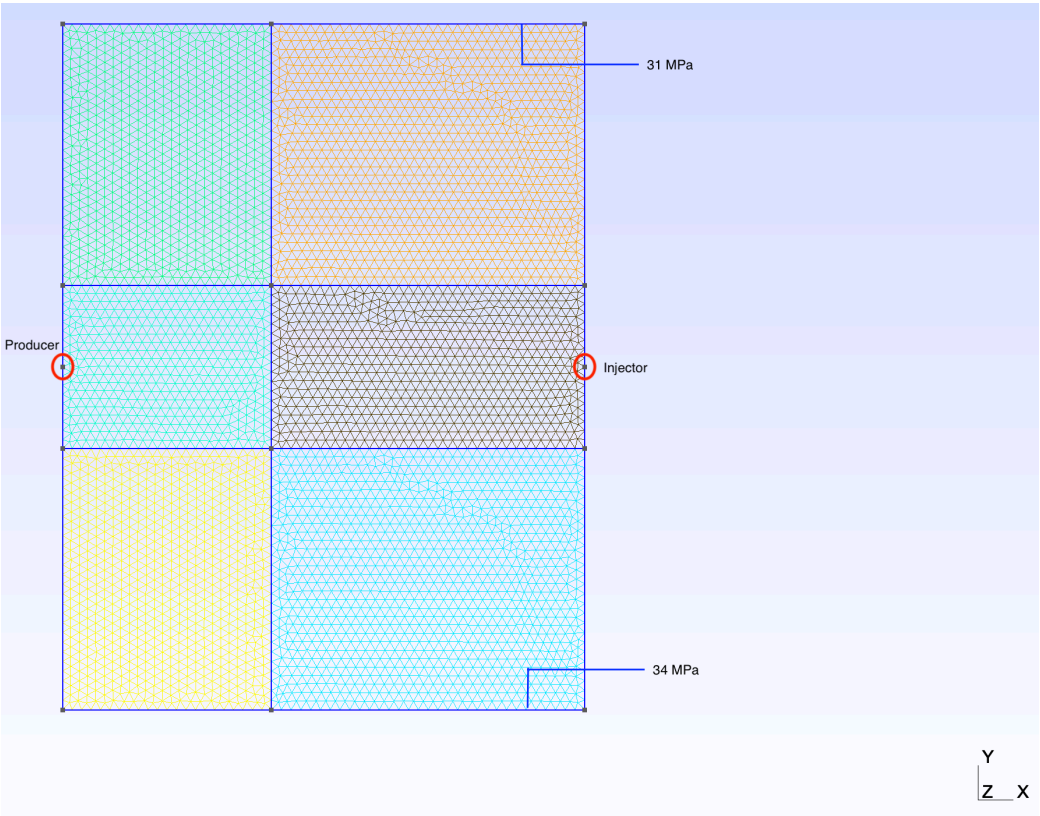

Figure 27. The mesh for the 800-meter well spacing, with the fixed Top and Bottom pressure boundaries

By setting the injection mass flux to zero and not producing from the reservoir, MOOSE can simulate pressure equalization within the reservoir. This makes it possible to determine a feasible hydrostatic pressure profile to ultimately determine an accurate pressure value at the position of the injector. It is important to repeat the pressure equilibration simulation any time the permeability or the reservoir dimensions are changed. To make sure that steady state is reached within the reservoir and to avoid the simulation stopping before equilibrium is reached two measures can be taken. It is possible to either implement a steady state detection command into the input file or to set the simulation time to approximately 200 years or longer. For this experiment both methods were executed and resulted in the same output,

however through steady state detection the simulation stopped early which saved processing power and time.

The results of the two equilibration simulations were used as the initial pressure conditions for the main simulations. Issues arose when the main simulations were performed without running an equilibration case beforehand. The resulting reservoir pressure was far off from any feasible profile and ended up falsifying the results.

The following two figures (28, 29) show the results of the equilibration simulations for the 800-m and 400-meter-wide reservoir.

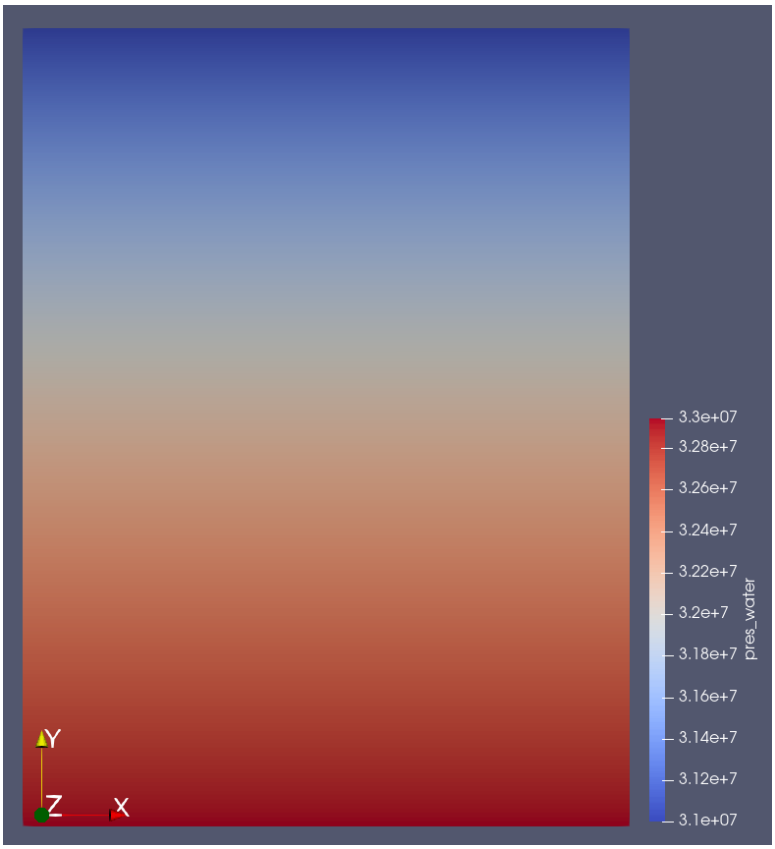

Figure 28. Hydrostatic pressure profile of the 800m wide reservoir after equilibration

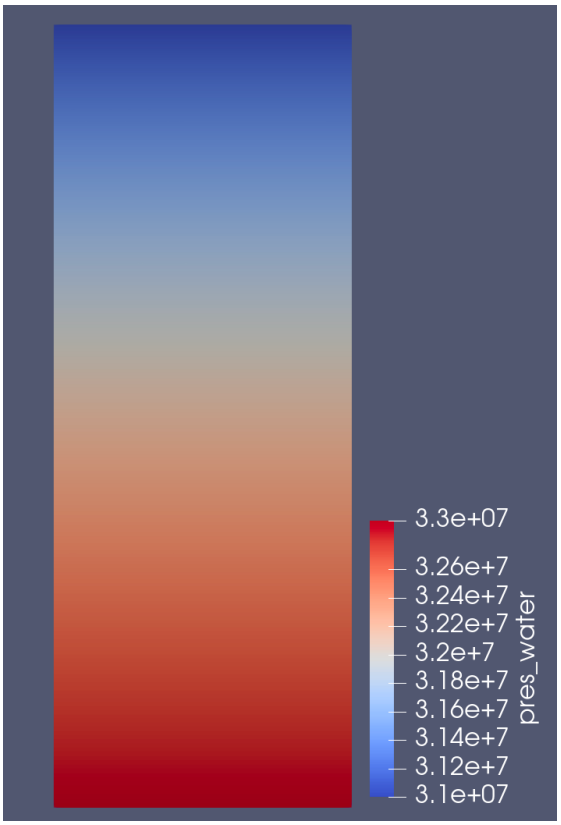

Figure 29. Hydrostatic pressure profile of the 400m wide reservoir after equilibration

Figure 30 shows the reservoir pressure profiles for both domain sizes and the curves coincide after equilibration is performed.

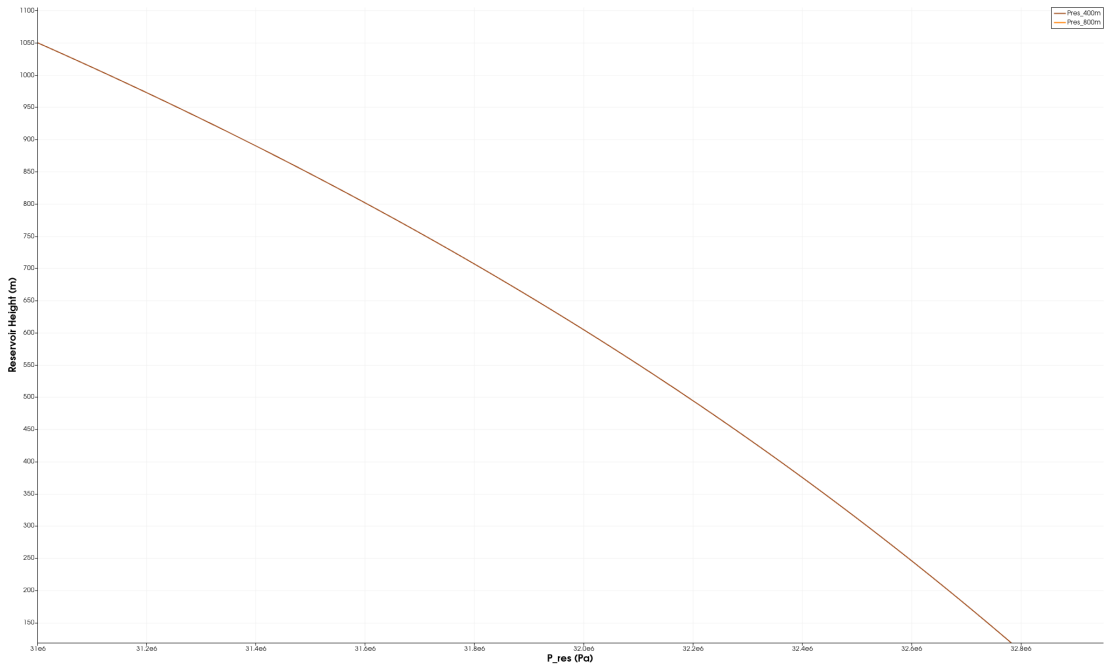

Figure 30. Hydrostatic reservoir pressure curves from top of the reservoir (1050 m) to bottom of the reservoir

4.7.1 Mass Flow Rate Calculations

In order to produce comparable results between the different cases, a mass flow rate of 6 kg/s is fixed for injecting CO_2. The density of CO_2 is determined through an online density calculator from PeaceSoftware (https://www.peacesoftware.de/einigewerte/co2_e.html , accessed April 2023) (Wischnewski, 2007) where the respective downhole temperature and pressure is entered. By entering a rather large downhole pressure of 42 MPa it is ensured that the overpressure is enough to overcome the reservoir pressure at the injector and, thus, making inflow into the formation possible. Due to the difference in density of water and CO_2 it is necessary to convert the mass flow of CO_2 to the mass flow rate of water to maintain the same injection pressure when simulating only water injection. Initially, simulations were based on a fixed volumetric flow rate, however this resulted in non-converging simulation which lead to the decision of fixing the mass flow and thus reaching convergence.

The following steps are performed in order to determined mass flow rates. First, the density and fixed mass flow are entered into Equation (25)

$$Q = \frac{\dot{m}_{CO2}[kg/s]}{\rho_{CO2}\,[kg/m^3]} \qquad \text{(Eq. 25)}$$

with the resulting volumetric flow rate and the density of water at the specified conditions, the mass flow rate of water at the given conditions can be determined as

$$\dot{m}_{H2O} = Q\,[m^3/s] * \rho_{H2O}[kg/m^3] \qquad \text{(Eq. 26)}$$

As the density of water is also dependent on the downhole temperature and pressure, Wolfram Alpha's online density calculator widget (https://www.wolframalpha.com/widgets/view.jsp?id=1de7d2b90d554be9f0db1c338e80197d, accessed April 2023) is used to determine the density value which is consequently entered into Equation (26).

This procedure has to be repeated for each change in temperature or pressure because density is a function of the encountered downhole conditions $\rho(p, T)$.

Table 8. Results of the mass flow calculations for the two different injection temperature scenarios

$T_{inj}\,[°C]$	$P_{inj}\,[MPa]$	$\rho_{CO2}\,[\frac{kg}{m^3}]$	$\dot{m}_{CO2}\,[\frac{kg}{s}]$	$Q[\frac{m^3}{s}]$	$\rho_{H20}\,[\frac{kg}{m^3}]$	$\dot{m}_{H2O}\,[\frac{kg}{s}]$
380	42	325,08	6	0,01845699	602,7	11
60	42	899,54	6	0,00667008	1001	6,7

4.8 Input Data: Water vs. CO_2 - Injection

The following tables (Tables 9-11) provide an overview of the parameters used in the simulations and should highlight the differences between the cases.

Table 9. Parameters remaining constant for every case.

Reservoir Thickness h	1050 m
T_{res}	500°C
Porosity ϕ	0.15
TVD (Top of Reservoir)	3000 m
P_{wf} **Production Well**	30 MPa

Table 10: Summary of the input parameters for the MOOSE input file with 800-m well spacing between production and injection well

	Case 1	**Case 2**	**Case 3**	**Case 4**
Identifiers	$CO2\_1A$ $H2O\_1B$	$CO2\_2A$ $H2O\_2B$	$CO2\_5A$ $H2O\_5B$	$CO2\_6A$ $H2O\_6B$
Permeability k	$1 * 10^{-15}\ m^2$	$1 * 10^{-14}\ m^2$	$1 * 10^{-15}\ m^2$	$1 * 10^{-14}\ m^2$
T_{inj}	380°C		60°C	
$\dot{m}_{CO2}$	$6\ \frac{kg}{s}$			
$\dot{m}_{H2O}$	$11\ \frac{kg}{s}$		$6{,}7\ \frac{kg}{s}$	
Well spacing	800m			

Table 11. Summary of the input parameters for the MOOSE input file with 400-m well spacing between production and injection well

	Case 5	**Case 6**	**Case 7**	**Case 8**
Identifier	$CO2\_7A$ $H2O\_7B$	$CO2\_8A$ $H2O\_8B$	$CO2\_9A$ $H2O\_9B$	$CO2\_10A$ $H2O\_10B$

Permeability k	$1 * 10^{-15}\ m^2$	$1 * 10^{-14}\ m^2$	$1 * 10^{-15}\ m^2$	$1 * 10^{-14}\ m^2$
T_{inj}	$60°C$		$380°C$	
$\dot{m}_{CO2}$	$6\ \frac{kg}{s}$			
$\dot{m}_{H2O}$	$6{,}7\ \frac{kg}{s}$		$11\ \frac{kg}{s}$	
Well spacing	$400m$			

4.9 CO_2 Plume and Gravity Number

Identification of the CO_2 plume movement is done by analyzing the gravity number for each case. The gravity number is used to quantify the effects of buoyancy forces on the plume movement. It is given as the ratio of buoyancy forces over viscous forces and determines if the CO_2 sinks at the investigated point. In plain language, the gravity number is connected to the pressure gradient and buoyancy.

According to Darcy's law the flow in a reservoir can either be pressure or buoyancy dominated. In the case of a small pressure gradient the gravity number can then be used to identify if the density difference between the phases is large enough in order for the CO_2 to sink. Sinking of CO_2 can be expected when N is above 1 and vice versa, in case the gravity number is below 1, then viscous forces are dominating and consequently reducing the vertical mobility. The influence of gravity on the plume movement increases with the increasing size of the plume, due to the increase of the characteristic lengths (Vilarrasa et al. 2010).

The gravity number can be expressed as

$$N = \frac{2\pi d r_{ch} k \Delta\rho g \rho_{ch}}{\mu_{CO2} Q_m} \qquad \text{(Eq. 27)}$$

Where d is a characteristic length, which represents the thickness of the plume. As the plume occupies approximately two thirds of the reservoir thickness, the value was selected to be 700 m. Other variables are the permeability in m^2 the density difference between the water and CO_2 in kg/m^3, gravitational acceleration in m/s^2 as well as the viscosity in Pa·s and mass flow rate in kg/s. The characteristic length r_{ch} is entered as the horizontal distance from the

investigated point to the injection point and the characteristic density represents the density of the supercritical CO_2 at the investigated point.

Chapter 5

Results

5.1 Sinking CO_2 & Temperature Profiles

5.1.1 Far Well Spacing – 800 m

As seen in Figure 31 during injection of CO_2 with an injection temperature of 380°C into the low permeability reservoir leads to a symmetrical plume shape. Plume migration seems to be rather horizontal with initially no visible sinking effects. In the majority of the reservoir the temperatures are already well above the critical point of water leading to the density of CO_2 being higher than that of the supercritical water (Figure 32).

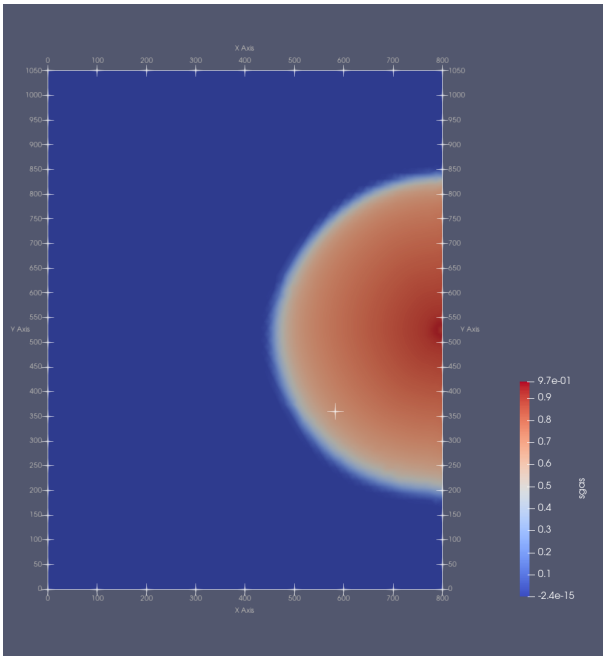

*Figure 31. CO_2 Plume at **$k = 1*10^{-15}$** m^2 and T_{inj} = 380°C after 20 years*

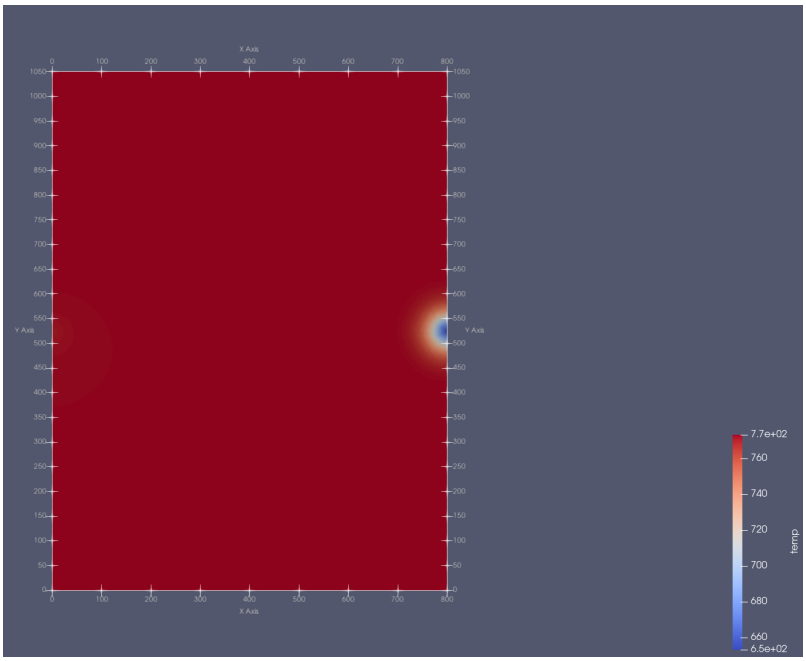

Figure 32. Temperature profile of CO_2 (in Kelvin) of the reservoir at ***k = 1*10^{-15}*** *m^2 and T_{inj} = 380°C after 20 years*

Comparing the same injection temperature and same well spacing to the higher permeability case leads to a clearly visible sinking of the CO_2 (Figure 33). By calculating the gravity number for both permeability cases, the results showed that the lower permeability case does not show sinking which that is further confirmed by the gravity number N = 0,67 (N<1), meaning that viscous forces dominate, and the plume moves horizontally rather than vertically.

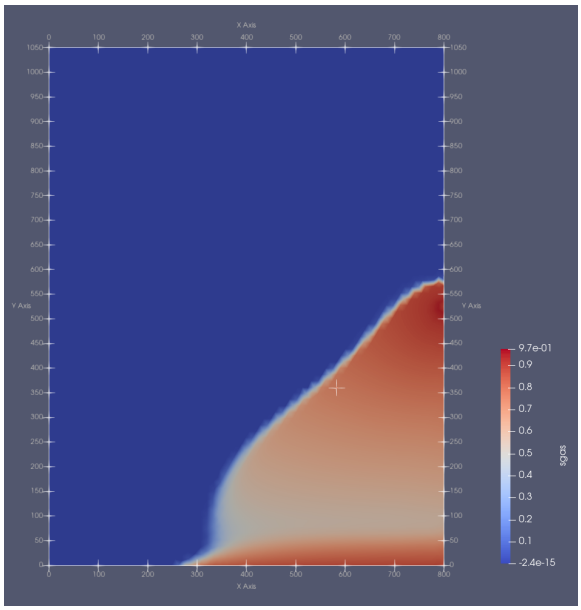

Figure 33. CO_2 Plume at ***k = 1*10^{-14}*** *m^2 and T_{inj} = 380°C after 20 years*

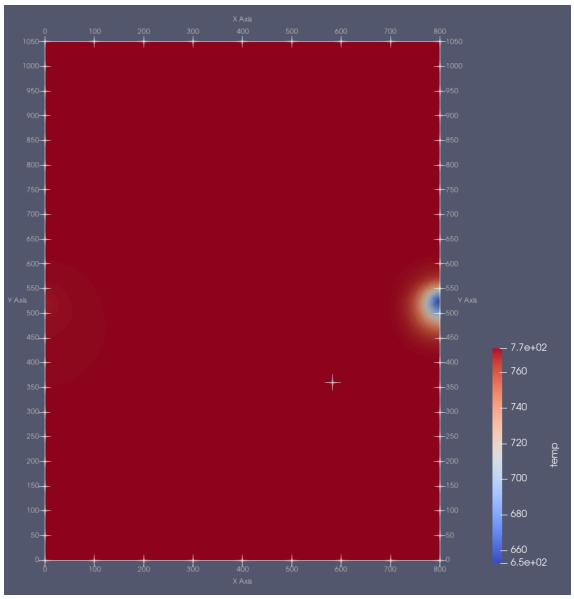

Figure 34. Temperature profile of CO_2 (in Kelvin) of the reservoir at ***k = 1*10^{-14}*** *m^2 and T_{inj} = 380°C after 20 years*

In the case of k = $1*10^{-14}$ m^2 (Figure 33) the gravity number was computed to be N = 6,81 (N>>1) confirming that the flow is gravity dominated as a result of the large permeability causing the CO_2 to sink.

When comparing the temperature profiles for the case when only water is injected, the temperature profile shows a larger radius of the cooled region in the low permeability

reservoir (Figure 35). Nonetheless, no thermal breakthrough to the producer is observed. The reason for the increased radius of the cooled region when compared to the CO_2 injection, is that the heat capacity of water is higher.

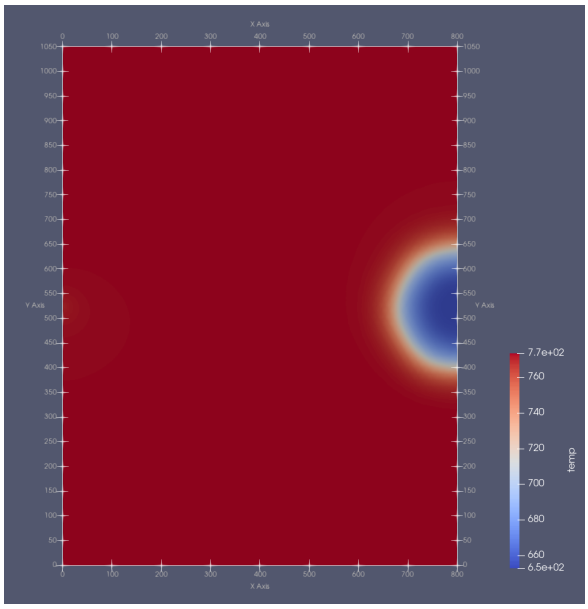

Figure 35. Temperature profile for H_2O injection at T_{inj} = 380°C and low permeability ***k = 1*10^{-15} m^2*** *after 20 years*

In Figure 36, the increased permeability in combination with the lower viscosity of water causes the injected water to cool the area below the injector. This results in a different shape of the temperature profile compared to the CO_2 case at the same conditions.

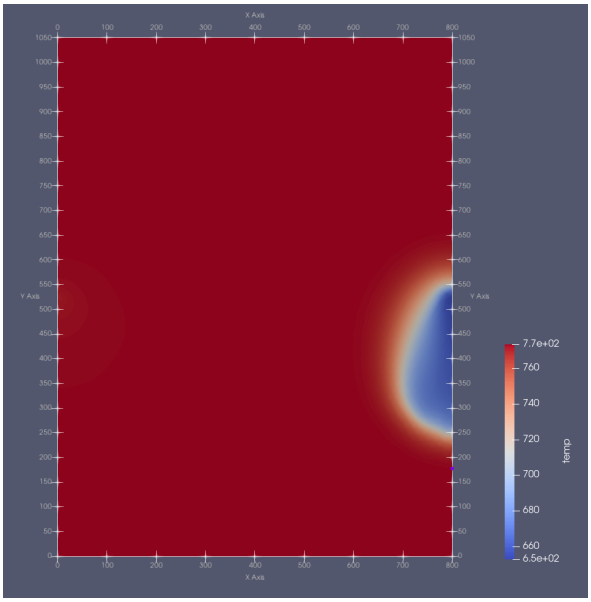

Figure 36. Temperature profile for H_2O injection at T_{inj} = 380°C and high permeability ***k = 1*10^{-14} m^2*** *after 20 years*

The following gas saturation and temperature profiles show the results for CO_2 injection at 60°C downhole. While the shape of the plume is largely unchanged and is similar to the high temperature injection from Figures 31-36, the temperature profiles only seem to change in magnitude and resemble previous shapes in both low- (Figure 37, 38) and high permeability cases (Figure 39, 40). However, a difference in the temperature profile for CO_2 in high permeability can be observed, showing a slightly larger cooled region extending below the injector (Figure 40).

The temperature difference in the near wellbore region changes as the difference in temperature between the reservoir (500°C) and the injected CO_2 is now greater than when injecting with 380°C. However, the size of the cooled region stays in the magnitude of the cooled area from the higher injection temperature case. As expected, gravity numbers for the lower temperature case are the same as the ones computed for the hotter injection, since the reference point is chosen to be in an area where thermal equilibrium is already reached. At this point, the densities of the phases have adjusted to the reservoir temperature and pressure.

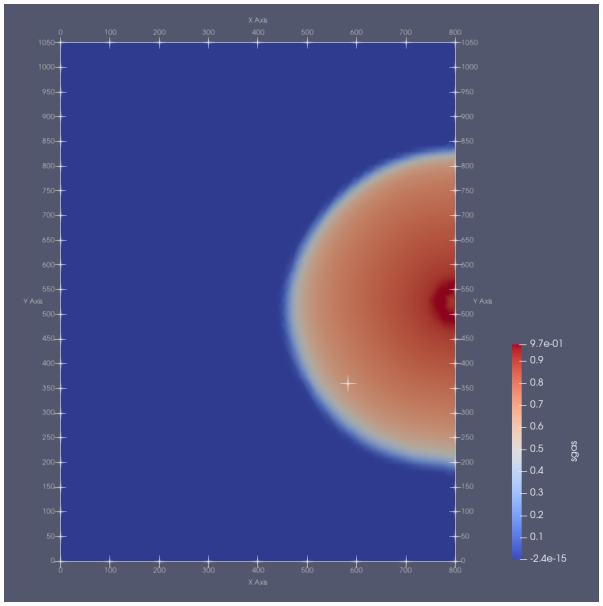

Figure 37. CO_2 Plume at $\mathbf{k = 1*10^{-15}\ m^2}$ and T_{inj} = 60°C after 20 years

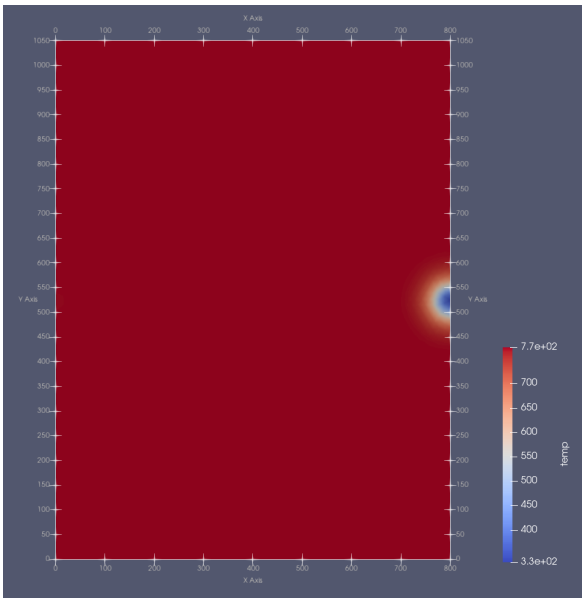

Figure 38. Temperature profile of CO_2 (in Kelvin) of the reservoir at $\mathbf{k = 1*10^{-15}\ m^2}$ *and* T_{inj} *= 60°C after 20 years*

Figures 39 and 40 show the gas saturation profile and temperature distribution for the high permeability case, when injecting CO_2.

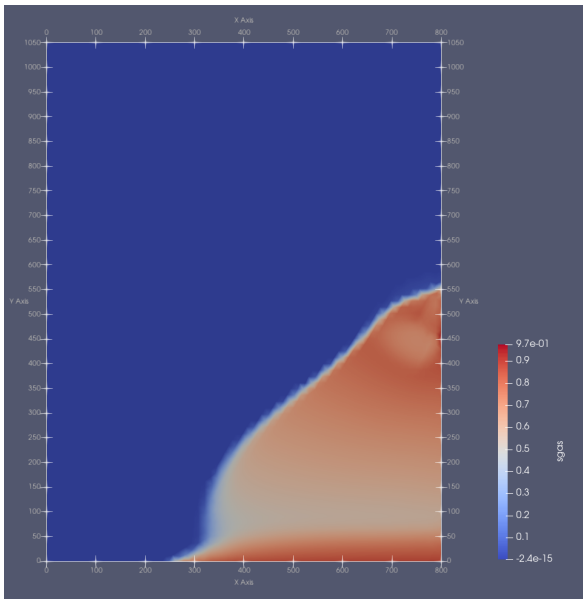

Figure 39. CO_2 Plume at ***k = 1*10^{-14} m^2*** *and T_{inj} = 60°C after 20 years*

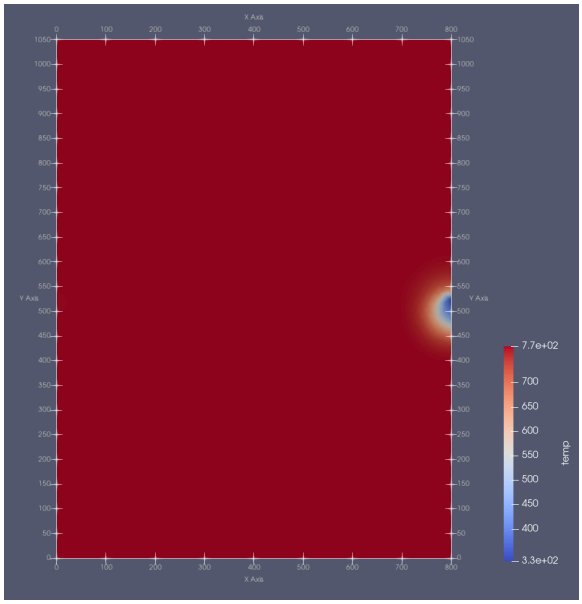

Figure 40. Temperature profile of CO_2 (in Kelvin) of the reservoir at ***k = 1*10^{-14} m^2*** *and T_{inj} = 60°C after 20 years*

For the water injection at 60°C the temperature profiles show the same trends as when injecting CO_2. The area of the cooled region increases when injecting water. Figures 41 and 42 show the water injection temperature contour plots.

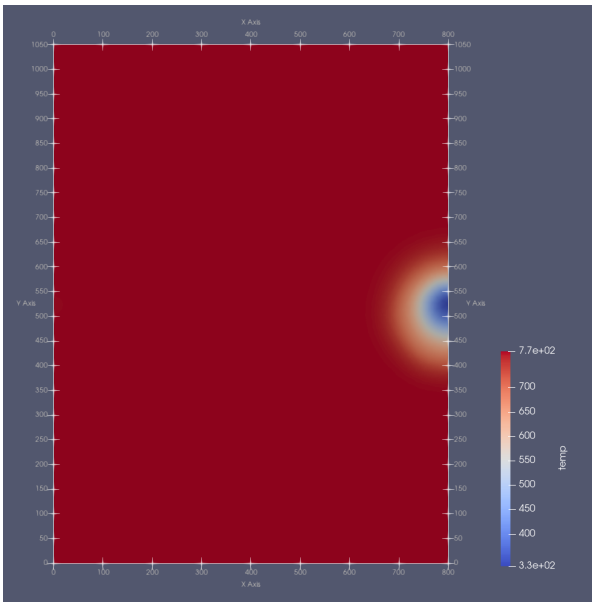

Figure 41. Temperature profile for H_2O injection at T_{inj} = 60°C and low permeability ***k = 1*10^{-15} m^2*** *after 20 years*

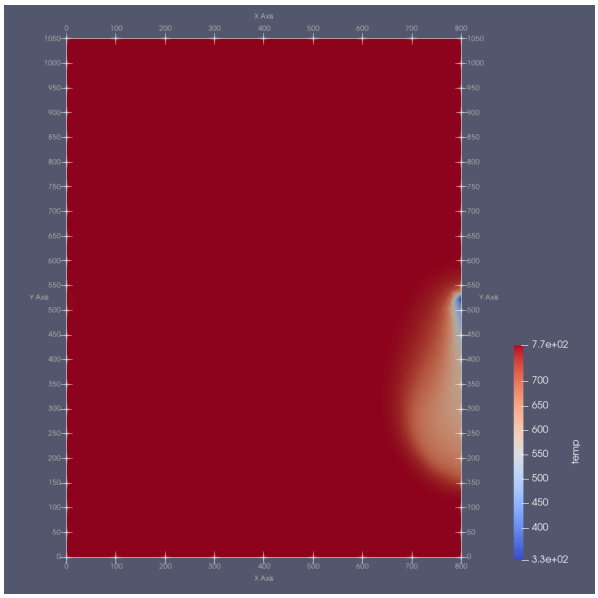

Figure 42. Temperature profile for H_2O injection at T_{inj} = 60°C and high permeability ***k = 1*10^{-14} m^2*** *after 20 years*

As illustrated in Figure 43, the permeability does not influence the CO_2 in terms of the distance after thermal equilibrium is reached. However, Figure 44, shows that in the water case, thermal equilibrium is reached earlier, when permeability is high. Additionally, water generally reaches thermal equilibrium at a later stage than CO_2 due to its higher heat capacity.

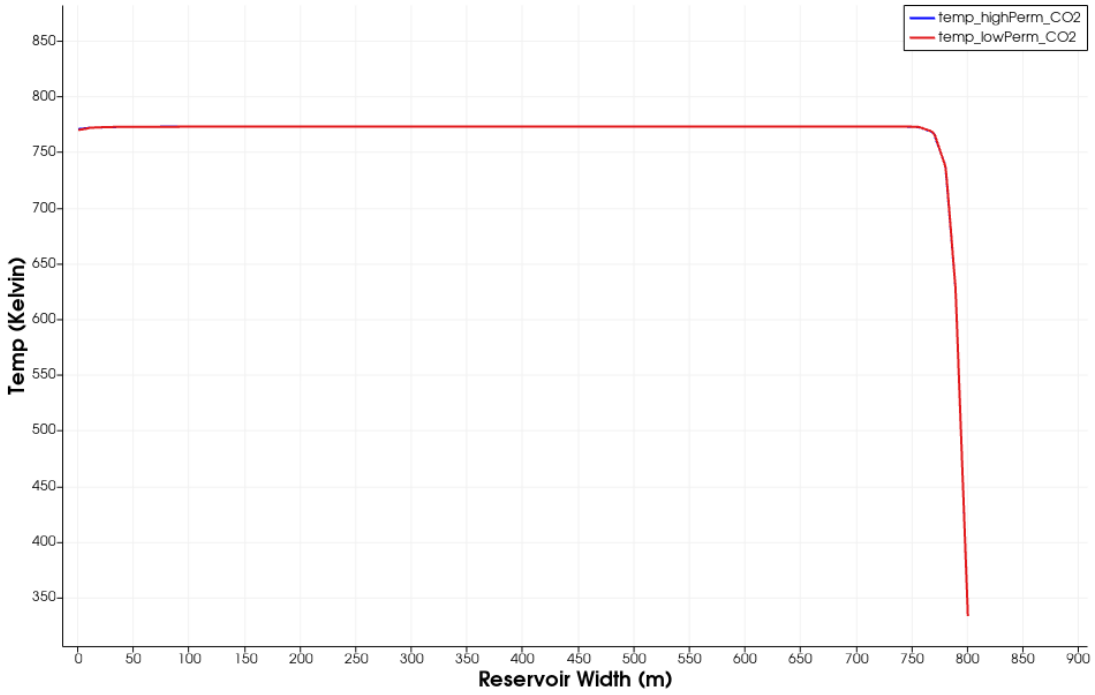

Figure 43. Temperature in high vs. low permeability reservoirs for CO_2 injection

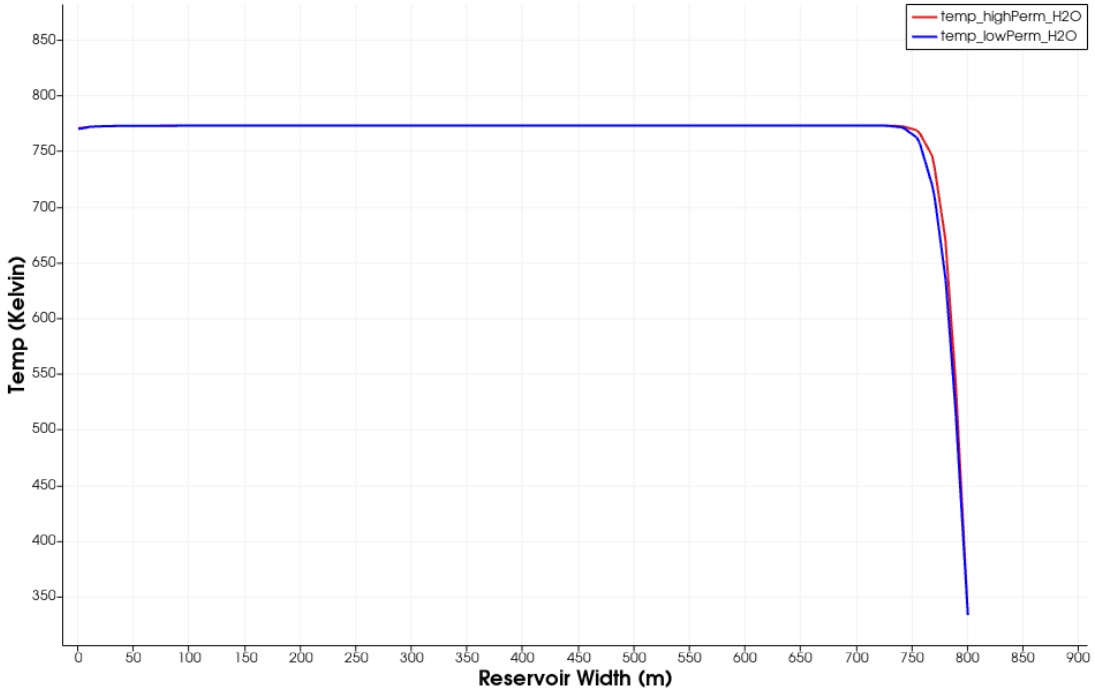

Figure 44. Temperature in high vs. low permeability reservoirs for H_2O injection

5.1.2 Close Well Spacing – 400m

Analysis of the saturation profiles when the injection and production well are 400 meters apart indicate a CO_2 breakthrough. The breakthrough can be observed in all the simulations in which the wells were moved closer together, independent of temperature and permeability variations.

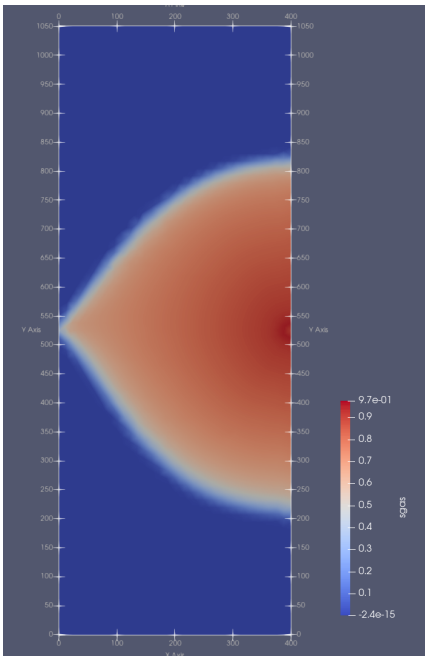

*Figure 45. CO_2 Plume at **k = 1*10^{-15}** m^2 and T_{inj} = 380°C after 20 years*

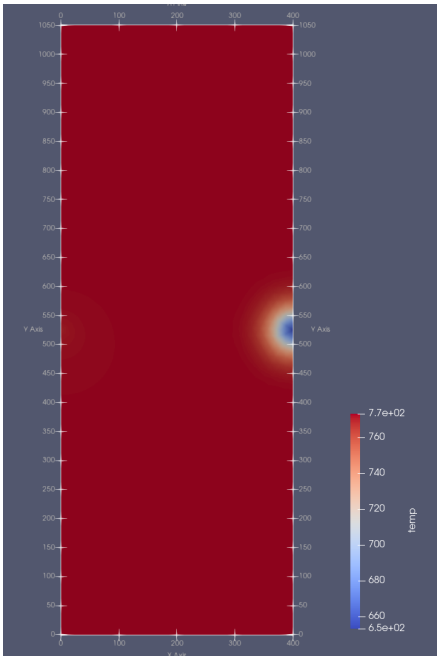

*Figure 46. Temperature profile of CO_2 (in Kelvin) of the reservoir at **k = 1*10^{-15} m^2** and T_{inj} = 380°C after 20 years*

As discussed earlier, gravity number calculations resulted in the same values for the two permeability cases: N = 0,70 for k = $1*10^{-15}$ m^2 (Figure 45) and N = 6,78 for k = $1*10^{-14}$ m^2 (Figure 47).

Due to the closer well spacing, the CO_2 is dragged towards the production well. This effect can be seen for both permeability cases. In the high permeability case around the production well, the viscous forces are in competition with gravity, and although the flow in the high permeability reservoir is mostly gravity dominated, viscous forces were able to move some of the sinking CO_2 upwards.

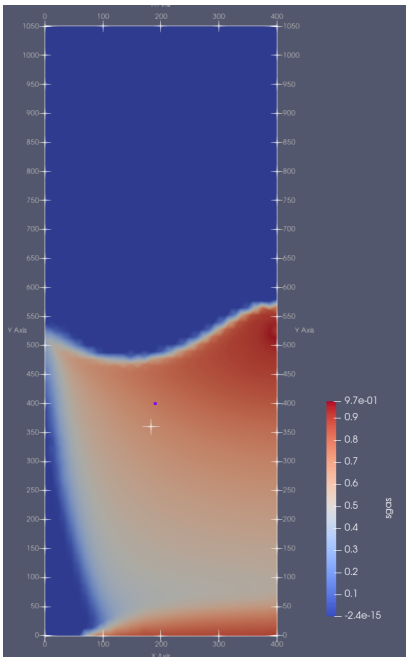

*Figure 47. CO_2 Plume at **k = 1*10^{-14}** m^2 and T_{inj} = 380°C after 20 years*

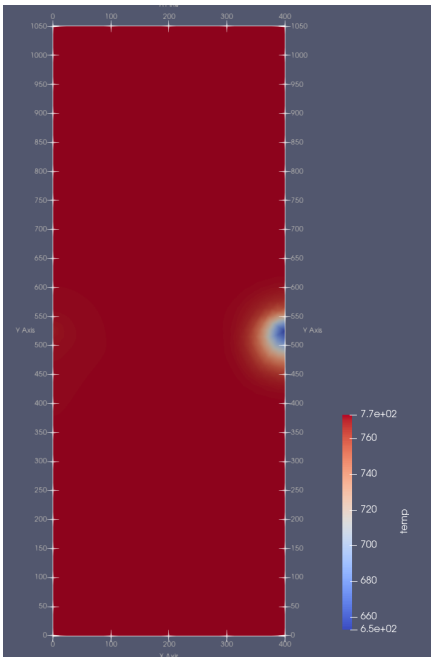

Figure 48. Temperature profile of CO_2 (in Kelvin) of the reservoir at ***k = 1*10^{-14} m^2*** *and T_{inj} = 380°C after 20 years*

Although the shorter well spacing results in CO_2 breakthrough, there is no temperature breakthrough in neither the CO_2 injection nor the H_2O injection case for both permeabilities.

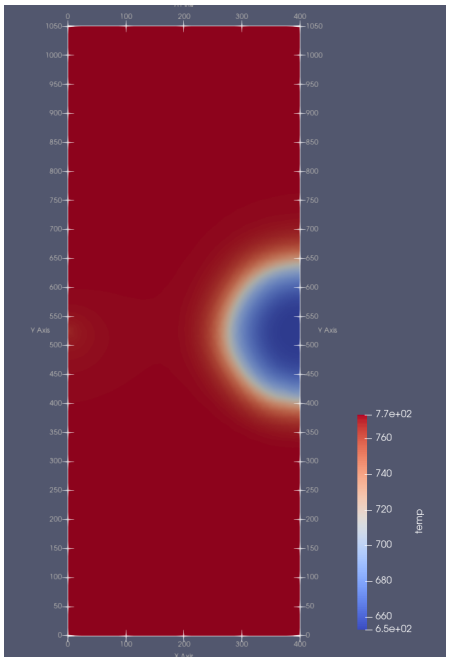

Figure 49. Temperature profile for H_2O injection at T_{inj} = 380°C and low permeability ***k = 1*10^{-15} m^2*** *after 20 years*

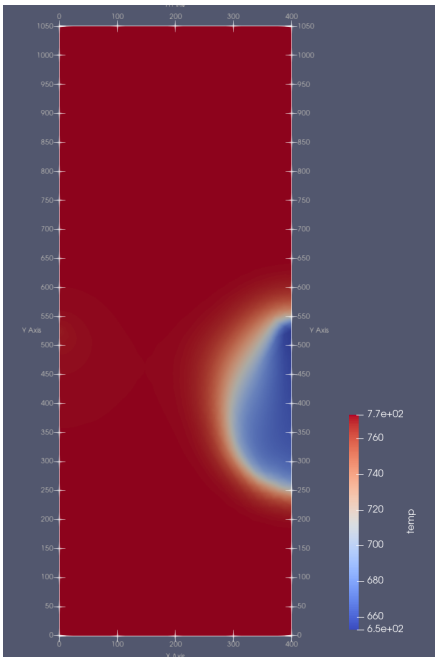

Figure 50. Temperature profile for H_2O injection at T_{inj} = 380°C and high permeability ***k = 1*10^{-14} m^2*** *after 20 years*

When simulating with at lower temperature the gas saturation profile also indicates CO_2 breakthrough due to the shorter well spacing (Figure 51, 52). In the lower temperature case (60°C injection) no temperature breakthrough is observed for neither CO_2 nor H_2O, and the water injection displays a larger area of the cooled region, as seen in all the previous cases.

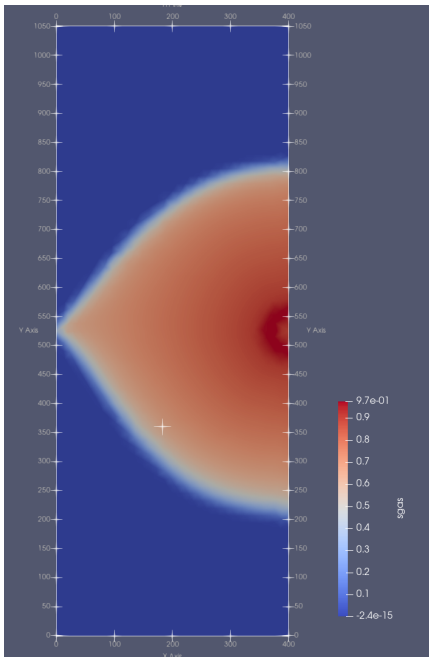

*Figure 51. CO_2 Plume at **k = 1*10^{-15}** m^2 and T_{inj} = 60°C after 20 years*

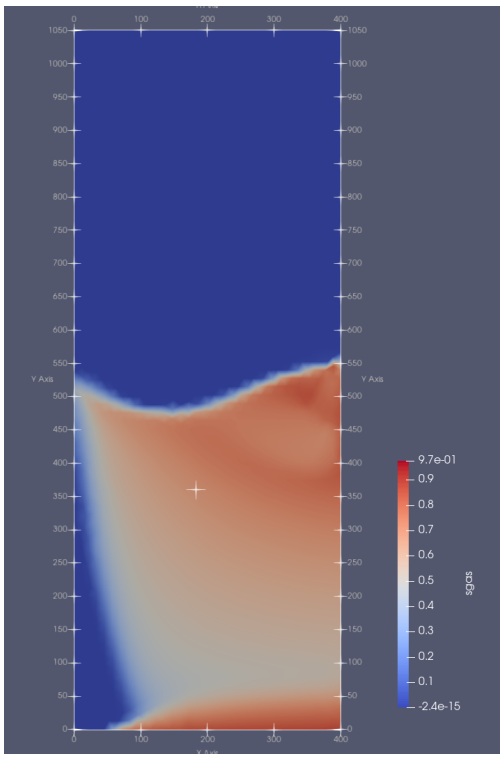

*Figure 52. CO_2 Plume at **k = 1*10^{-14}** m^2 and T_{inj} = 60°C after 20 years*

Figures 53 and 54, also show the temperature plots comparing high- and low-permeability reservoirs in the case of CO_2 injection and water injection. As stated in the 800-m case the CO_2 (Figure 53) shows the same thermal behavior for both permeabilities, whereas water reaches thermal equilibrium earlier when injected into highly permeable rocks (Figure 54).

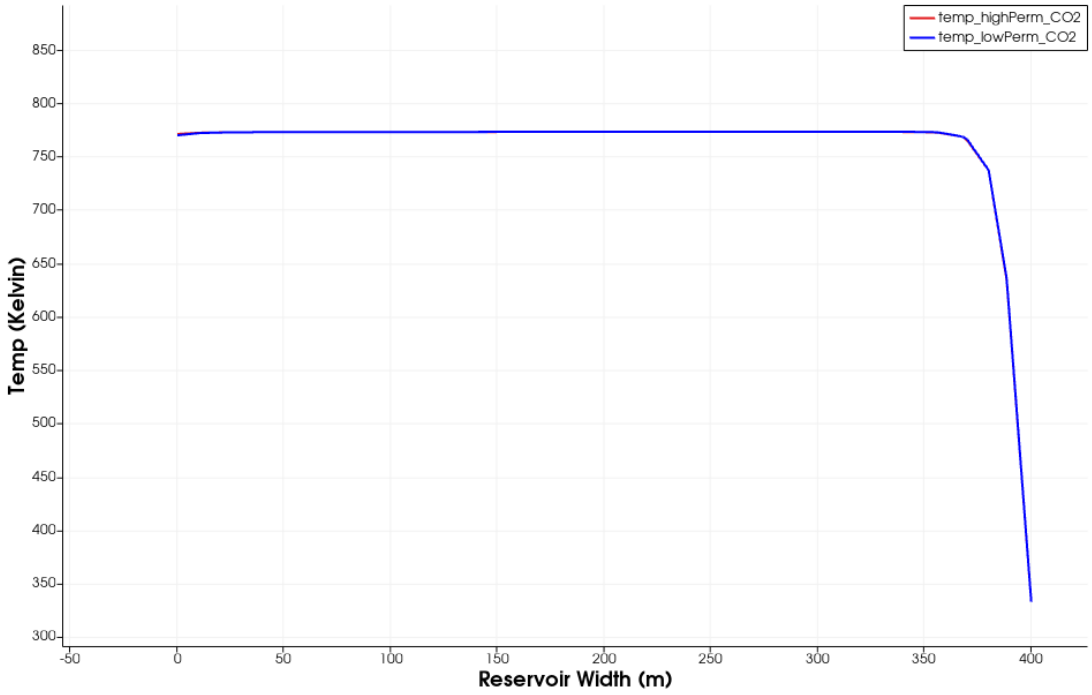

Figure 53. Temperature in high vs. low permeability reservoirs for CO_2 injection

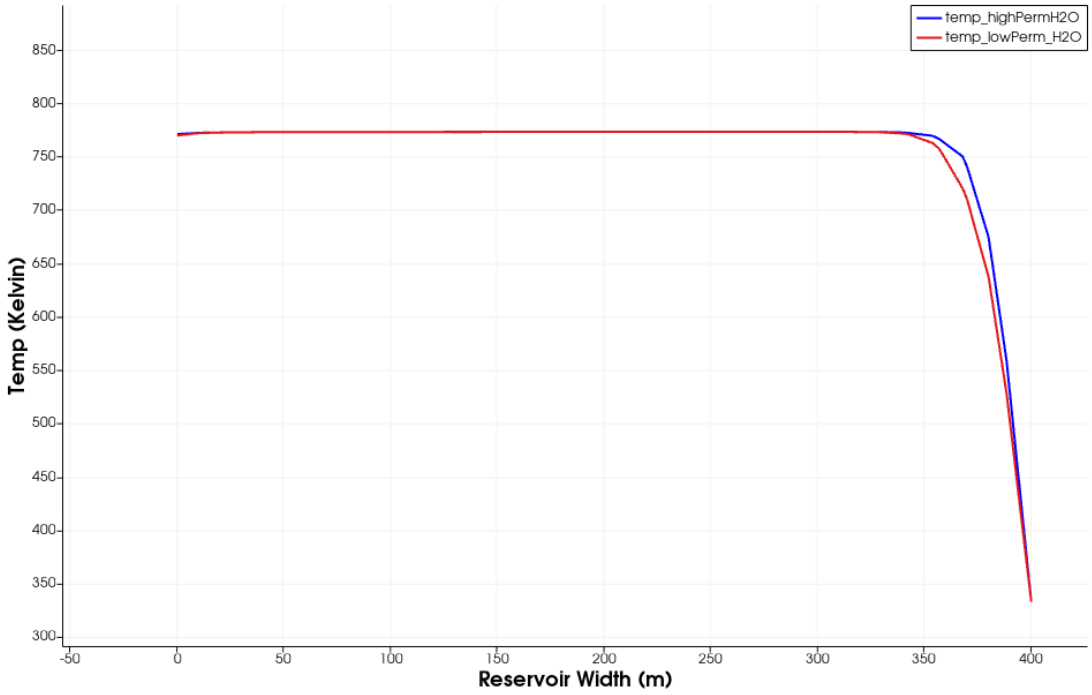

Figure 54. Temperature in high vs. low permeability reservoirs for H_2O injection

The effect of different distances of reaching thermal equilibrium, in the case of water injection, is also observed in the temperature profiles (Figure 55, 56)

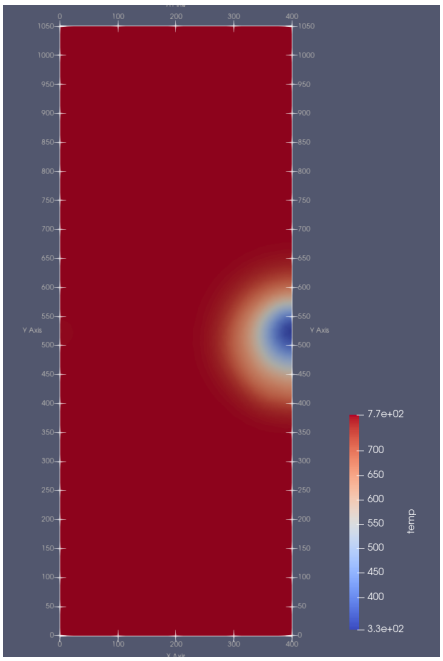

Figure 55. Temperature profile for H_2O injection at T_{inj} = 60°C and low permeability ***k = 1*10^{-15} m^2*** *after 20 years*

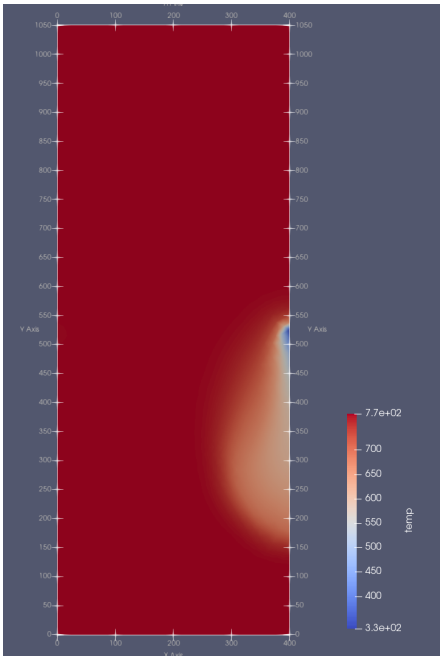

Figure 56. Temperature profile for H_2O injection at T_{inj} = 60°C and low permeability ***k = 1*10^{-14} m^2*** *after 20 years*

5.2 Injected CO_2

As defined previously, all the simulations use a mass flow rate of 6 kg/s for CO_2 injection. This means that the total mass injected is the same for all simulations and equates to 3.78 Mt of CO_2 after 20 years of injection (Figure 57).

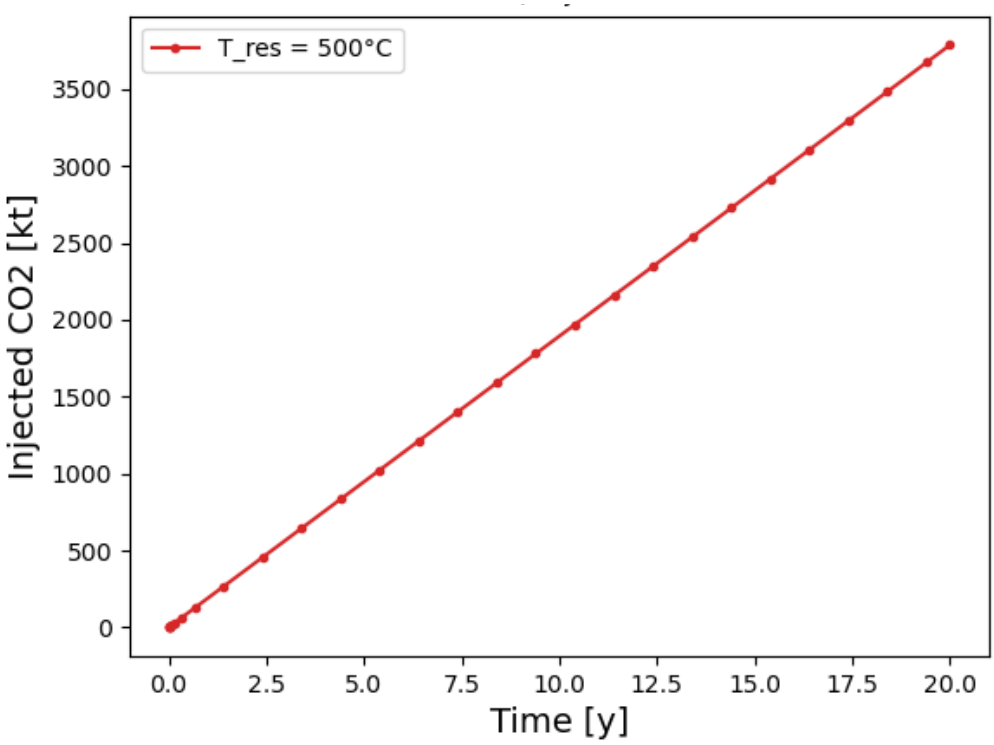

Figure 57. Total mass of CO_2 injected into the reservoir after 20 years at an injection mass flow rate of 6 kg/s.

5.3 Produced Energy

The cumulative energy that is produced over 20 years of injection is plotted for both, the CO_2 injection case and the H_2O injection case. By using Jupyter notebook, a python-based notebook, the CSV files from the simulations can be read. Firstly, the energy produced at each timestep is computed by multiplying the mass of CO_2 or H_2O that is extracted at the specified timestep (given in kilograms) with the specific enthalpy of the respective phase (given in kJ/kg). The cumulative energy is added up over the 20-year timespan and can then be plotted for each case.

5.3.1 Far Well Spacing – 800 meters

The following figures show the cumulative energy produced for the all cases with a reservoir width of 800 meters.

Figure 58 shows the cumulative energy produced for the low permeability case when injection temperature is 380°C. In all cases the cumulative energy produced is higher when injecting water only in contrast to CO_2.

When the injected phase is CO_2, then the high permeability case is the best option for maximum energy output. The different injection temperatures do not play a role when the injected phase is CO_2, neither for high nor for low permeability cases.

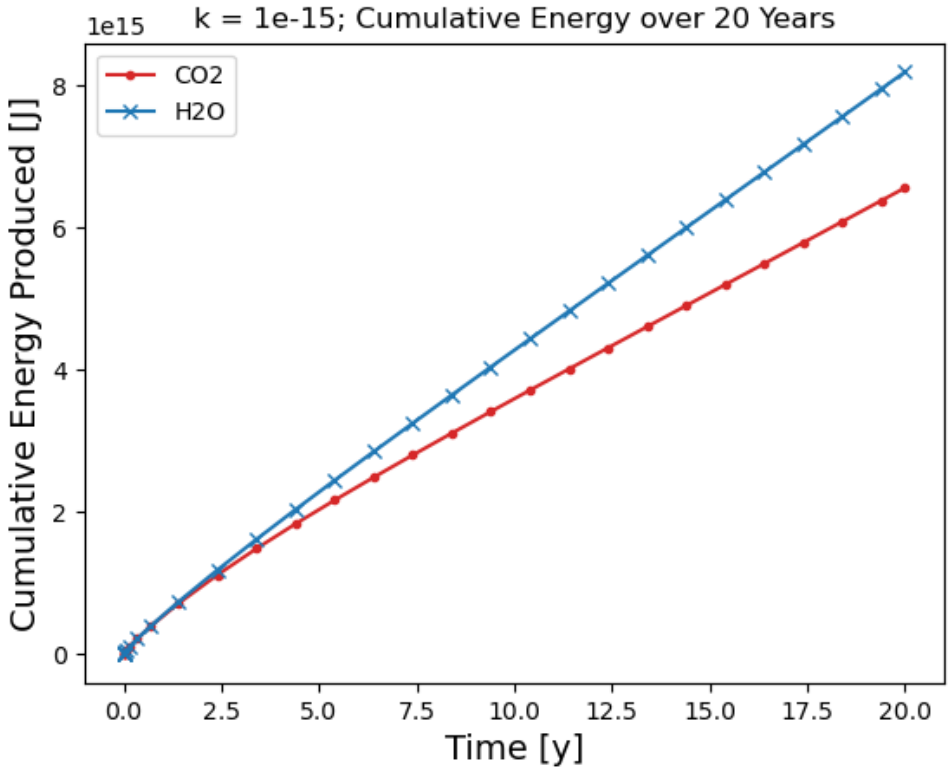

Figure 58. Cumulative energy production with injection temperature at 380°C and low permeability (800m apart)

However, it must be noted that, as seen in Figure 59 when only water is injected, the produced energy decreases significantly at an injection temperature of 60°C. The fact that injection at super high temperatures, close to 380°C, are not feasible, makes a case for injecting CO_2 at lower temperatures, as the difference in produced energy between water and CO_2 then becomes very small. By taking the added benefit of storing the CO_2 into account, it can be of advantage to go for the CO_2 injection.

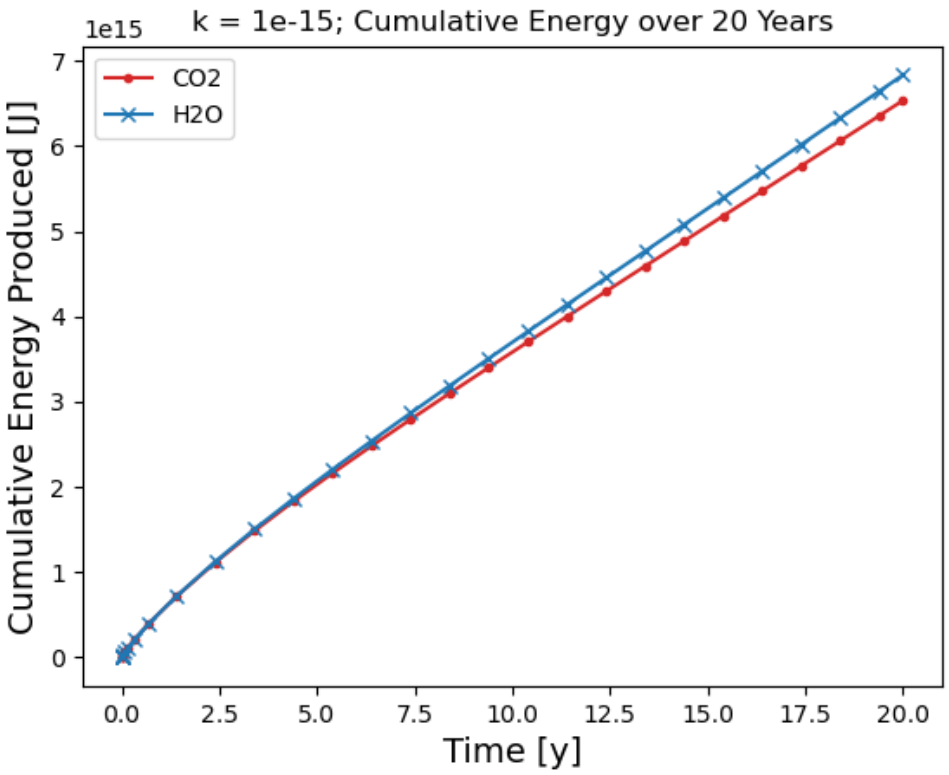

Figure 59. Cumulative energy production with injection temperature at 60°C and low permeability (800m apart)

Table 12 shows the resulting energy produced for the cases and also indicates that when injecting at 60°C the option with the most total value looks to be the CO_2 injection. Figures 60 and 61 compare the cumulatively produced energy for the different injection temperatures.

*Table 12. Resulting cumulative energy produced for a well spacing of **800 meters***

Case 1	Cumulative Energy Produced [J]	$k = 1*10^{-15}$ m^2		Injection Temperature: 380°C
		CO_2 Injection Case	H_2O Injection Case	
		$6{,}56*10^{15}$	$8{,}19*10^{15}$	
Case 2	Cumulative Energy Produced [J]	$k = 1*10^{-14}$ m^2		
		$4{,}72*10^{16}$	$4{,}98*10^{16}$	
Case 5	Cumulative Energy Produced [J]	$k = 1*10^{-15}$ m^2		Injection Temperature: 60°C
		$6{,}53*10^{15}$	$6{,}83*10^{15}$	
Case 6	Cumulative Energy Produced [J]	$k = 1*10^{-14}$ m^2		
		$4{,}72*10^{16}$	$4{,}82*10^{16}$	

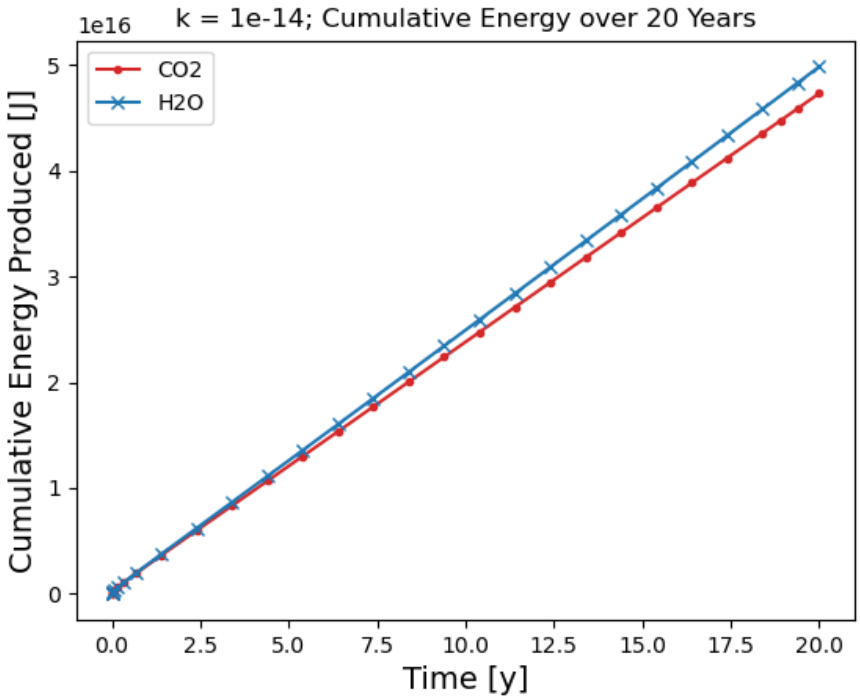

Figure 60. Cumulative energy production with injection temperature at 380°C and high permeability (800m apart)

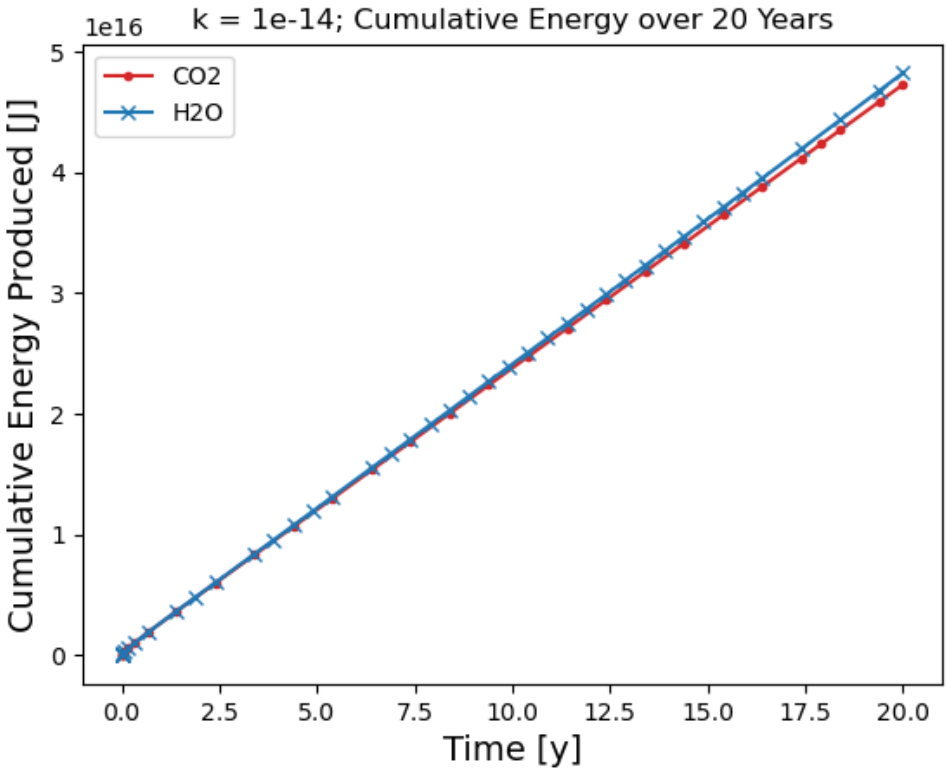

Figure 61. Cumulative energy production with injection temperature at 60°C and high permeability (800m apart)

5.3.2 Close Well Spacing – 400 meters

As already mentioned in the CO_2 plume section for the short well spacing cases, the CO_2 breakthrough can also be observed when looking at the mass of CO_2 produced, as seen in Figures 62. When comparing the amount of years it takes until CO_2 production begins, it is observed that the injection temperature has no influence on when CO_2 starts being produced. The main difference is between the two permeability cases. After examination of the CSV file, the number of years until CO_2 breakthrough was 14,7 years in case of a low permeability reservoir and 12,4 years when permeability is high. Through CO_2 breakthrough, the mass of produced water is reduced which consequently leads to a reduction in produced energy.

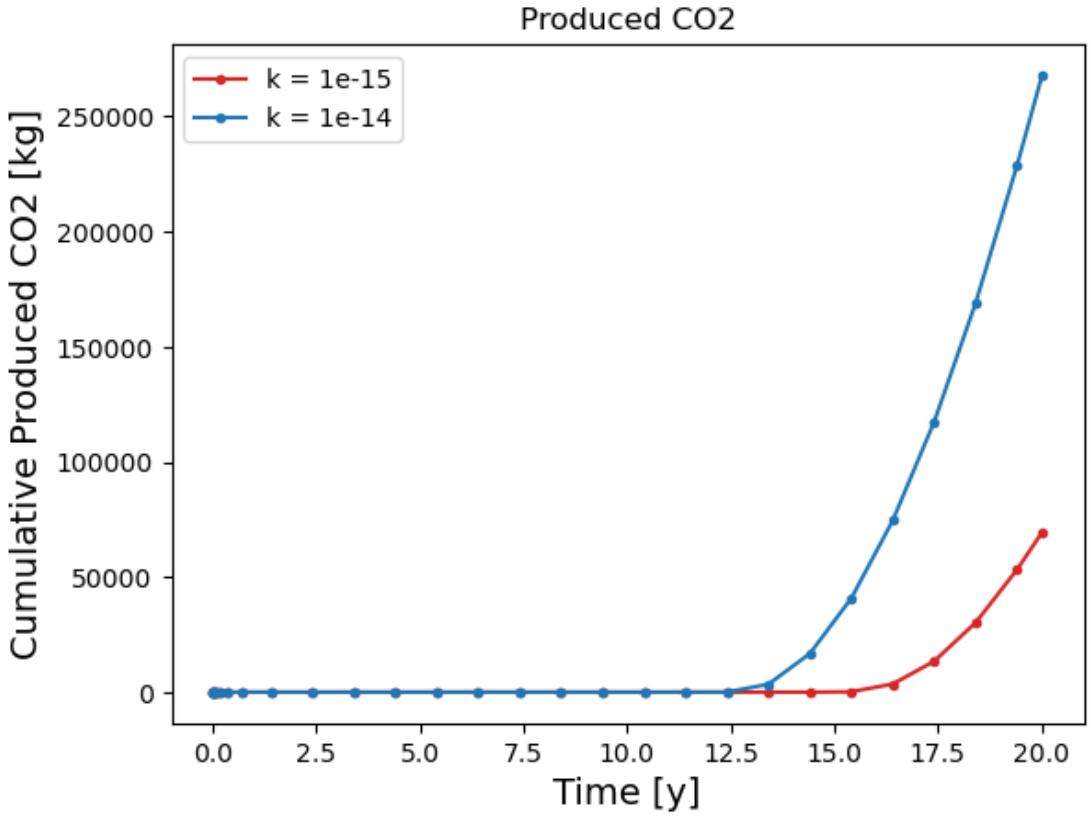

Figure 62. Time after CO_2 starts breaking through and is produced at the production well

Also shown in Figure 62, is the higher permeability and slight dominance of viscous forces causing a larger dragging towards the production well, leading to significantly more mass of CO_2 being extracted.

A comparison of Table 12 and Table 13, indicates that energy production is higher when well spacing is 800 meters (Table 12).

*Table 13. Resulting cumulative energy produced for a well spacing of **400 meters***

Case 9	Cumulative Energy Produced over 20 Years [J]	$k = 1*10^{-15}$ m^2		Injection Temperature: 380°C
		CO_2 Injection Case	H_2O Injection Case	
		$6,45*10^{15}$	$1,087*10^{16}$	
Case 10	Cumulative Energy Produced [J]	$k = 1*10^{-14}$ m^2		
		$3,91*10^{16}$	$4,69*10^{16}$	
Case 7	Cumulative Energy Produced [J]	$k = 1*10^{-15}$ m^2		Injection Temperature: 60°C
		$6,45*10^{15}$	$7,816*10^{15}$	
Case 8	Cumulative Energy Produced [J]	$k = 1*10^{-14}$ m^2		
		$3,91*10^{16}$	$4,34*10^{16}$	

For completeness, Figures 63 – 66 show the charts for the cumulative energy produced in the 400 m well spacing case. The red curve, referring to the energy production via CO_2 injection diverges from the H_2O line at the point of CO_2 breakthrough at the producer.

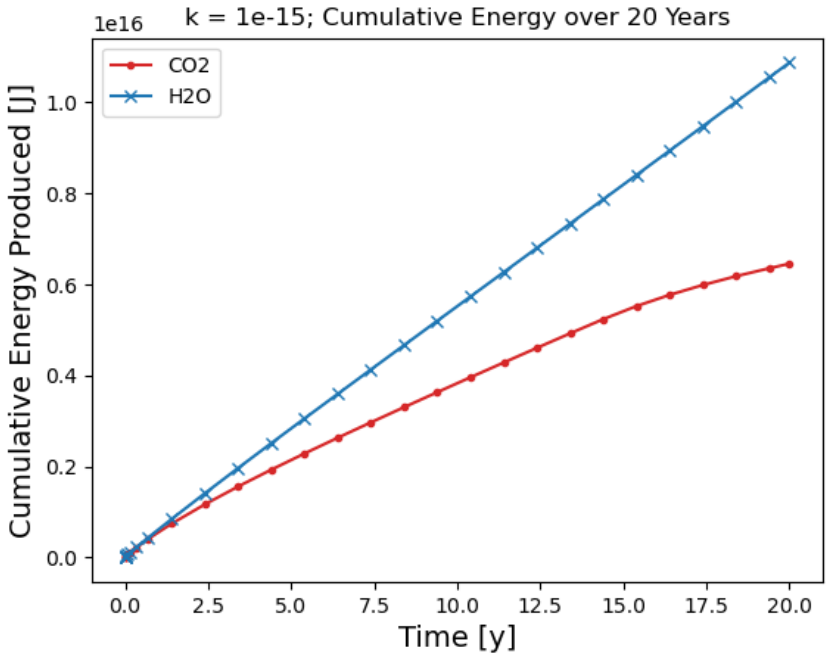

Figure 63. Cumulative energy production with injection temperature at 380°C and low permeability (400m apart)

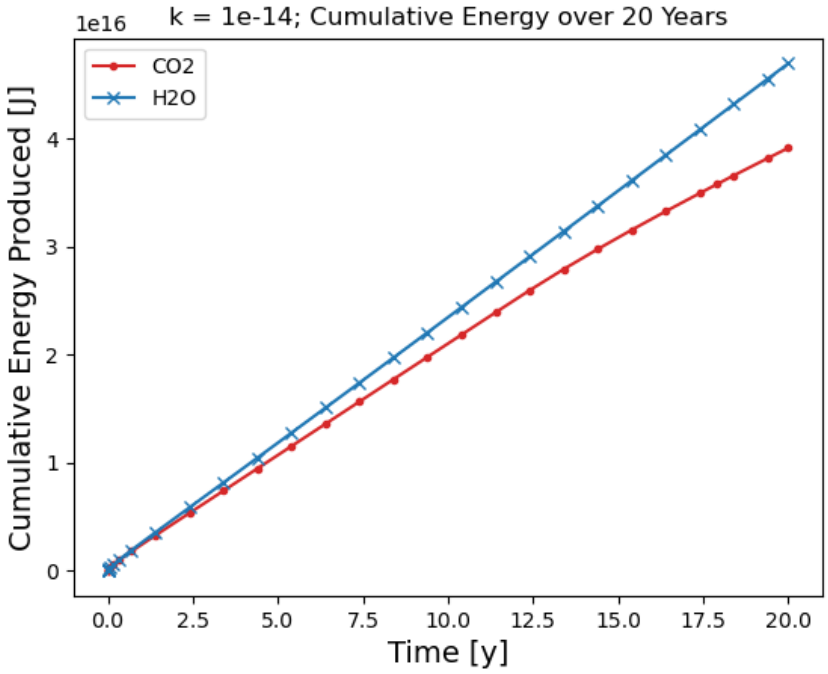

Figure 64. Cumulative energy production with injection temperature at 380°C and high permeability (400m apart)

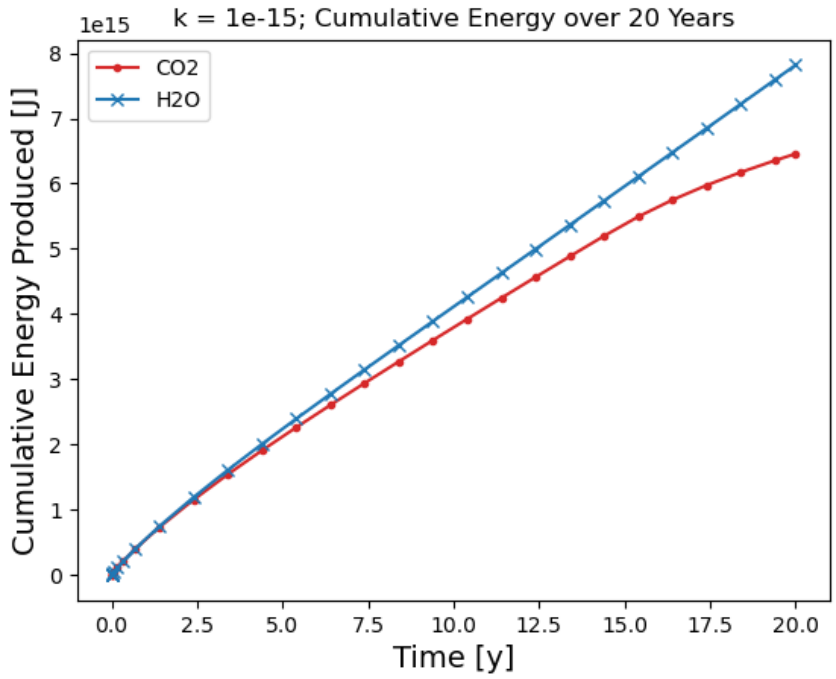

Figure 65. Cumulative energy production with injection temperature at 60°C and low permeability (400m apart)

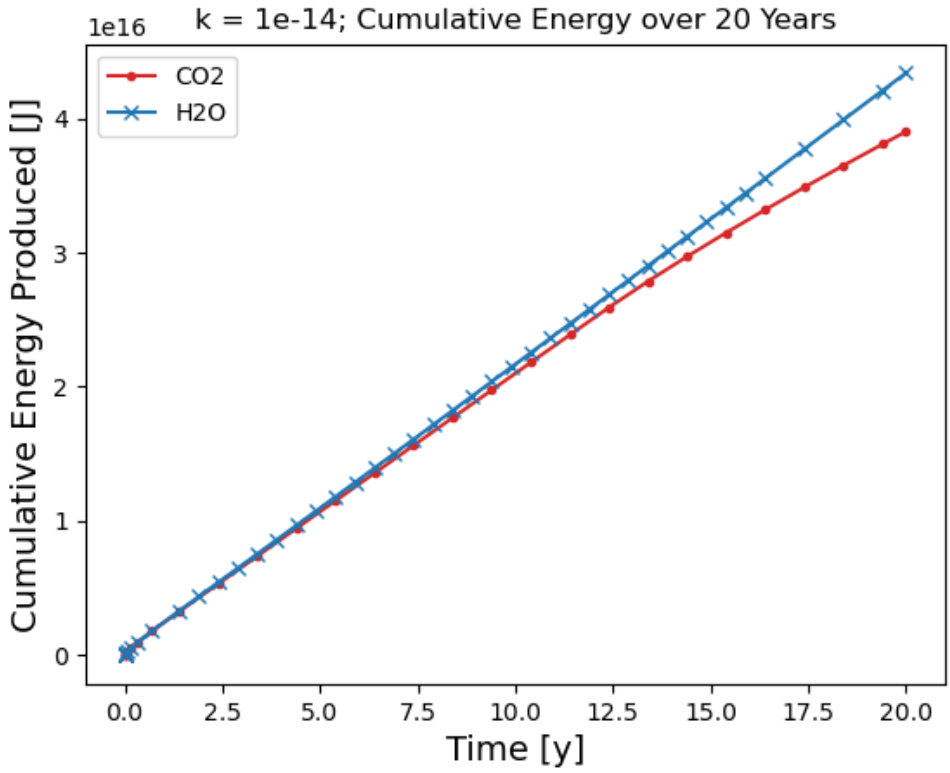

Figure 66. Cumulative energy production with injection temperature at 60°C and high permeability (400m apart)

5.4 Pressure Profiles

The following figures show the pressure profiles during injection at 60°C, with an overlay of isobar lines ranging from 30 MPa to 33 MPa. In the low permeability reservoir, most of the high-pressure area is concentrated around and close to the injection area (Figure 67, 68).

When comparing the path of the isobar lines with high permeability (Figure 69,70), better pressure support occurs due to larger pressures occurring at the bottom of the reservoir caused by the higher permeability.

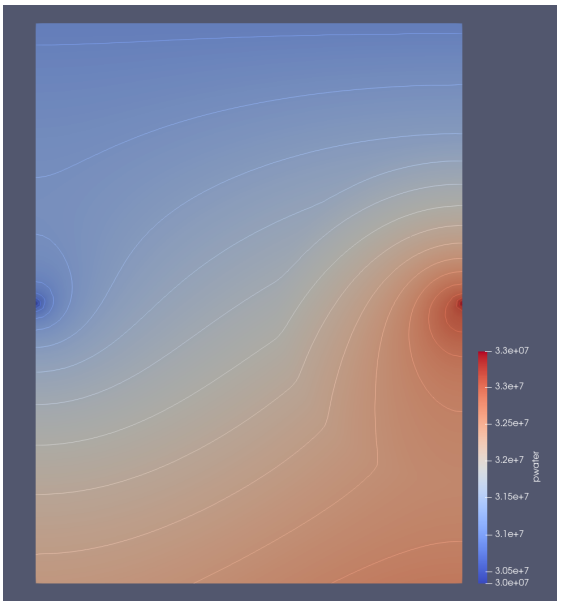

Figure 67. Pressure profile for CO_2 injection at $k = 1*10^{-15}$ m^2 after 20 years

Additionally, Figure 68 illustrates the effect of the higher viscosity of water compared to CO_2, as the pressure gradients around the injector are higher.

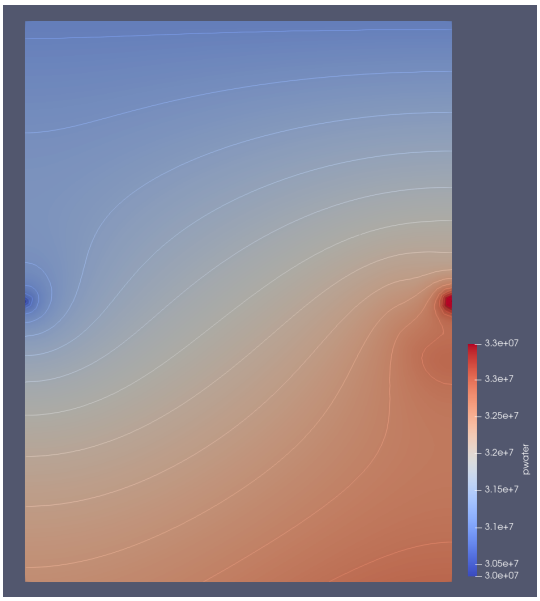

*Figure 68. Pressure profile for H_2O injection at k = 1*10^{-15} m^2 after 20 years*

In the case of high permeability (Figures 69,70), gravity forces dominate, causing a lower pressure buildup around the injector. Water's increased viscosity leads to an increased pressure at the lower righthand area of the reservoir (Figure 70).

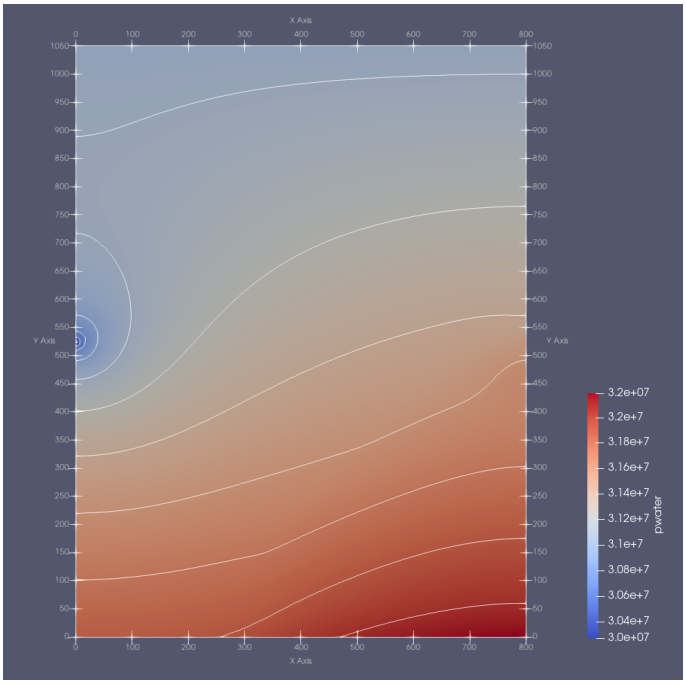

*Figure 69. Pressure profile for CO_2 injection at k = 1*10^{-14} m^2 after 20 years*

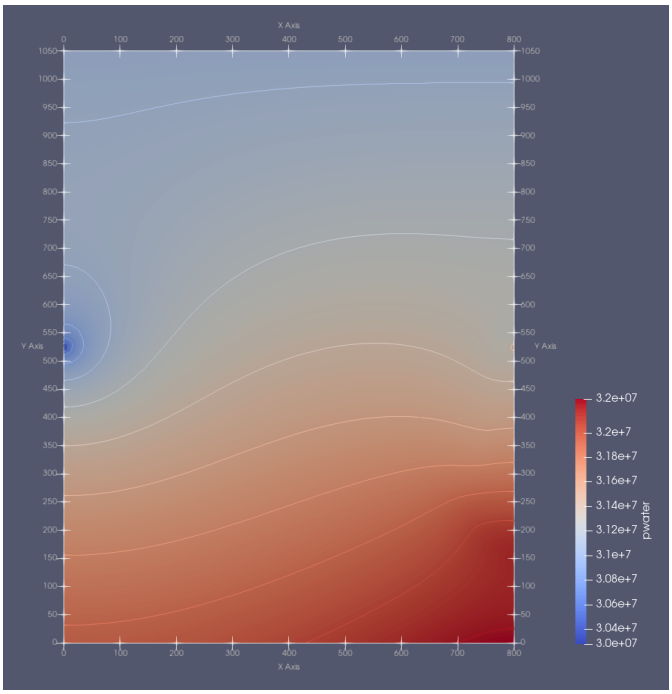

*Figure 70. Pressure profile for H_2O injection at k = 1*10^{-14} m^2 after 20 years*

Chapter 6

Discussion

The simulations that were performed all showed similar gas saturation profiles when comparing the high and the low temperature case. The biggest change in plume size and development was caused by changing the permeability. During injection in high permeability reservoirs, the CO_2 injection resulted in the plume sinking to the bottom of the reservoir resulting in an accumulation of CO_2 below the water phase. This supports the hypothesis that storing CO_2 in supercritical enhanced geothermal systems is possible without the presence of a seal rock. Analysis of the gravity number shows that in reservoirs where permeability is low ($k = 1*10^{-15}$ m^2), viscous forces dominate the flow ($N<1$), hence the plume moves horizontally through the reservoir with little influence of gravity forces. This movement is more complex than in the highly permeable reservoir, however due to the similarity of the plume shape among the 380°C injection temperature and 60°C injection temperature it can be concluded that the effects are mostly governed by permeability as the expected density shift has occurred all along. This domination of viscous forces gives the impression of a symmetrical plume around the injector but with the important aspect that CO_2 is not buoyant meaning that safe storage is deemed possible in both cases. This is possible because due to the high reservoir temperature and pressure, and although the plume might look like it is not influenced by gravity, it is slightly larger in the bottom half of the reservoir indicating a trend in downwards movement.

The two different well spacings helped to identify the distance between wells that leads to CO_2 breakthrough. Simulation results show that CO_2 breakthrough occurs after 12,4 years for the high-permeability case and after 14,7 years for the low-permeability case. Considering that projects with the objective of storing CO_2 underground are expected to be operational for up to and above 50 years, these results are not acceptable from an operational standpoint and

disqualify a well spacing of 400 meters. The time until CO_2 breakthrough was the same for both injection temperature cases.

Selecting a downhole injection temperature of 380°C was done in order to provide a reference case at super high temperature conditions and investigate the impact of injecting at more feasible temperatures like 60°C. From an operational perspective, reaching a downhole injection temperature of 380°C and pressure of 42 MPa is not economically feasible. At those conditions CO_2 has a density of 325 kg/m^3 and almost the same pressure is required at the wellhead as downhole in order to compress it enough so injection can be performed. Compression pumps capable of providing such conditions are, if technology even permits it, economically not attractive due to their high energy consumption and large footprint.

The lack of thermal breakthrough neither in the CO_2 injection nor the H_2O injection cases, regardless of well spacing or permeability variations results in high energy production as the heat extracted is maximized. However, due to the higher heat capacity of water the cases with solely water injection produced a temperature profile with large, cooled areas surrounding the horizontal injection well. This large temperature drop causes a thermal stress reduction which can lead to induced seismicity in deep volcanic areas (Parisio et al. 2019). Due to the unknown presence of faults within our reservoir and thus an activation of such faults, seismic events could be triggered. This increase of seismicity due to wellbore quenching was observed by Parisio et al. (2019) when modelling long-term re-injection of cold water. When compared to CO_2, the increased water viscosity due to the low temperatures cause an increase in total water head (Parisio et al. 2019) and presents a sinking effect of the water, which could also be seen in the high permeability case. The larger cooled region also results in a large rock volume being contracted due to the low temperatures. With the circular shaped of the cooled region, the contracted rock results in a reduction of the vertical stresses, which causes an increase in horizontal stresses in order to satisfy the stress equilibrium. Consequently, the presence of a large fault in the region of the cool rock, will result in a destabilization. Due to this thermo-mechanical effect, the CO_2 injection case is advantageous as the cooled areas is smaller. In addition to that, the CO_2 injection cases are not sensitive to different permeabilities, as they reach thermal equilibrium at the same distance for both permeabilities. This is different in the case of water injection, as in the high permeability case thermal equilibrium with the reservoir is reached earlier. This indicates that in real life, when permeability distribution in the reservoir varies, the resulting CO_2 temperature profile is not affected as much by these changes.

In terms of energy production, all the cases show that the cumulative energy produced over 20 years of injection is higher in the case of water injection as compared to CO_2 injection.

This can be attributed to the increased displacement and sweep in the case of high permeability.

When comparing the domains, the larger reservoir domain shows higher energy production compared to the closer well spacing. The results show that the injected and produced mass is the same for the large and small domain, this is due to mass conservation. The higher production can be explained by the fact that energy production is computed as the product of mass of water extracted and the specific enthalpy. Consequently, if there is CO_2 breakthrough then there is less production of H_2O, hence less produced energy.

Table 12 in the results section, shows the amount of energy produced in Joules. When looking at the numbers, it stands out that the high permeability case produces seven times more energy than the low permeability case. In absolute numbers, over a period of 20 years, the energy produced by a doublet, in the case of CO_2 injection into a highly permeable rock, results in 47,2 Petajoules (PJ) ($4{,}72*10^{16}$ Joules). This is 2,36 PJ of produced thermal energy per year. With the assumption that the well is more efficient than traditional geothermal wells, due to the supercritical conditions present, the electricity produced can be calculated to around 20% of the thermal energy, which is 0,472 PJ. However, when comparing this number to 1123 PJ, which is the total Austrian energy consumption in 2021 (“Energy Balances” 2022), this result seems quite low, and can be attributed to the fixed injection rates and fixed bottomhole pressure at the producer.

The fixed mass flow rate was used for comparability between the cases, but in order to provide better comparability between the two domains, either the bottomhole pressure at the producer or the mass flow injection rate, can be increased for future simulations. This should provide a better balance of injected vs. produced mass. Furthermore, it should be considered that because the simulations were not set up to maximize production, the numbers in Table 12 and the energy output calculation above, should not be compared to large scale geothermal power plants.

Chapter 7

Conclusion

Geothermal energy provides a strong pillar for solutions to mitigate the climate emergency by combining clean energy generation with carbon sequestration. Understanding different state of the art geothermal energy systems is essential to analyze the feasibility of expansion of the currently available technology portfolio as well as the exploration of opportunities such as supercritical enhanced geothermal systems. Projects like the Icelandic Deep Drilling Project provide the possibility to inject CO_2 into supercritical hydrothermal reservoirs at extremely high temperatures. The simulations in this thesis show that when comparing the injection of CO_2 and water, the cumulatively produced energy is higher for the water injection. This difference becomes large when comparing CO_2 vs. H_2O injection at a high injection temperature of 380°C with short well spacing. However, due to the breakthrough of CO_2, the cases of 400-m well spacing can be neglected. Additionally, as established previously, an injection temperature of 380°C is unfeasibly high as the CO_2 or water would need to be heated on the surface, which drives up the operating costs immensely and disqualifies this option as well. At an injection temperature of 60°C, the water case then has an advantage of additionally producing $0{,}3*10^{15}$ J, when $k = 1*10^{-15}$ m^2 and $0{,}1*10^{15}$ J additionally produced when $k = 1*10^{-14}$ m^2. This marginal advantage of increased power production in the water case has to be weighed against the added benefit of CO_2 storage. Injection of CO_2 also leads to a smaller area of the cooled region than for water injection which consequently reduces the risk of induced seismicity. When considering that the number of carbon capture and sequestration projects will increase over the next years, the occurrence of seismic events has the potential to increase, requiring an even more careful consideration of induced seismicity. Technological advancements in drilling equipment and exploration will support location of supercritical hydrothermal resources. Ongoing projects in Kakkonda Japan, Taupo Volcanic Area, New Zealand, the Geysers in California, USA as well as Laradello geothermal site in

Italy (Parisio et al. 2019) look promising to store supercritical CO_2. As shown in this thesis, the potential for sinking CO_2 is present if the right temperature and pressure conditions are encountered.

References

Aljughaiman, Ibraheem. 2022. “Supercritical CO2 Recirculation in Reservoirs for Continuous Storage and Production of Renewable Energy.” In , D032S152R001. https://doi.org/10.2523/IPTC-22268-MS.

Anderson, Austin, and Behnaz Rezaie. 2019. “Geothermal Technology: Trends and Potential Role in a Sustainable Future.” *Applied Energy* 248 (August): 18–34. https://doi.org/10.1016/j.apenergy.2019.04.102.

Bali, Enikö, László Aradi, Robert Zierenberg, Larryn Diamond, Thomas Pettke, Ábel Szabó, Guðmundur Guðfinnsson, G.Ó Friðleifsson, and Csaba Szabo. 2020. “Geothermal Energy and Ore-Forming Potential of 600 °C Mid-Ocean-Ridge Hydrothermal Fluids.” *Geology* 48 (August). https://doi.org/10.1130/G47791.1.

Basel I. Ismail, ed. 2022. “Geothermal Energy,” January. https://doi.org/10.5772/intechopen.87837.

Blazek, J. 2005. “Boundary Conditions.” In *Computational Fluid Dynamics: Principles and Applications*, 271–302. Elsevier. https://doi.org/10.1016/B978-008044506-9/50010-2.

Camuffo, Dario. 2014. “Chapter 7 - Atmospheric Stability and Pollutant Dispersion.” In *Microclimate for Cultural Heritage (Second Edition)*, edited by Dario Camuffo, 245–82. Boston: Elsevier. https://doi.org/10.1016/B978-0-444-63296-8.00008-1.

Celati, R., G. Cappetti, C. Calore, S. Grassi, and F. D’Amore. 1991. “Water Recharge in Larderello Geothermal Field.” *Geothermics* 20 (3): 119–33. https://doi.org/10.1016/0375-6505(91)90010-S.

Cleveland, Cutler J., and Robert U. Ayres, eds. 2004. *Encyclopedia of Energy*. Amsterdam ; Boston: Elsevier Academic Press.

Climo, Melissa, Lisa Lind, Simon Bendall, and Brian Carey. 2012. *The Rise and Rise of Geothermal Heat Pumps in New Zealand.*

Corey, A. 1954. “The Interrelation Between Gas and Oil Relative Permeability.” *Producers Monthly* 19 (January).

Davies, J. Huw. 2013. “Global Map of Solid Earth Surface Heat Flow.” *Geochemistry, Geophysics, Geosystems* 14 (10): 4608–22. https://doi.org/10.1002/ggge.20271.

Elders, W.A., and J.N. Moore. 2016. “Geology of Geothermal Resources.” In *Geothermal Power Generation*, 7–32. Elsevier. https://doi.org/10.1016/B978-0-08-100337-4.00002-4.

“Energy Balances.” 2022. STATISTICS AUSTRIA. November 11, 2022. https://www.statistik.at/en/statistics/energy-and-environment/energy/energy-balances.

Fitts, Charles R. 2013. “11 - Groundwater Contamination.” In *Groundwater Science (Second Edition)*, edited by Charles R. Fitts, 499–585. Boston: Academic Press. https://doi.org/10.1016/B978-0-12-384705-8.00011-X.

Fleming, Mark R., Benjamin M. Adams, Jonathan D. Ogland-Hand, Jeffrey M. Bielicki, Thomas H. Kuehn, and Martin O. Saar. 2022. “Flexible CO2-Plume Geothermal (CPG-F): Using Geologically Stored CO2 to Provide Dispatchable Power and Energy Storage.” *Energy Conversion and Management* 253 (February): 115082. https://doi.org/10.1016/j.enconman.2021.115082.

Friðleifsson, Guðmundur Ó., Wilfred A. Elders, Robert A. Zierenberg, Ari Stefánsson, Andrew P. G. Fowler, Tobias B. Weisenberger, Björn S. Harðarson, and Kiflom G. Mesfin. 2017. “The Iceland Deep Drilling Project 4.5 Km Deep Well, IDDP-2, in the Seawater-Recharged Reykjanes Geothermal Field in SW Iceland Has Successfully Reached Its Supercritical Target.” *Scientific Drilling* 23 (November): 1–12. https://doi.org/10.5194/sd-23-1-2017.

GeoEnergy, Think. 2021. “An Overview of Geothermal Resources | ThinkGeoEnergy.” February 23, 2021. https://www.thinkgeoenergy.com/geothermal/an-overview-of-geothermal-resources/.

“Geothermal: Digging Beneath the Surface.” 2020. JPT. October 1, 2020. https://jpt.spe.org/geothermal-digging-beneath-surface.

“Geothermal Potential Runs Hot in Texas.” 2023. JPT. March 1, 2023. https://jpt.spe.org/geothermal-potential-runs-hot-in-texas.

Geothermal Technologies Office. 2019. “GeoVision: Harnessing the Heat Beneath Our Feet.” DOE/EE-1306, 1879171, 8890. https://doi.org/10.2172/1879171.

“Geothermal Well Construction: A Step Change in Oil and Gas Technologies.” 2021. JPT. January 1, 2021. https://jpt.spe.org/geothermal-well-construction-a-step-change-in-oil-and-gas-technologies.

Giljarhus, Knut Erik Teigen, Svend Tollak Munkejord, and Geir Skaugen. 2012. “Solution of the Span–Wagner Equation of State Using a Density–Energy State Function for Fluid-Dynamic Simulation of Carbon Dioxide.” *Industrial & Engineering Chemistry Research* 51 (2): 1006–14. https://doi.org/10.1021/ie201748a.

Glassley, William E. 2010. *Geothermal Energy: Renewable Energy and the Environment*. Energy and the Environment. Boca Raton: CRC Press.

Green, Bruce D. 2004. “Geothermal Technologies Program: Direct Use,” August.

Guinot, Frédéric, and Peter Meier. 2019. “Can Unconventional Completion Systems Revolutionise EGS? A Critical Technology Review.” In , D041S012R006. https://doi.org/10.2118/195523-MS.

Gupta, Nandlal, and Manvendra Vashistha. 2016. “Carbon Dioxide Plume Geothermal (CPG) System-A New Approach for Enhancing Geothermal Energy Production and Deployment of CCUS on Large Scale in India.” *Energy Procedia* 90 (December): 492–502. https://doi.org/10.1016/j.egypro.2016.11.216.

“Hot Spots.” 2022. May 20, 2022. https://education.nationalgeographic.org/resource/hot-spots.

Hu, Xiaodong, Xianzhi Song, Kan Wu, Yu Shi, and Gensheng Li. 2021. “Effect of Proppant Treatment on Heat Extraction Performance in Enhanced Geothermal System.” *Journal of Petroleum Science and Engineering* 207 (December): 109094. https://doi.org/10.1016/j.petrol.2021.109094.

Huenges, Ernst, ed. 2010. *Geothermal Energy Systems: Exploration, Development, and Utilization*. Weinheim: Wiley-VCH.

Katterbauer, Klemens, Abdulaziz Qasim, Abdallah Al Shehri, and Abdulkareem Al Sofi. 2022. “A Deep Learning Optimization Framework for Geothermal Energy Production Based on Carbon Dioxide.” In *Day 3 Wed, October 05, 2022*, D031S057R003. Houston, Texas, USA: SPE. https://doi.org/10.2118/210295-MS.

Lake, Larry W., John R. Fanchi, and Society of Petroleum Engineers (U.S.), eds. 2006. *Petroleum Engineering Handbook*. Richardson, TX: Society of Petroleum Engineers.

“LibMesh - A C++ Finite Element Library.” 2023. March 11, 2023. https://libmesh.github.io/.

Lindsay, Alexander D., Derek R. Gaston, Cody J. Permann, Jason M. Miller, David Andrš, Andrew E. Slaughter, Fande Kong, et al. 2022. “2.0 - MOOSE: Enabling Massively

Parallel Multiphysics Simulation." *SoftwareX* 20 (December): 101202. https://doi.org/10.1016/j.softx.2022.101202.

McClure, Mark W., and Roland N. Horne. 2014. "An Investigation of Stimulation Mechanisms in Enhanced Geothermal Systems." *International Journal of Rock Mechanics and Mining Sciences* 72: 242–60. https://doi.org/10.1016/j.ijrmms.2014.07.011.

Meyers, Robert A., ed. 2002. *Encyclopedia of Physical Science and Technology*. 3rd ed. San Diego: Academic Press.

"Minifrac." 2017. April 5, 2017. https://www.ihsenergy.ca/support/documentation_ca/WellTest/content/html_files/reference_materials/general_concepts/minifrac.htm.

Mondejar, M.E., and C.R. Chamorro. 2017. "Geothermal Power Technologies." In *Encyclopedia of Sustainable Technologies*, 51–61. Elsevier. https://doi.org/10.1016/B978-0-12-409548-9.10095-8.

Ott, Holger. 2018. "Enhanced Geothermal Systems." University of Leoben, Leoben, November 8.

Parisio, Francesco, and Victor Vilarrasa. 2020. "Sinking CO_2 in Supercritical Reservoirs." *Geophysical Research Letters* 47 (23). https://doi.org/10.1029/2020GL090456.

———. 2022. "CO2 Flow in Supercritical Geothermal Systems." Presented at the EGU General Assembly, May 25.

Parisio, Francesco, Victor Vilarrasa, Wenqing Wang, Olaf Kolditz, and Thomas Nagel. 2019. "The Risks of Long-Term Re-Injection in Supercritical Geothermal Systems." *Nature Communications* 10 (1): 4391. https://doi.org/10.1038/s41467-019-12146-0.

"PEH:Hydraulic Fracturing." 2017. PetroWiki. April 26, 2017. https://petrowiki.spe.org/PEH:Hydraulic_Fracturing.

Pongratz, Reinhard. 2021. "Hydraulic Fracturing Basics and Practical Applications." Lecture presented at the Formation Impairment and Stimulation, University of Leoben, Leoben, December 3.

Saar, Martin, Jimmy Randolph, Thomas Kuehn, Jeffrey Bielicki, and Steven Taff. 2012. "Numerical Modeling of CO2-Plume Geothermal (CPG) Systems." September 1, 2012. https://geg.ethz.ch/project-co2-plume/.

Satter, Abdus, and Ghulam M. Iqbal. 2016. *Reservoir Engineering: The Fundamentals, Simulation, and Management of Conventional and Unconventional Recoveries*. Amsterdam: Elsevier.

"Season Greetings 2020 Test - IDDP." 2022. IDDP -. July 7, 2022. https://iddp.is/saga-report-no-12-test-copy-copy/.

Slaughter, Andrew E., Cody J. Permann, Jason M. Miller, Brian K. Alger, and Stephen R. Novascone. 2021. "Continuous Integration, In-Code Documentation, and Automation for Nuclear Quality Assurance Conformance." *Nuclear Technology* 207 (7): 923–30. https://doi.org/10.1080/00295450.2020.1826804.

Spice, Holly. 2021. "VOLCANIC ACTIVITY IN THE REYKJANES PENINSULA." HIDDEN ICELAND. March 14, 2021. https://hiddeniceland.is/volcanic-activity-in-the-reykjanes-peninsula/.

"Step-down Test Analysis." 2017. April 5, 2017. https://www.ihsenergy.ca/support/documentation_ca/WellTest/content/html_files/analysis_types/minifrac_test_analyses/step-down_test_analysis.htm.

"Supercritical CO2 Tech Team." 2023. Energy.Gov. April 14, 2023. https://www.energy.gov/supercritical-co2-tech-team.

"Technology - Eavor - Closed-Loop Geothermal, Unlike Any Other." 2023. *Eavor* (blog). April 11, 2023. https://www.eavor.com/technology/.

"Technology - Sage Geosystems™." 2021. May 25, 2021. https://www.sagegeosystems.com/technology/.

"USGS: Volcano Hazards Program Glossary - Dike." 2015. May 12, 2015. https://volcanoes.usgs.gov/vsc/glossary/dike.html.

Vilarrasa, Victor, Diogo Bolster, Marco Dentz, Sebastia Olivella, and Jesus Carrera. 2010. "Effects of CO2 Compressibility on CO2 Storage in Deep Saline Aquifers." *Transport in Porous Media* 85 (2): 619–39. https://doi.org/10.1007/s11242-010-9582-z.

Wagner, W., J. R. Cooper, A. Dittmann, J. Kijima, H.-J. Kretzschmar, A. Kruse, R. Mareš, et al. 2000. "The IAPWS Industrial Formulation 1997 for the Thermodynamic Properties of Water and Steam." *Journal of Engineering for Gas Turbines and Power* 122 (1): 150–84. https://doi.org/10.1115/1.483186.

Wang, Yu, Tianfu Xu, Yuxiang Cheng, and Guanhong Feng. 2022. "Prospects for Power Generation of the Doublet Supercritical Geothermal System in Reykjanes Geothermal Field, Iceland." *Energies* 15 (22): 8466. https://doi.org/10.3390/en15228466.

Wells, Sharon L., and Joseph DeSimone. 2001. "CO2 Technology Platform: An Important Tool for Environmental Problem Solving." *Angewandte Chemie International Edition* 40 (3): 518–27. https://doi.org/10.1002/1521-3773(20010202)40:3<518::AID-ANIE518>3.0.CO;2-4.

"What Is Supercritical CO2?" 2021. Alicat Scientific. March 4, 2021. https://www.alicat.com/knowledge-base/why-supercritical-co2-is-super-cool/.

Wilkins, Andy, Christopher Green, and Jonathan Ennis-King. 2020. "PorousFlow: A Multiphysics Simulation Code for Coupled Problems in Porous Media." *Journal of Open Source Software* 5 (55): 2176. https://doi.org/10.21105/joss.02176.

Wilkins, Andy, Christopher P. Green, and Jonathan Ennis-King. 2021. "An Open-Source Multiphysics Simulation Code for Coupled Problems in Porous Media." *Computers & Geosciences* 154 (September): 104820. https://doi.org/10.1016/j.cageo.2021.104820.

Wischnewski, Berndt. 2007. "Calculation of Thermodynamic State Variables of Carbon Dioxide." Peace Software. June 2007. https://www.peacesoftware.de/einigewerte/co2_e.html.

"Work Packages." 2016. *DEEPEGS* (blog). February 23, 2016. https://deepegs.eu/work-packages/.

Zhou, Xianmin, Fawaz Al-Otaibi, and Sunil Kokal. 2019. "Relative Permeability Characteristics and Wetting Behavior of Supercritical CO_2 Displacing Water and Remaining Oil for Carbonate Rocks at Reservoir Conditions." *Energy & Fuels* 33 (6): 5464–75. https://doi.org/10.1021/acs.energyfuels.9b01053.

Appendix A

Input Files

The input files for the different cases were uploaded to a repository on GitHub. In order to find information on which variables were changed in each case, please consult the CaseBook.xls file in the repository.

Additionally, to the MOOSE files, the mesh files are uploaded as well. For definition of wellbore information and location, the well_in.bh and well_out.bh files are used in the form of (wellbore radius, x-Coordinate, y-Coordinate, z-Coordinate).

The cumulative produced energy was determined via utilization of Jupyter notebooks, which are uploaded as well.

GitHub-Link:

https://github.com/plo8010/Supercritical-CO2

List of Figures

List of Tables